Scholar Commons
USF University of South Florida

University of South Florida
Scholar Commons

Graduate Theses and Dissertations | Graduate School

November 2017

A High Accuracy Microwave Radiometric Thermometer to Measure Internal Body Temperature

Michael D. Grady
University of South Florida, gradym@mail.usf.edu

Follow this and additional works at: https://scholarcommons.usf.edu/etd


Part of the Biomedical Engineering and Bioengineering Commons, and the Electromagnetics and Photonics Commons

Scholar Commons Citation
Grady, Michael D., "A High Accuracy Microwave Radiometric Thermometer to Measure Internal Body Temperature" (2017). *Graduate Theses and Dissertations.*
https://scholarcommons.usf.edu/etd/7404

This Dissertation is brought to you for free and open access by the Graduate School at Scholar Commons. It has been accepted for inclusion in Graduate Theses and Dissertations by an authorized administrator of Scholar Commons. For more information, please contact scholarcommons@usf.edu.

المنارة للاستشارات

www.manaraa.com

A High Accuracy Microwave Radiometric Thermometer to Measure Internal Body Temperature

by

Michael D. Grady

A dissertation submitted in partial fulfillment
of the requirements for the degree of
Doctor of Philosophy in Electrical Engineering
Department of Electrical Engineering
College of Engineering
University of South Florida

Major Professor: Thomas Weller, Ph.D.
Gokhan Mumcu, Ph.D.
Frank Pyrtle, Ph.D.
Stephen Saddow, Ph.D.
Hariharan Srikanth, Ph.D.

Date of Approval:
October 23, 2017

Keywords: Wireless and Non-Invasive Thermography, Comprehensive Radiometer Model, On-Body Inward Facing Antennas, Radiative Transfer Modeling

Copyright © 2017, Michael D. Grady

www.manaraa.com

Dedication

The dissertation is dedicated to my late grandparents (Easter Grady and William Thomas Grady); to my late aunt (Barbara Ann Chilsom); to my late high school calculus teacher (Ms. Laura Little); and to my late undergraduate mentor (Dr. Dennis Weatherby). This dissertation is also dedicated to my many mentors, friends, and family who supported and pushed me throughout this process. Last but not least, this dissertation is dedicated to any person that I may inspire to reach for greatness. I am a strong believer in the fact that greatness is created! This dissertation is the product of many long hours of hard work and dedicated focus. I look forward to this platform helping me to help others reach for greatness!

www.manaraa.com

Acknowledgments

I would like to express a warm thank you to my tactful, encouraging, patient, and kind major professor, Dr. Thomas M. Weller. While Dr. Weller is indeed a brilliant man, to only praise him for his intellect does not do him justice. Under his apprenticeship, I can strongly say that I have become an independent researcher. I am very proud to be a part of his research lineage! I would also like to thank my dissertation committee Dr. Gokhan Mumcu, Dr. Frank Pyrtle, Dr. Stephen Saddow, and Dr. Hariharan Srikanth; and my oral defense chair Dr. Venkat Bhethanabotla.

Thanks to all of my ENB 412 friends and colleagues. There are too many people to name, but I have had a wonderful experience due to all of you. Thanks to Ramiro Ramirez for offering comments on this dissertation. Thanks to Jon Obrien for always helping out the cause when he was called upon. Special thanks to Arya Menon for reading this dissertation and helping me to prepare for my oral defense.

Thanks to all of my technical supporters (Dr. Quenton Bonds, Dr. Ibrahim Nassar, Dr. John Gerig, Dr. James Randa, Dr. Arthur Snider, Dr. Larry Dunleavy, Dr. Jerome McClendon, and Dr. Jordon Gilmore). Thanks to all of the undergraduate researchers who supported this project (Robert Donatto, Timothy Proto, and Emily Schultz). Thanks to Mr. Bernard Batson for being a wonderful and supportive mentoring figure. Mr. Batson's support is immeasurable! Thanks to Dr. Al-Aakhir Rogers for introducing me to this wonderful university. Thanks to my family, friends, and mentors for their love, encouragement, and support.

Thanks to the funding support from NSF, the IEEE MTT-S Graduate Fellowship, the Alfred P. Sloan Minority Ph.D. Scholarship, the McKnight Doctoral Fellowship, and the GEM Doctoral Fellowship.

www.manaraa.com

Table of Contents

www.manaraa.com

www.manaraa.com

www.manaraa.com

www.manaraa.com

List of Tables

www.manaraa.com

List of Figures

www.manaraa.com

www.manaraa.com

www.manaraa.com

www.manaraa.com

www.manaraa.com

www.manaraa.com

Abstract

The Center for Disease Control and Prevention (CDC) released heat illness data which highlighted that ~29 heat stress hospitalizations [1] and ~3 heat-related deaths [2] occurred every day during the summer months within the US from years 2000 to 2014. Heatstroke- the most severe form of heat illness which oftentimes lead to death- has been cited to be entirely preventable if a timely intervention is introduced [3]. This dissertation uses microwave radiometric thermometry to perform wireless non-invasive internal body temperature monitoring which can enable intervention methods that help to prevent deaths associated with heat-illness.

Overall, this dissertation develops a comprehensive closed-form analytical radiometric model and validates the effectiveness of the comprehensive model through a controlled life-like human body temperature sensing experiment. Wireless sub-skin temperature data is predicted from a human tissue mimicking phantom testbed to within 1%.

A generic isolated radiometer system equation is derived for all possible calibration source combinations. The generic isolated radiometer system equation predicts comparable results to that of an ideal simulation. While improved isolation decreases measurement uncertainty, it does not improve the accuracy of estimated noise temperatures using a perfectly-isolated radiometer system equation assumption.

A highly reproducible tissue-mimicking biological phantom (bio-phantom) recipe (comprised of urethane, graphite powder, and a solvent) was developed to accurately emulate the electrical properties of actual dry human skin versus frequency up to 18 GHz. The developed solid state skin phantom begins in pourable liquid form and then cures at room temperature into a dry solid state mold.

www.manaraa.com

An in-plane electromagnetic bandgap structure was developed and integrated within an on-body inward facing spiral antenna design. The inclusion of the in-plane electromagnetic bandgap structure demonstrated a +2.64dB gain improvement in the antenna broadside and -8dB in the rear gain while in-contact with the body as compared to the conventional spiral antenna. Likewise, the measured main beam efficiency is improved from 54.43% for the conventional antenna to 86.36% for the EBG antenna.

Two techniques based on signal-flow graph theory were derived to explain both the non-coherent steady-state radiative transfer and the coherent radiative transfer within multi-layered dielectric media with non-uniform temperatures and any number of stratified layers. Both models allow for the accurate characterization and sensing of the thermal emissions originating from subsurface tissue layers.

www.manaraa.com

Chapter 1 Introduction

1.1 Motivation

Both heat stress hospitalizations and heat-related deaths negatively affect the lives of United States (US) persons during the summer months. The Center for Disease Control and Prevention (CDC) released heat illness data which emphasized the frequency in which both heat stress hospitalizations [1] and heat-related deaths [2] occur during the summer months (May 1 to September 30) within the US. The CDC statistics highlighted that ~29 heat stress hospitalizations and ~3 heat-related deaths occurred every day during the summer months within the US from years 2000 to 2014. Similar heat-related mortality outcomes are highlighted in Table 1.1.

Table 1.1 Various heat illness consequences within the United States (US)

Entity	Study Period	Group Affected	Heat- related event
Center for Disease Control and Prevention (CDC)	2000 - 2014	US persons	29 heat-stress hospitalizations and 3 heat-related deaths per day
	2006 - 2010		1.83 deaths per day
National High School Sports-Related Injury Surveillance	2005 - 2009	US high school athletes	A leading cause of death and disability in practice and competition
Total Army Injury Health Outcomes Database	1980 - 2002	Operational military personnel	5,246 heat-stress hospitalizations and 37 heat-related deaths
Annual Survey of Football Injury	1995 - 2010	US football players	42 heat-related deaths (31 HS, 8 collegiate, 2 professional, and 1 sandlot)

Heat illness outcomes and other undesirable healthcare effects led to the Engineering and Physical Science Research Council (EPSRC) issuing a call to action defining four major healthcare technologies grand challenges intended to accelerate the translation of scientific research in benefiting healthcare applications [4]. The four EPSRC healthcare technologies grand challenges are: (1) to use real-time information to support self-management of health and wellbeing, and

www.manaraa.com

facilitate timely interventions, (2) to optimize treatment for individuals through early diagnosis, patient-specific prediction and evidence-based intervention, (3) to enhance the precision and minimize the invasiveness of surgery, radiotherapy, and other physical interventions, and (4) to support the development of new therapies to enhance efficacy, minimize costs and reduce risk to patients. This dissertation will address the EPSRC grand challenges number (1) and (2) by using microwave radiometric thermometry to perform wireless non-invasive sub-skin core temperature monitoring which can enable intervention methods that help to prevent deaths associated with heat-illness.

The long term goal of this work is to advance the existing body of knowledge in portable biomedical radiometry and ultimately lead to outcomes that support the full-system modeling of a microwave thermometer that is able to non-invasively, wirelessly, and accurately extract internal body temperature. The overall objective of this dissertation is to develop a comprehensive closed-form analytical radiometric model and to validate the effectiveness of the comprehensive model through a controlled life-like human body temperature sensing experiment. The outcomes found in this dissertation are steps toward that research goal by answering the question, "Can a closed-form analytical radiometric model provide sufficient detail to resolve sub-skin internal body temperature with 0.2°C accuracy?" A temperature accuracy of 0.2°C is chosen due this value being the quoted accuracy of many inexpensive (< $15) oral digital thermometers.

1.2 Background

The threat of a heat-related death is more eminent for active persons in high heat environments, such as student athletes practicing their respective sport in extreme summer heat. Both the high intensity activity and the high heat environment produce an excessive heat load on the athlete's body. If the athlete's body is unable to dissipate enough excess heat through cooling methods like the evaporation of sweat, then the athlete's core body temperature will rise beyond healthy levels. Moreover, if the athlete's body is unable to regulate normal temperature conditions

www.manaraa.com

and his/her core temperature ultimately rises above 104 °F, then an exertional heatstroke may ensue [3, 5, 6]. The effects of an exertional heat stroke, can lead to liver damage, bloods clots, and the failure of vital organs which oftentimes lead to hospitalization and death. Conversely, deaths attributed to heat-illness may be entirely preventable if a timely intervention is introduced [3]. The currently prescribed heatstroke interventions include visual-based subjective assessments, heat acclimatization techniques, or core temperature monitoring systems [5]. While there are many options to measure core body temperature for non-active persons (e.g. oral/ear/temporal/rectal thermometers [7]), there exists few options to measure core body temperature for active persons. Bio-wireless technology has been suggested as a potential method for monitoring core body temperature in active persons [8, 9]. Current commercially available bio-wireless solutions include, internal body thermometry (*e.g.* gastrointestinal (GI) radio-pills [7, 9]) or wireless thermometry (*e.g.* infrared (IR) sensors [7]). Although the wireless nature of the IR thermometer (shown in Figure 1.1(a)) features increased portability, this technology is limited in that it only provides temperature information from the surface of the skin. The GI radio-pill, given in Figure 1.1(b), provides the temperature of the GI tract which is accepted as a good representation of core body temperature [10, 11]. Although the GI radio-pill accurately predicts changes in core temperature, its adoption is limited by both a ~$25 per single use cost and the invasiveness of the user having to ingest and expel the radio-pill through the digestive system [8, 9].

This dissertation uses microwave radiometric thermometry (Figure 1.1(c)) to perform wireless non-invasive core body temperature monitoring. Microwave radiometric thermometry is an attractive method to measure internal body temperature because it combines the advantages of both the wireless thermometry and internal body thermometry techniques and provides a means for wireless non-invasive internal body thermometry. Not only does a microwave radiometric thermometer give more comprehensive temperature depth information from the internal body (in

www.manaraa.com

contrast to IR sensors providing skin temperature), it is also less invasive in nature (than the currently deployed GI radio-pill).

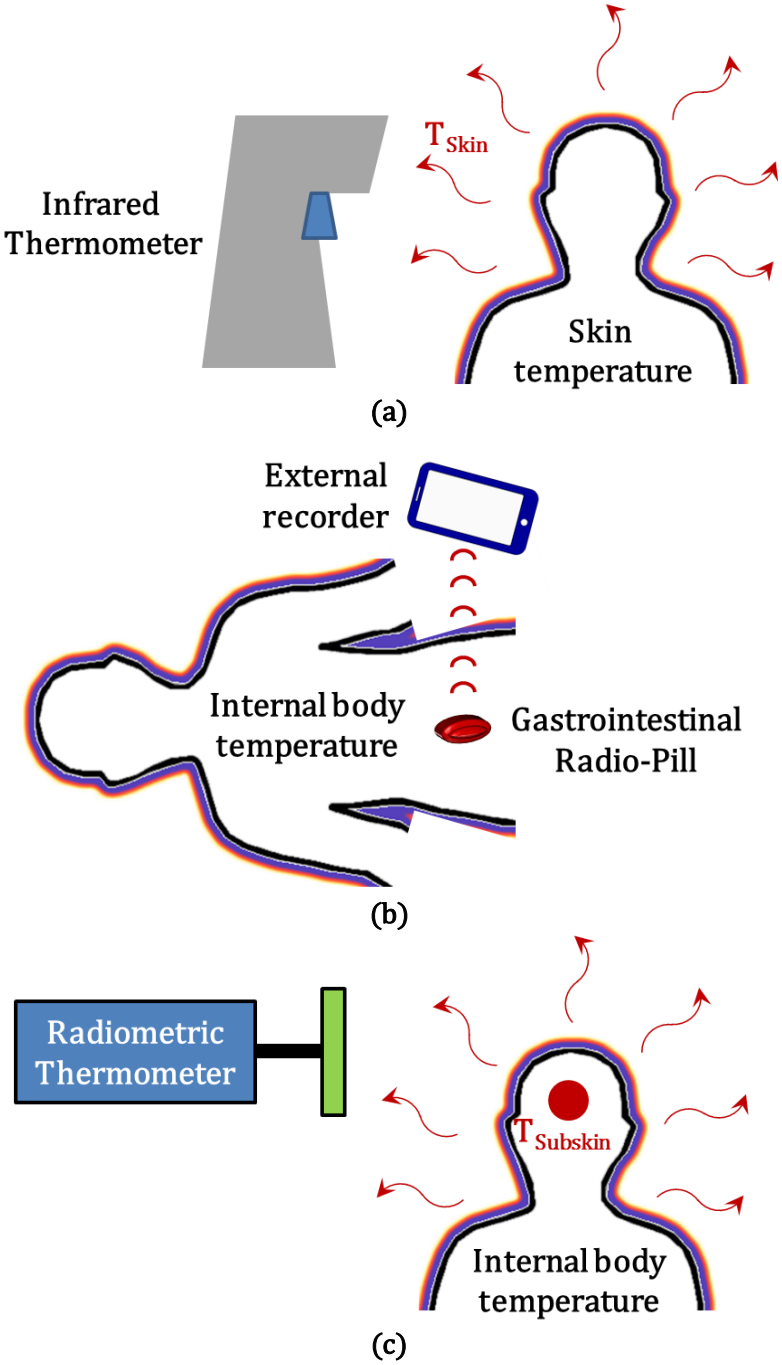

Figure 1.1 Comparison of (a) an infrared thermometer wirelessly measuring the skin surface temperature of a human, (b) a gastrointestinal radio-pill invasively measuring the internal body temperature and transmitting the temperature data to an external recorder, and (c) a microwave radiometric thermometer wirelessly and non-invasively measuring internal body temperature. Microwave thermometry combines the advantages of both internal body and wireless techniques.

www.manaraa.com

1.3 Challenges in Resolving Internal Body Temperature Using a Microwave Radiometer

A microwave radiometer is a sensitive receiver designed to passively measure changes in radiation (on the order of 10^{-16} watts) resolved from a material under test. The passive measurement of temperature is plagued by three main challenges: (1) the difficulty involved with resolving minuscule changes in the temperature of the object, (2) the accuracy in how well the measurement system is known, and (3) the accuracy in how well the radiometric model properly characterizes the material under test.

To better illustrate the challenges involved with resolving the small changes in the thermal emissions originating from the human body, consider this example with a typical radiometer system with 100 MHz of bandwidth and 100 dB of total system gain. Figure 1.2 illustrates the small changes in the radiation originating from the body and the corresponding radiometer output power for these changes. The radiation received from the human body at a temperature of 98.70 °F (or 37.05 °C) is equal to 4.282×10^{-13} watts. After this emitted energy from the human body is received by the antenna and passed through the radiometer system, the radiometer output is 4.282×10^{-3} watts. If a 0.1 °C (ΔC) temperature change (*i.e.* $\Delta F = 0.18$ °F) is desired to be detected, then the radiometer would have to detect a power variation of 1.380×10^{-16} watts from the human body which corresponds to a radiometer output change of 1.380×10^{-6} watts. This example highlights the fact that the output power resulting from changes in radiation originating from the body are still relatively small even after 100 dB of amplification to the input power (10 billion times greater than the input power). The difficulty of passively resolving internal body temperature with a microwave radiometer is further heightened due to uncertainties in the electrical properties of the material under test, device characteristics, antenna properties, and the proper modeling of the propagation of electromagnetic waves throughout stratified media. The presence of these uncertainties may compromise the radiometer's ability to resolve 0.1°C changes in internal body temperature.

www.manaraa.com

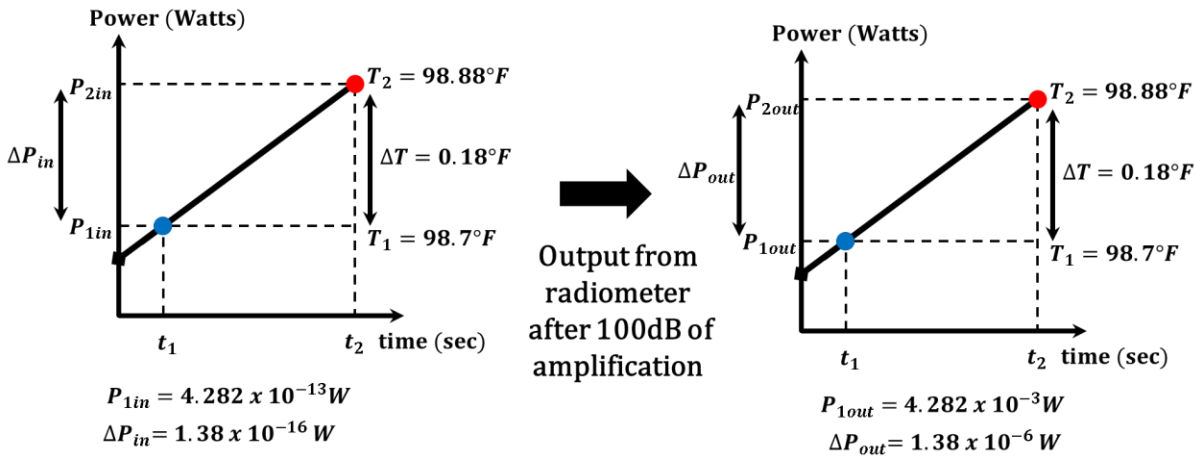

Figure 1.2 Example of typical changes in the radiation (in terms of power) received from the body and the resulting output after radiation is passed through a microwave radiometer with 100 dB of gain. Example assumes an initial temperature T_1 of 98.7°F (corresponding to an input power P_{1in} of 4.282 x10^{-13} and an output power P_{1out} of 4.282 x10^{-3}) with a temperature change ΔT of 0.18°F. The 0.18°F temperature change corresponds to a power variation ΔP_{in} of 1.38 x10^{-16} watts at the input of the radiometer and ΔP_{out} of 1.38 x10^{-6} watts at the output of the radiometer.

If the radiometer were an ideal system, then the output power would be precisely the power gain multiplicative of the input power ($P_{out}^{ideal} = Gain \cdot P_{in}$). However, since an ideal radiometer system does not exist within real-world measurement applications, there exists some uncertainty in the operation of the system performance ($P_{out}^{actual} = Gain \cdot [1 \pm \Delta Gain] \cdot P_{in} \cdot [1 \pm \Delta P_{in}]$ where $\Delta Gain$ is the gain uncertainty and ΔP_{in} is the input power uncertainty). This uncertainty in the system's electrical behavior should be modeled in order to predict how the resulting output should behave. Likewise, since microwave radiometry is an entirely passive sensing technique, prior knowledge of the scattering and emission within the stratified tissues of the human body must be known in order to accurately correlate the electromagnetic (EM) behavior of the multi-layered body tissues back to the passive measurement of absolute sub-skin temperature. This implies that both the dielectric constant and the material thickness must be precisely known in order to predict absolute temperature from a buried layer.

These abovementioned challenges encourage the need for a comprehensive radiometric model which overcomes the difficulties involved with the passive measurement of sub-skin

www.manaraa.com

temperature. This dissertation will address the development of such a comprehensive model that enables these challenges to be transcended. In other words, the EM behavior of the entire MW thermometer ecosystem is modeled.

1.4 Research Objectives

The overall objective of this dissertation is to develop a comprehensive closed-form analytical radiometric model to accurately resolve internal body temperature at the output of a radiometer system. This objective is accomplished by modeling the full EM behavior of the entire MW thermometer ecosystem (*i.e.* every EM interaction is modeled from the radiometric sensor to the material under test). The effectiveness of the comprehensive radiometric model is validated with a comparison to a controlled measurement of internal body temperature from a physically and electrically accurate human body tissue-mimicking phantom testbed. The anatomy of the comprehensive closed-form analytical radiometric model consists of the following subsystems seen in Figure 1.3: (A) the radiometer calibration and system equation modeling, (B) the antenna modeling, (C) the radiative transfer modeling, (D) the human body modeling (which is represented by a tissue-mimicking phantom testbed), and (Σ) the combination of subsystems (A) to (D) to achieve noninvasive internal body temperature extraction. Specifically, the following aims will be pursued:

(A) the radiometer calibration and system equation modeling, which includes a correction from the radiometer output to antenna input;

(B) the antenna modeling, which includes a correction for the antenna radiation and main-beam efficiencies;

(C) the radiative transfer modeling, which includes a correction from the skin surface down to the last layer of interest;

(D) the tissue-mimicking phantom modeling, which includes the modeling of the electromagnetic properties of the tissue;

www.manaraa.com

(Σ) an accurate non-invasive internal body temperature extraction, which includes the full system modeling to accurately resolve internal temperature at output of radiometer.

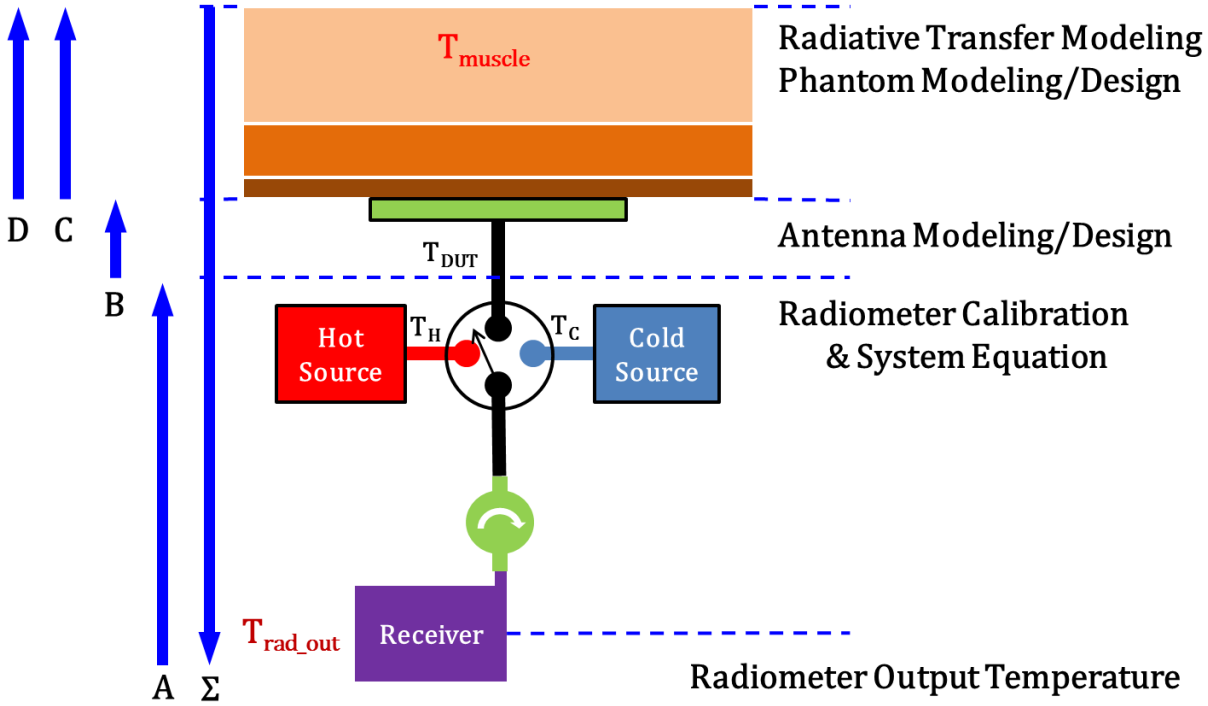

Figure 1.3 Anatomy of the comprehensive closed-form analytical radiometric model. Path Σ - full system modeling to accurately resolve internal temperature at the output of the radiometer. Path A - correction from the radiometer output to input. Path B - correction from the radiometer output to the antenna input. Path C - correction from the skin surface down to the last layer of interest. Path D - the human body modeling (which is represented by a tissue-mimicking phantom testbed).

1.5 Methodology and Validation for Internal Body Temperature Sensing

The comprehensive closed-form analytical radiometric model will be validated with radiometric measurements from an anatomically accurate human body testbed. The measurement setup for this microwave thermometer ecosystem consists of a microwave radiometer operating at 1.4 GHz, connected to an antenna that is placed in contact with a four-layer human body tissue-mimicking phantom testbed (Figure 1.4). The layered tissue-mimicking phantom testbed is made up of materials that mimic the electrical and physical properties of a human abdominal core: a liquid muscle phantom, a solid skin phantom, a solid fat phantom, and air. The liquid muscle phantom is heated and placed in contact with both the fat and skin phantoms. Physical temperature

www.manaraa.com

changes of the layered tissue phantoms are tracked over time with a data-logger thermometer. Thermocouple probes connected to the data-logger thermometer are used to measure the temperatures of the ambient environment, the skin layer, the fat layer, the muscle layer, and the heated and cooled final air layer. Experimental temperature data from the heated tissue phantom testbed is extracted with the radiometer, independently modeled, and compared to the temperature output of the thermocouple probes.

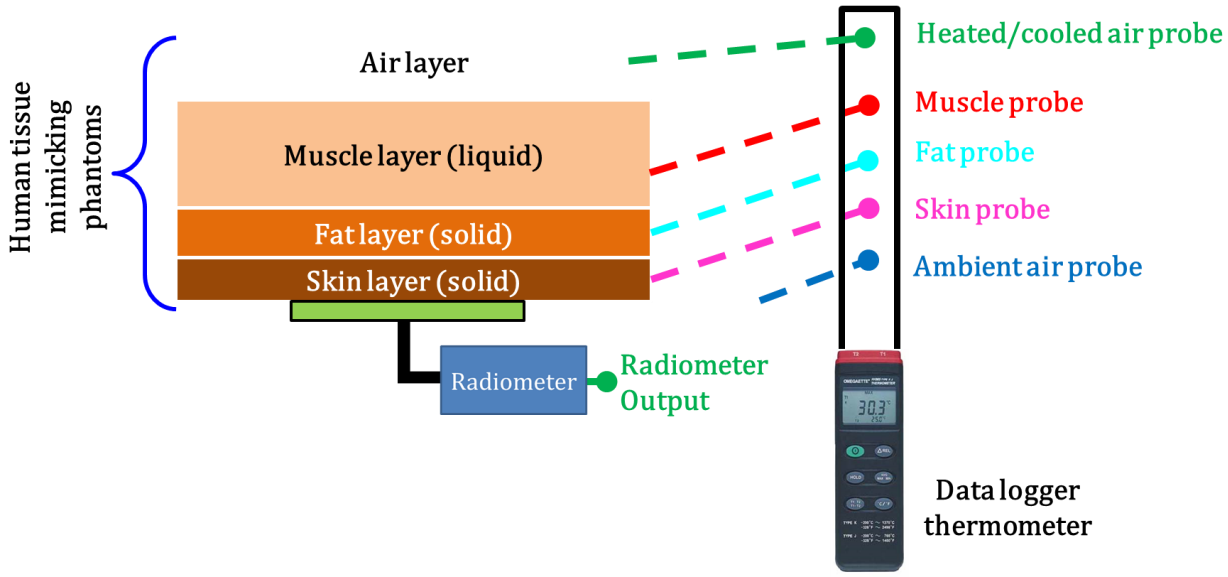

Figure 1.4 Measurement set-up for a microwave radiometric thermometer. An antenna connected to a microwave radiometer is placed in contact with a four-layer human body tissue-mimicking phantom testbed (skin, fat, muscle, air). Thermocouple probes connected to a data-logger thermometer are used to record the physical temperatures of the ambient environment, the skin layer, the fat layer, the muscle layer, and the final heated and cooled air layer.

1.6 Significance of Research Aims and Contributions to the Field

1.6.1 Internal Body Microwave Radiometric Sensing

1.6.1.1 Overall Significance

Of the available microwave radiometry works for biomedical sensing, most provide radiometric models only sophisticated enough to resolve relative internal body temperature. No current works give a closed-form analytical model with enough accuracy to provide a credible prediction of absolute internal body temperature. Up until the point, the available MW radiometric

www.manaraa.com

models either (1) give radiometric formulations calculated from computer-aided simulation software which would only work for relative temperature measurements [12] or (2) give closed-form analytical radiometric formulations which lack the required detail to achieve high accuracy absolute temperature monitoring [13, 14]. The next logical step is to realize a more comprehensive closed-form analytical radiometric model that is capable of resolving temperature to within 0.1°C.

1.6.1.2 Overall Contribution

This dissertation introduces new modeling techniques that leverage from existing works in order to develop a more comprehensive closed-form analytical radiometric model that will allow for the accurate sensing of internal body absolute temperature.

1.6.2 Radiometer System Equation

1.6.2.1 Significance

To this point, there is no available fully generic radiometer system equation that adequately accounts for all potential source temperatures. Nor has any study looked at the error resulting from using simplified radiometer system equations with respect to different amounts of system isolation.

1.6.2.2 Contribution

This work derives a generic radiometer system equation that accounts for all available noise source combinations. Varying assumptions are applied which lead to simpler, more convenient forms of the radiometer system equation. Noise temperature is extracted for an unknown DUT using varying amounts of system isolation and applying each form of the radiometer system equation.

1.6.3 Biological Tissue Phantoms

1.6.3.1 Significance

In order to avoid measurement discrepancies during the sensing system optimization, biomedical measurements must be performed with materials that accurately represent the electromagnetic properties of the human body. Tissue-mimicking phantoms are realistic models

www.manaraa.com

that mimic the electrical properties of the human tissue and allow the user to validate the microwave system in comparison to simulations. The availability of reliable solid state human skin tissue-mimicking phantom recipes is limited. Of the available solid state skin phantom recipes, most either do not provide adequate details to recreate the phantom recipe or require extremely invasive mixing techniques (*e.g.* the user is required to knead the messy phantom material by hand).

1.6.3.2 Contribution

This dissertation highlights the development of a highly reproducible tissue-mimicking phantom recipe that accurately mimics the electrical properties of actual dry human skin versus frequency up to 18 GHz. The developed solid state skin phantom begins in pourable liquid form and then cures at room temperature into a dry solid state mold. Pourable solid state skin phantoms make realizing any desired thickness much easier as compared to previous recipes which require kneading by hand.

1.6.4 On-Body Inward Facing Antenna

1.6.4.1 Significance

Designing antennas for human body contact sensing imposes a number of restrictions that are unique to this specific case. In this scenario, antenna input match along with radiation and beam efficiencies must be precisely known and maximized. Few works exist in literature that explicitly outlines how to design antennas for on-body inward facing applications [12, 13, 15-27]. Of the available on-body antenna designs most provide SAR patterns, but do not include antenna radiation patterns for the scenario when the antenna is in contact with the body [12, 15, 17-27]. Most of these works also do not discuss the proper way to mitigate unwanted side lobes that become apparent during an on-body or near-field sensing application.

www.manaraa.com

1.6.4.2 Contribution

This dissertation contributes to the body of knowledge by providing a novel implementation of an in-plane quasi-corrugated, cylindrically symmetric, electromagnetic bandgap (EBG) structure that is used to mitigate unwanted side lobes that arise from inward facing antennas. To the best of the author's knowledge, this is the first time that this type of in-plane quasi-corrugated cylindrically-symmetric EBG has been used for an on-body antenna sensing application.

1.6.5 Closed-Form Analytical Radiative Transfer Model

1.6.5.1 Significance

Since microwave radiometry is an entirely passive sensing technique, prior knowledge of the scattering and emission within the stratified tissues of the human body must be known in order to accurately correlate the electromagnetic (EM) behavior of the multi-layered body tissues back to the passive measurement of absolute sub-skin temperature. In current literature, the derivation for both coherent and non-coherent emission and scattering models are not always straightforward to comprehend and implement.

1.6.5.2 Contribution

This dissertation contributes to the body of knowledge by using signal-flow graph theory to (1) to derive the non-coherent steady-state radiative transfer for stratified dielectrics with any number of layers, and (2) to provide executional clarity to graphically represent the iterative process that explains the coherent radiative transfer within multi-layered dielectrics. To the best of the author's knowledge, this is the first time that these approaches have been used to explain the radiative transfer within multi-layered media with non-uniform temperature distributions.

1.7 Organization of Dissertation

This dissertation is organized as follows: Chapter 2 introduces the principles necessary for microwave remote sensing. Chapter 3 highlights the impact that system isolation plays on

www.manaraa.com

extracting noise temperature while using various forms of a perfectly-isolated radiometer system equation. Chapter 4 presents the development of a highly reproducible human tissue-mimicking phantom recipe (comprised of urethane, graphite powder, and a solvent) designed to accurately emulate different human body tissues with varying water concentrations. Chapter 5 highlights the result of the inclusion of an in-plane electromagnetic bandgap structure within an on-body inward facing spiral antenna design and demonstrates an improvement in the antenna radiation characteristics. Chapter 6 presents two techniques designed to address both the modeling of the coherent and non-coherent radiative transfer within multi-layered media. Chapter 7 validates the derived radiative transfer models with a comparison to the extracted apparent temperature detected by a microwave radiometer. The dissertation concludes with Chapter 8 and offers suggestions for future work.

www.manaraa.com

Chapter 2 Remote Temperature Sensing Using Microwave Radiometry

2.1 Introduction

Principles essential to microwave radiometric remote sensing are introduced. The concepts presented in this chapter are primarily adapted from [28] unless otherwise noted.

2.2 Background - Overview of Microwave Radiometry

All matter at non-zero absolute temperatures emits electromagnetic (EM) energy. Radiometry is the field of science associated with the measurement of this emitted electromagnetic radiation. A microwave (MW) radiometer is a very sensitive receiver designed to passively measure noise power in the MW frequency range. Ultimately, the EM energy that is detected by the radiometer is correlated to an absolute temperature.

The origin of microwave radiometry can be traced back to the 1900's when Max Planck proposed the blackbody radiation law. Planck's blackbody radiation law describes the amount of electromagnetic energy radiated by a blackbody, in terms of the spectral brightness per solid angle, at a particular wavelength and in thermal equilibrium with its environment. Planck's blackbody radiation law can be seen by

$$B_f^P = \frac{2hf^3}{c^2}\left(e^{hf/kT} - 1\right)^{-1}, \tag{2.1}$$

where B_f^P is the blackbody spectral brightness [W·m^{-2}·sr^{-1}·Hz^{-1}], h is Planck's constant = 6.63 × 10^{-34} [J·s], f is the frequency [Hz], k is Boltzmann's constant = 1.38 × 10^{-23} [J·K^{-1}], T is the absolute temperature [K], and c is the speed of light = 3 × 10^{8} [m·s^{-1}].

A blackbody is defined as an ideal, perfectly opaque object that isotopically absorbs all incoming radiation at all frequencies and in turn reemits the radiation with perfect efficiency in

www.manaraa.com

order to maintain thermal equilibrium. At lower frequencies (where $hf/kT << 1$), EM energy is log-linear with respect to frequency. Planck's Law is approximated at lower frequencies by the Raleigh-Jeans' Law, in the form of

$$B_f^R = \frac{2f^2kT}{c^2}, \tag{2.2}$$

where B_f^R is the blackbody spectral brightness under the Raleigh-Jeans' approximation. At higher frequencies (where $hf/kT >> 1$), Planck's Law is approximated by Wein's Law, given by

$$B_f^W = \frac{2hf^3}{c^2} e^{-hf/kT}, \tag{2.3}$$

where B_f^W is the blackbody spectral brightness under Wein's approximation. Figure 2.1 describes the frequency dependence of the spectral brightness for Planck's Law at 300K. The corresponding brightness curves for both the Raleigh-Jeans' and Wien's Law are also depicted for comparison. At room temperature ($T \approx 300$ K) and up to a frequency of 300 GHz, the Rayleigh-Jeans approximation deviates by less than three percent from the value dictated by Planck's Law, thus making it a valid assumption in the microwave frequency range. Absorbing materials found in anechoic chambers provide a good representation for an ideal blackbody at MW frequencies.

All physical temperatures are herein denoted by either a lowercase subscript (e.g. T_{sub}) or no subscript (e.g. T) to avoid any confusion with naming conventions associated with physical and radiometric temperatures. Conversely, all radiometric temperatures are denoted by uppercase subscripts (e.g. T_{SUB}).

For a narrow bandwidth Δf in the microwave region, the brightness B_{bb} of a blackbody at temperature T is given by, from equation (2.2),

$$B_{bb} = B_f^R \cdot \Delta f = \frac{2f^2kT}{c^2}\Delta f. \tag{2.4}$$

Since most natural objects are non-ideal or imperfect emitters, called greybodies, the efficiency of emitted electromagnetic radiation is less than that of an ideal blackbody. This reduced efficiency of

www.manaraa.com

an imperfect radiator is called emissivity $e(\theta,\phi)$. Emissivity is defined as the ratio of the observed brightness of a greybody $B(\theta,\phi)$, which is a function of direction, relative to that of an ideal blackbody at the same temperature, as seen by

$$e(\theta,\phi) = \frac{B(\theta,\phi)}{B_{bb}}, \tag{2.5}$$

with

$$B(\theta,\phi) = \frac{2f^2k}{c^2} \cdot T_B(\theta,\phi) \cdot \Delta f, \tag{2.6}$$

and $B(\theta,\phi) \leq B_{bb}$ and $0 \leq e(\theta,\phi) \leq 1$, where $T_B(\theta,\phi)$ is the radiometric equivalent brightness temperature. Employing the above relationships, it is noticed that the brightness temperature of a greybody is defined as the corresponding blackbody physical temperature reduced by the greybody efficiency of emission in

$$T_B(\theta,\phi) = T \cdot e(\theta,\phi). \tag{2.7}$$

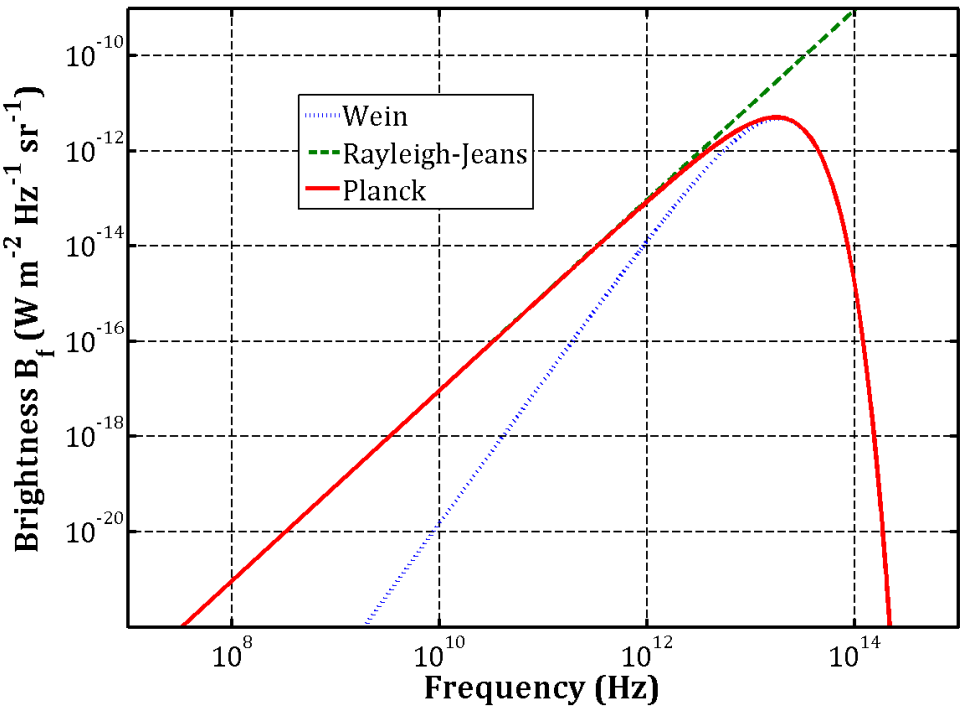

Figure 2.1 Comparison of Planck's law with both the low frequency (Rayleigh-Jeans law) and high frequency (Wien's law) approximations of spectral brightness at 300 K.

www.manaraa.com

Figure 2.2 illustrates both the isotropic thermal emissions from an ideal blackbody and the angular dependence of the brightness temperature emitted by a semi-infinite isothermal greybody medium.

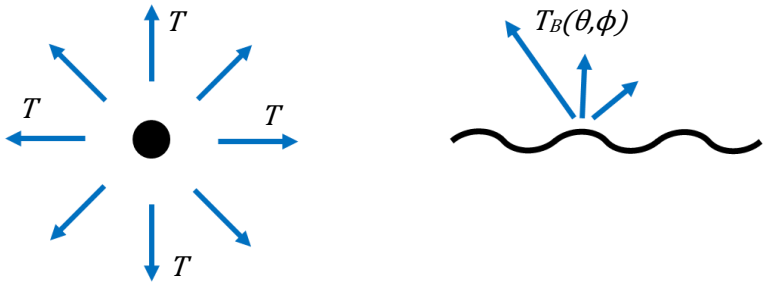

Figure 2.2 Thermal emissions from an isotopically radiating ideal blackbody (left) and a direction-dependent semi-infinite greybody (right).

Extending the greybody emission concept from above to apply to a lossy two-layer medium, a relationship between reflectivity Γ, emissivity ϵ, and transmissivity Υ can be established. As Figure 2.3 illustrates, the first law of thermodynamics requires that the incident radiation must be equal to the sum of the reflected, absorbed, and transmitted radiation [28, 29], given by

$$\begin{aligned} P_{inc} &= P_{refl} + P_{abs} + P_{trans} \\ &= \Gamma \cdot P_{inc} + \epsilon \cdot P_{inc} + \Upsilon \cdot P_{inc}. \end{aligned} \tag{2.8}$$

where P_{inc} is the incident radiation, $P_{reflc} = \Gamma \cdot P_{inc}$ is the reflected radiation, $P_{abs} = \epsilon \cdot P_{inc}$ is the absorbed radiation, and $P_{trans} = \Upsilon \cdot P_{inc}$ is the transmitted radiation. Normalizing equation (2.8), it is seen that the sum of the emissivity, transmissivity, and reflectivity must be equal to unity in order to satisfy the conservation of energy (*i.e.* $1 = \epsilon + \Gamma + \Upsilon$). For a lossy two-layer medium, emissivity, transmissivity, and reflectivity are related to the brightness temperature T_B by

$$\begin{aligned} T_{inc} &= T_{refl} + (T_{abs} + T_{trans}) \\ \therefore T_{AP} &= \Gamma \cdot T_0 + (T_B) \\ &= \Gamma \cdot T_0 + (\epsilon \cdot T_1 + \Upsilon \cdot T_2). \end{aligned} \tag{2.9}$$

where T_{AP} is the apparent temperature, T_B is the brightness temperature, and T_0, T_1, and T_2 are the physical temperatures of layer's 0, 1 and 2, respectively.

www.manaraa.com

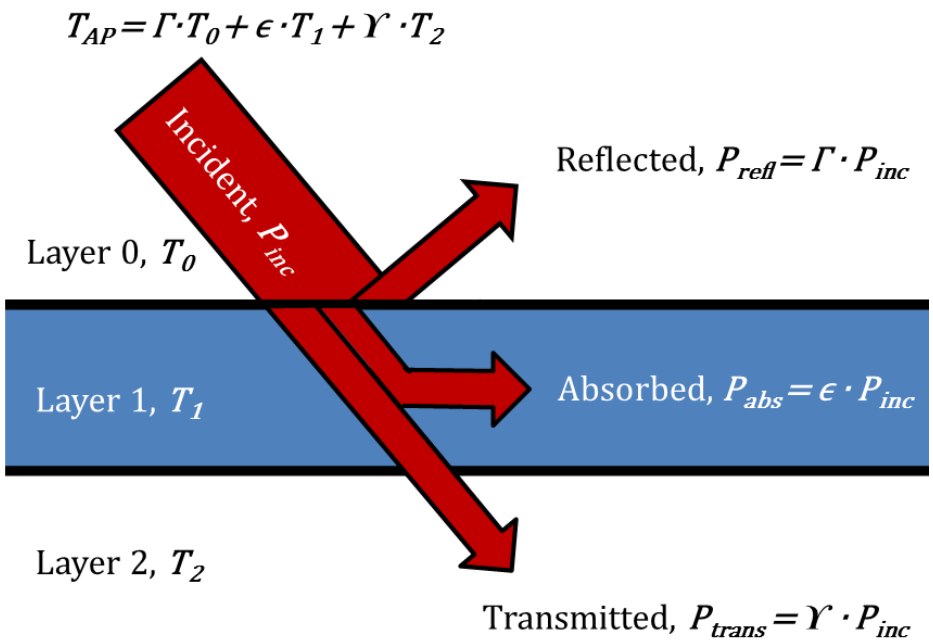

Figure 2.3 The reflection, absorption, and transmission of incident radiation for a lossy two-layer medium. To satisfy conservation of energy, the incident radiation must be equal to the sum of the reflected, absorbed, and transmitted radiation, $P_{inc} = P_{reflc} + P_{abs} + P_{trans}$. Likewise, the apparent temperature is the sum of (1) the reflected portion multiplied by the layer 0 temperature, (2) the absorbed portion multiplied by the layer 1 temperature, and (3) the transmitted portion multiplied by the layer 2 temperature.

2.2.1 Relationship between Temperature and Power

So far, brightness has only been expressed in terms of temperature. Conveniently, power and temperature have a direct linear relationship which allows for these two terms to be used interchangeably. This power-temperature relationship can be understood by observing the maximum power transfer from a noisy resistor placed inside a blackbody enclosure (Figure 2.4(a)) at a constant temperature T, cascaded with an ideal bandpass filter (BPF) with bandwidth Δf and terminated in a matched load R, denoted as

$$P_n = V_n I = \left(\frac{V_{rms}}{2}\right)\left(\frac{V_{rms}}{2R}\right) = \frac{V_{rms}^2}{4R} = \frac{4kTR\Delta f}{4R} = kT\Delta f, \tag{2.10}$$

where P_n is the available spectral noise power [W], $V_n = \frac{V_{rms}}{2} = \frac{1}{2}\sqrt{4kTR\Delta f}$ is the RMS voltage produced by the noisy resistor [V], R is the resistance of load [Ω], k is Boltzmann's constant, and T is the physical temperature of the resistor. The above resistor to BPF to load relationship (Figure

www.manaraa.com

2.4a) is also analogous to a lossless antenna placed inside a blackbody enclosure (Figure 2.4(b)) at a constant temperature T where the detected power is limited to a bandwidth such that the blackbody spectral brightness B_f is approximately constant over the bandwidth. Taking into account the pattern solid angle of the antenna, the power received by the antenna due to emission by the blackbody enclosure results in

$$P_{bb} = kT\Delta f, \tag{2.11}$$

where P_{bb} is the total received power of the antenna with respect to the directional distribution of the spectral brightness.

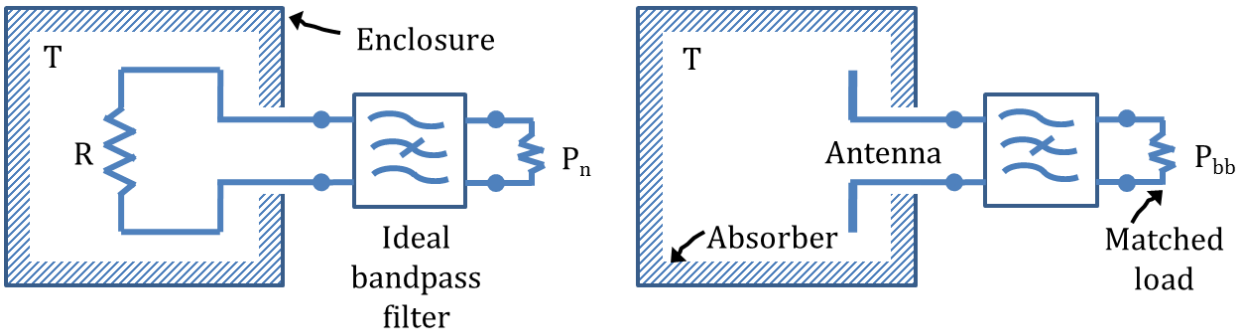

(a) (b)

Figure 2.4 The noise power P_n delivered by (a) a resistor maintained at temperature T in a black body enclosure is equivalent to the power received P_{bb} by (b) an antenna at the same temperature T. All devices are connected to an ideal bandpass filter of bandwidth Δf and terminated in a matched load R.

2.2.2 Basic Radiometer Operation

Now, instead of a BPF, consider an ideal total power radiometer system as depicted in Figure 2.5. The output noise power of a total power radiometer system with overall gain G and bandwidth Δf, connected in cascade with a lossy antenna, is given by

$$P = k(T_A + T_{REC})\,\Delta f \cdot G, \tag{2.12}$$

where T_A is the radiometer noise temperature detected by the antenna which equals to the resistor-equivalent temperature that would deliver the same output power (this includes the brightness temperature contribution) and T_{REC} is the radiometer receiver's overall input noise temperature.

www.manaraa.com

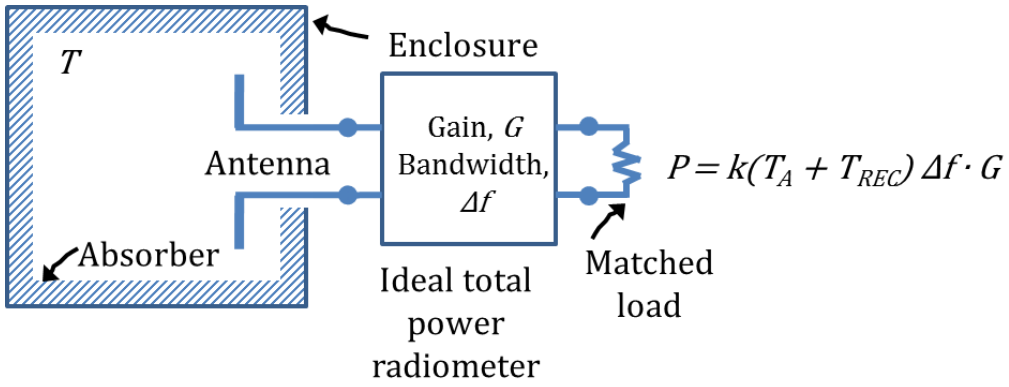

Figure 2.5 The power P received by an antenna connected to a total power radiometer with gain G and bandwidth Δf where T_A and T_{REC} are the antenna and the overall receiver radiometric input noise temperature, respectively.

For a lossy antenna, part of the energy is received at the output of the antenna and another part is absorbed by the antenna material in the form of heat loss. Subsequently, the effective apparent temperature $T_{AP,eff}$ of the background scene is resolved from T_A in a far-field scenario by accounting for the antenna radiation efficiency η_{rad} and the antenna physical temperature T_p, as seen in

$$T_A = \eta_{rad} T_{AP,eff} + (1 - \eta_{rad}) T_p. \tag{2.13}$$

The relationship described in equation (2.13) assumes that the antenna radiation pattern is ideal (that the antenna has one main-lobe with no side-lobes), but in reality, the antenna receives thermal emissions from both the main and side-beams. This suggests that the portion of the energy received by the antenna can be expressed as the sum of both the main and side-lobe contributions, as in

$$\begin{aligned} T_{AP,eff} &= \eta_{ML} \bar{T}_{ML} + \eta_{SL} \bar{T}_{SL} \\ &= \eta_{ML} \bar{T}_{ML} + (1 - \eta_{ML}) \bar{T}_{SL} \\ &= \eta_{ML} T_{AP} + (1 - \eta_{ML}) T_a, \end{aligned} \tag{2.14}$$

where $\bar{T}_{ML}$ is the main-lobe contribution which is equivalent to the apparent brightness temperature of the scene T_{AP}, η_{ML} is the main-beam efficiency, $\bar{T}_{SL}$ is the effective temperature of the side-lobe contribution which is equivalent to the ambient temperature T_a, and η_{SL} is the side-beam efficiency. Combining equations (2.13) and (2.14) gives

www.manaraa.com

$$T_A = \eta_{rad}\eta_{ML}\bar{T}_{ML} + \eta_{rad}(1-\eta_{ML})\bar{T}_{SL} + (1-\eta_{rad})T_p, \\ = \eta_{rad}\eta_{ML}T_{AP} + \eta_{rad}(1-\eta_{ML})T_a + (1-\eta_{rad})T_p. \quad (2.15)$$

Effectively, the quantity $\bar{T}_{ML}$ (the apparent brightness temperature of the scene T_{AP}) is estimated from the measured quantity T_A (the radiometric antenna temperature). The relationship in Equation (2.15) implies that $T_A = T_{AP}$ for a lossless antenna (where $\eta_{ML} = \eta_{rad} = 1$). The radiometric antenna temperature can be further improved by employing additional corrections for the antenna path losses as derived in [28]. The calculation of both the antenna radiation efficiency η_{rad} and main-lobe efficiency η_{ML} is further described in Appendix A.

2.2.3 Typical Radiometer Configurations (Adapted from [30])

The most commonly utilized classes of radiometers include the total power radiometer (TPR) and the Dicke radiometer. Both radiometer types are outlined in Table 2.1. The front-end of the TPR is similar to the frontend of a standard superheterodyne receiver in that it contains an RF amplifier, a mixer and local oscillator, an IF filter, an IF amplifier, and a square law detector [30]. The amplifier strengthens the signal received from the antenna. After amplification, the mixer shifts the input frequency to a more desirable frequency range. This desired frequency range is determined by the local oscillator frequency. The IF filter selects the desired frequency band of use and rejects any unwanted frequency bands. The square law detector gives a DC component at the detector output that is proportional to the square of the AC input voltage. The back-end of the TPR only contains an integrator (low pass filter). The integrator filters out the ac components in the output voltage that contain frequency components greater than the inverse of the integration constant τ. Table 2.1 also outlines the typical errors in the measured T_B associated with the TPR. These errors include both the error due to noise fluctuations ΔT_N and the error due to gain variations ΔT_G. The error due to gain variations is more detrimental to the radiometer system accuracy because gain variations can be ten or more times greater than the noise fluctuations as shown by [30]. The error due to noise fluctuations can be reduced by increasing either the

www.manaraa.com

integration time, bandwidth, or by minimizing the receiver internal noise contribution. The error due to gain fluctuations in a radiometer system is reduced by repeatedly calibrating the radiometer at a rapid rate. This repeated calibration technique is the basis behind the Dicke null-balancing radiometer. The front-end of the Dicke radiometer is identical to the TPR, however, the input is periodically switched between the antenna and a variable power noise source [30]. The back-end of the balanced Dicke radiometer contains a synchronous demodulator (a switch and difference circuit) that operates in sync with the Dicke switch. The output of the difference circuit is used as an error signal to control a feedback circuit. The errors due to noise fluctuations and gain variations are outlined in Table 2.1. Other radiometer configurations are discussed in [28].

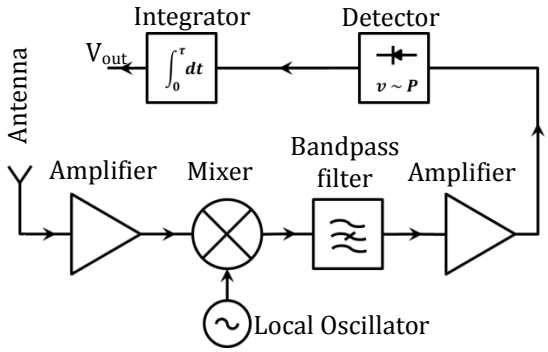

Figure 2.6 Diagram of total power radiometer.

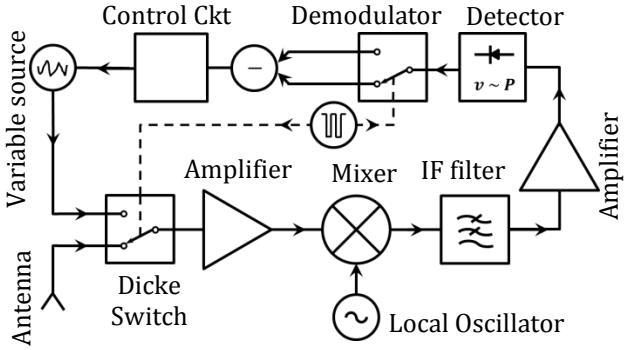

Figure 2.7 Diagram of Dicke radiometer.

Table 2.1 Total power radiometer (left) vs Dicke radiometer (right) characteristics

Parameter	Total power radiometer	Dicke radiometer
Output Voltage	$V_{out} = k(T_A + T_{REC})\Delta f \cdot G$ where T_{REC} is the receiver effective noise temperature.	$V_{out} = \frac{1}{2}(T_A - T_{REF})G$ where T_{REF} is the reference noise temperature.
Sensitivity/ noise fluctuation error	$\Delta T = \frac{T_A + T_{REC}}{\sqrt{\Delta f \cdot \tau}}$	$\Delta T = 2\frac{T_A + T_{REF}}{\sqrt{\Delta f \cdot \tau}}$
Calibration	Insert two calibrated noise sources	Rapid and repeated switching between the antenna and variable power source

2.2.4 Radiometer Calibration

The total power radiometer is calibrated with two reference sources with known noise temperatures that are used to find an unknown noise temperature for a device under test (DUT).

www.manaraa.com

Since noise power in the microwave region is linear, the calibration process is ultimately a linear interpolation of the two known calibration temperatures (assuming an isolated radiometer with constant system gain across frequency, constant path losses, and constant mismatch for all devices) as given by Figure 2.8. The unknown DUT noise temperature is resolved using

$$\begin{aligned} T_{DUT} &= T_C + (T_H - T_C) \cdot \frac{P_{DUT}^{del} - P_{COLD}^{del}}{P_{HOT}^{del} - P_{COLD}^{del}} \\ &= T_C + (T_H - T_C) \cdot \frac{Y_{DUT} - 1}{Y_{HOT} - 1} \end{aligned} \tag{2.16}$$

where T_{DUT} is the noise temperature for the device under test, T_H is the noise temperature for the hot calibration reference source, T_C is the noise temperature for the cold calibration reference source, Y_{DUT} is the DUT Y-factor which is the ratio of the DUT delivered noise power to the cold source delivered noise power $P_{DUT}^{del}/P_{COLD}^{del}$, and Y_{HOT} is the hot load Y-factor which is the ratio of the hot source delivered noise power to the cold source delivered noise power $P_{HOT}^{del}/P_{COLD}^{del}$. Noise temperatures are related to the available power by $P_{HOT}^{av} = k \cdot \Delta f \cdot T_H$. Conversely, effective noise temperatures are related to the delivered noise power through the same relationship. Equation (2.16) assumes an isolated radiometer with constant system gain across frequency, constant path losses, and constant mismatch for all devices, but for radiometer system equations with dissimilar path losses and dissimilar mismatch for all devices are discussed in Section 3.3.

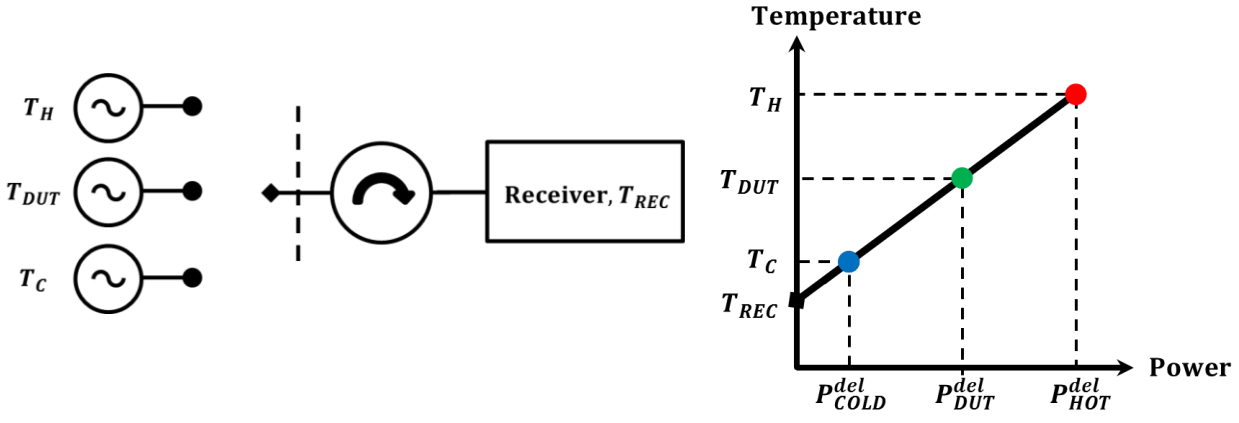

Figure 2.8 Calibration of a total power radiometer including the setup (left) and the plotted noise temperatures versus delivered powers (right).

www.manaraa.com

A diode-based noise source is a possible option to use for the hot noise source. In this work, Noisecom's NC346B diode-based noise source with a nominal excess noise ratio (ENR) of 15 dB is used for the hot noise source. Calibrated noise sources are typically specified in terms of the effective hot noise temperature as opposed to the hot noise temperature T_H [31], where $T_H^{eff} = T_H \cdot (1 - |R_{HOT}|^2)$ and R_{HOT} is the reflection coefficient of the noise source. The effective noise temperature of the hot noise source T_H^{eff}, corrected for an ambient temperature T_a that is different than the reference temperature T_{REF}, is related to the calibrated ENR [32], by

$$\begin{aligned} ENR_{corr} &= \left(T_H^{eff} - T_a\right)/T_{REF} \\ &= ENR_{cal} + ENR_{deltaT} \\ &= 10^{(ENR_{cal}^{dB}/10)} + \frac{T_{REF} - T_a}{T_{REF}} \end{aligned} \tag{2.17}$$

where ENR_{corr} is the corrected ENR value, ENR^{dB}_{cal} is the original calibrated ENR value in decibels, ENR_{cal} is the original calibrated ENR value, and ENR_{deltaT} is the correction factor for an ambient temperature that is different than the reference temperature T_{ref} in Kelvin [K].

2.2.5 Radiometric Sensing and the Electromagnetic Spectrum

Optimal radiometric sensing frequencies are dependent on the size of the antenna structure, the desired depth of penetration into the body, and the potential presence of excess signals which cause unwanted electromagnetic interference (EMI). The Federal Communications Commission (FCC) regulates certain frequency bands within the EM spectrum to be allocated for passive space research and radio-astronomy. These aforementioned FCC allocated frequency bands provide the necessary protection from any unwanted EMI frequencies. A few passive space research and radio-astronomy frequency bands include: 406.1 MHz – 410 MHz, 608 MHz – 614 MHz, 1400 MHz – 1427 MHz, 1660.5 MHz – 1668.4 MHz, 2655 MHz – 2700 MHz, 4990 MHz – 5000 MHz , and 18.6 GHz – 18.8 GHz. While the passive space research and radio-astronomy frequency bands offer undisturbed frequency ranges, the desired penetration depth for the specific application also has a bearing on the optimal radiometric sensing frequency.

www.manaraa.com

2.2.6 Radiometric Sensing of Biological Materials

A unique feature of microwave radiometry is that the radiometric output seen by the antenna provides a weighted average of the distributed profile for all thermal emissions contributed by all observed strata down to a maximum sensing depth. The sensing depth is commonly defined as the depth at which the plane-wave penetration has decayed to *1/e* (~36.79%) of the surface value. The penetration depth of a radiometric system mainly depends on the relative permittivity and the frequency of the biological material under investigation. A simple human body volume can be modeled by the skin, fat and muscle tissue layers. The electromagnetic properties of interest for these tissues are governed by the complex permittivity

$$\varepsilon^* = \varepsilon_0 \cdot \varepsilon_r = \varepsilon_0 \cdot [\varepsilon_r' - j\varepsilon_r''] = \varepsilon_0 \cdot [\varepsilon_r' - j\varepsilon' \cdot tan\delta], \tag{2.18}$$

where ε_r is the complex relative permittivity, ε_0 is the permittivity of free space, ε_r' is the real part of the relative permittivity or the dielectric constant which is the ability of a substance to store electrical energy amid an electric field, ε_r'' is the imaginary part of the relative permittivity which is the ability of a substance to dissipate electrical energy amid an electric field, and $tan\delta$ is the loss tangent which is the ratio between the real and imaginary permittivities. Gabriel's documented electrical characteristics of biological materials are taken as the golden standard for the EM properties of human tissues [33-36]. Figure 2.9 shows the dielectric constants and skin-depths for skin, fat and muscle over a frequency range of 0.1 GHz to 18 GHz. Table 2.2 highlights selected penetration depths [37] of several biological tissues at specific frequencies. In general, the penetration depth increases as frequency decreases. As the trend from Figure 2.9 suggests, the areas of the body with higher fatty compositions allow for deeper sensing depths. Typically, a radiometer system can observe depths of about 1.4 to 5.7cm beneath the skin's surface from 410 MHz to 5 GHz, given the placement of the sensor on a human body volume comprised of 3.3mm of skin tissue and 6.25mm of fat tissue. The penetration depth for a multi-layered dielectric can be found with

www.manaraa.com

$$d_N = \left(Decay - \sum_{j=1}^{N-1} \alpha_j d_j \right) \Big/ \alpha_N,$$
$$d_{pen} = \sum_{j=1}^{N} d_j \tag{2.19}$$

where d_{pen} is total penetration depth, N is the total number of layers, α_N and d_N are the attenuation coefficient and thickness, respectively, for the N-th layer, *Decay* is the exponential order of the decay (*e.g.* a *Decay* value of 1 corresponds to $e^{-1} = 36.79\%$ and a *Decay* value of 2 corresponds to $e^{-2} = 13.53\%$), and α_j and d_j are the attenuation coefficient and thickness, respectively, for the j-th layer.

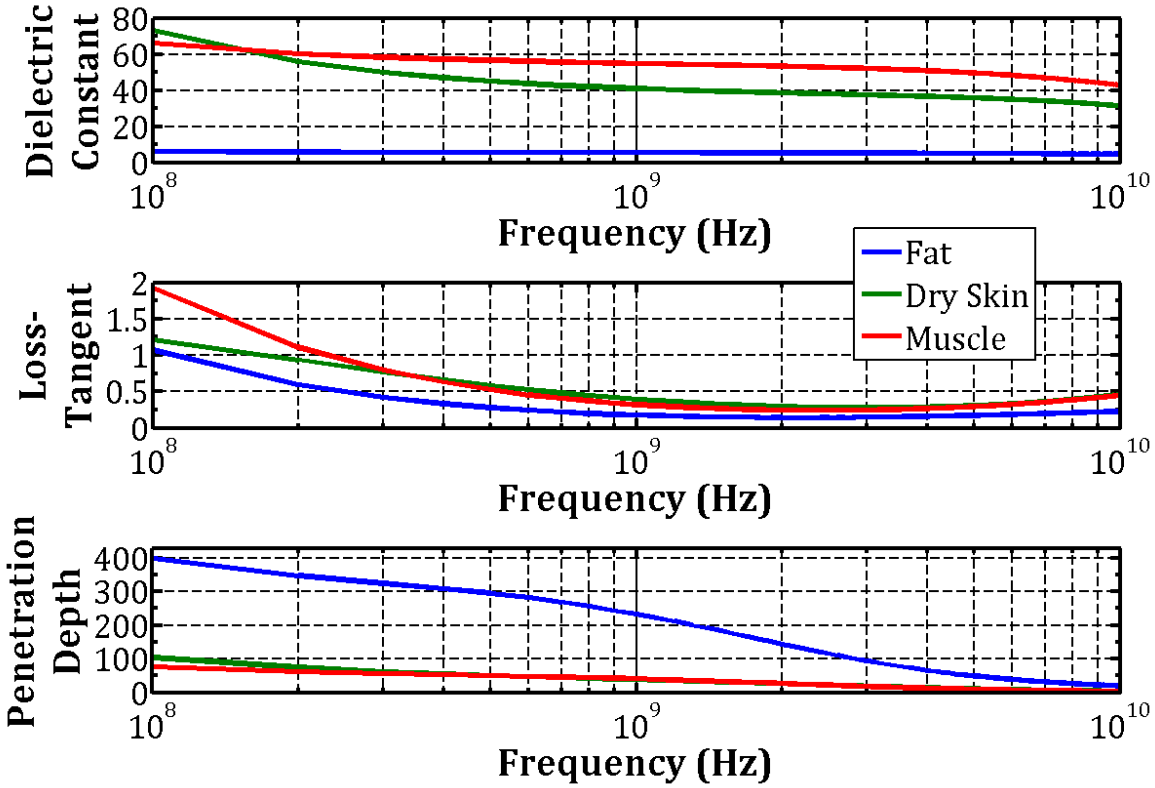

Figure 2.9 Frequency dependent dielectric constant (top), loss-tangent (middle), and penetration-depth (bottom) for biological tissues.

www.manaraa.com

Table 2.2 Penetration depths d_{pen} for tissues at select protected (passive space research and radio-astronomy) frequency bands

Frequency	Tissue			
	Dry Skin	Fat	Muscle	Total dpen beneath skin for Skin (3.3 mm), Fat (6.25 mm), and Muscle (infinite)
410 MHz	~ 54. 8 mm	~ 309 mm	~ 52.6 mm	~ 57.3 mm
610 MHz	~ 47.0 mm	~ 269 mm	~ 45.9 mm	~ 53.3 mm
1.4 GHz	~ 32.7 mm	~ 191 mm	~ 34.5 mm	~ 39.6 mm
1.665 GHz	~ 29.7 mm	~ 173 mm	~ 30.4 mm	~ 36 mm
2.7 GHz	~ 20.8 mm	~ 105 mm	~ 20.2 mm	~ 25.3 mm
5.0 GHz	~ 10.5 mm	~ 40.5 mm	~ 7.54 mm	~ 14.45 mm
18.6 GHz	~ 1.52 mm	~ 9.5 mm	~ 1.42 mm	~ 1.52 mm

2.3 Review of Microwave Biomedical Radiometry Applications

Microwave radiometry used for biomedical applications can be broadly divided into four categories: (A) sensing, (B) monitoring, (C) diagnostics, and (D) treatment. These categories were adapted from publications distributed from the IEEE Microwave Theory and Techniques Society (MTT-S) Technical Committee on the Biological Effect and Medical Applications of Radio Frequency (RF) and Microwaves [38-40]. Each category is defined below and corresponding applications are overviewed.

(A) Sensing refers to the detection of events or changes in a quantity. Some notable sensing applications involving MW radiometry include: cancer detection [41-43], detection of vesicoureteral reflux [26, 44-46], and detection of venerable plaque [47].

(B) Monitoring includes the observation, checking, and keeping a continuous record of a process or quantity. Some monitoring works involving MW radiometry consist of: core temperature monitoring [12-14, 48], monitoring neck and head diseases [49], monitoring of deep brain tissue [18, 19, 23, 24, 50], blood glucose monitoring [51], and monitoring of brown adipose tissue (BAT) metabolism [25].

www.manaraa.com

(C) Diagnostics refers to the identification of the nature of an illness or other problem by examination of the symptoms. Noteworthy diagnostics works involving MW radiometry include: diagnosing arthritis from joint inflammation by detecting elevated temperatures [52-54].

(D) Treatment/therapy includes the medical care given to a patient for an illness or injury. Some notable treatment applications involving MW radiometry consists of: monitoring the thermal doses delivered during cancer treatments [15, 55] and temperature control during hyperthermia treatments [20].

Also, exhaustive historical reviews on the applications for microwave biomedical radiometry can be found in [56-58].

www.manaraa.com

Chapter 3 Radiometer Calibration and System Equation Analysis

3.1 Introduction

As Section 2.2 illustrates, an unknown DUT noise temperature can be predicted using a radiometer calibration equation where two known reference sources are available. Three possible calibration sources can be used to form calibration combination pairs, either an ambient temperature (T_a), a cold temperature ($T_C < T_a$), or a hot temperature ($T_H > T_a$) reference source. These source temperatures can either represent physical temperatures or equivalent electrical temperatures. The classic radiometer calibration utilizes a source combination pair between either an ambient and hot source temperature $T_a : T_H$ or a cold and ambient source temperature $T_C : T_a$ [59-61]. However, any uncertainty in the actual value of the ambient source temperature can result in prediction errors for devices that are colder (for the $T_a : T_H$ source combination) or hotter (for the $T_C : T_a$ source combination) than the ambient source. The widest dynamic range able to cover the most possible noise temperature extractions comes from the source combination of $T_C : T_H$ calibration sources (assuming that the receiver linearity is of no concern). However, most radiometer system equations (RSEs) do not provide an option to simultaneously use both a hot and cold source temperature within the calibration routine.

Radiometer calibrations (*i.e.* noise power measurements) can be implemented with four general radiometer set-ups as shown in Figure 3.1. Temperature sources can be connected either directly or indirectly (*e.g.* separated by a lossy two-port device) to the radiometric receiver with the additional option to be perfectly-isolated or imperfectly-isolated (where the non-isolated case is the absolute state for the imperfectly-isolated case). Each scenario can have similar or dissimilar front-end path losses and source mismatches. The front-end in this case is considered to be every

www.manaraa.com

device before the radiometric receiver's pre-amplifier, not including the temperature source. The most general scenario is an indirectly-connected and non-isolated radiometer set-up, where all other scenarios have multiple assumptions applied which lead to its final form. While the isolated RSE assumption is limited by the usable bandwidth of the physical isolator, it makes for ideal simplifications which do not apply while using the non-isolated assumption. For example, for a non-isolated receiver, the receiver's effective input temperature T_{eff} becomes a function of the source mismatch [62, 63]. However, this is not the case for an isolated receiver as the assumption is no source mismatch affecting T_{eff}. For this reason, this study will only focus on isolated radiometers.

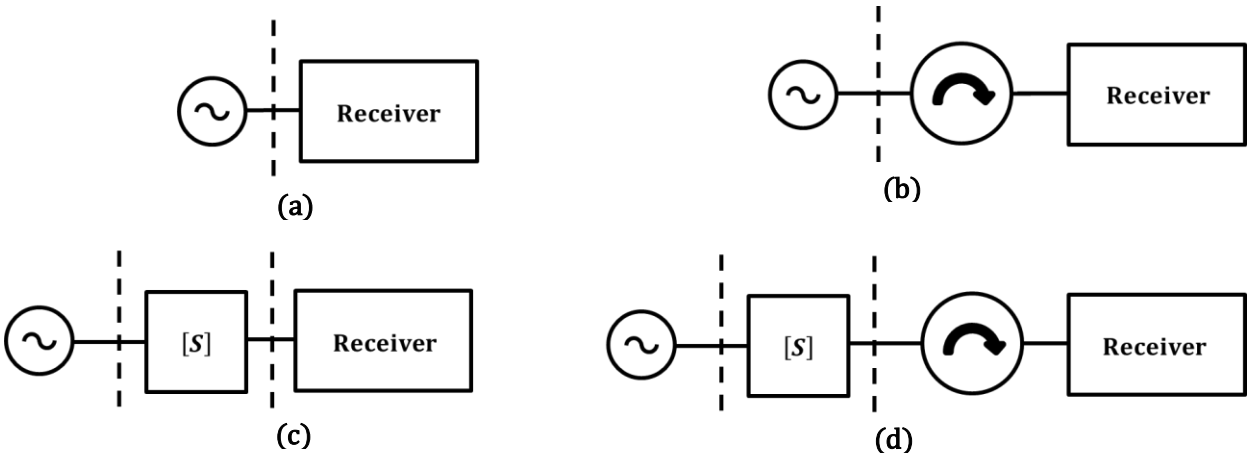

Figure 3.1 The four possible noise temperature measurement set-ups: (a) directly-connected and non-isolated, (b) directly-connected and isolated, (c) indirectly-connected and non-isolated, (d) indirectly-connected and isolated.

This work derives an indirectly-connected, perfectly-isolated, fully-corrected RSE that accounts for all available noise source combinations. Varying assumptions are applied which lead to simpler, more convenient forms of the RSE. Noise temperature is extracted for an unknown DUT using varying amounts of system isolation and in conjunction with each form of the RSE. Prediction accuracy is accessed for each combination of the RSE with the resulting system isolation.

This chapter highlights the impact that system isolation plays on extracting noise temperature while using various forms of the perfectly-isolated radiometer system equation.

www.manaraa.com

Section 3.2 overviews the relevant literature available in deriving radiometer system equations. Section 3.3 derives a generic isolated radiometer system equation and explains the relevance of underlying assumptions. Section 3.4 analyzes and validates the derived radiometer system equations with an electromagnetic circuit simulation. This chapter concludes with Section 3.5.

3.2 Review of Relevant Radiometer System Equation (RSE) Literature

A review of the relevant literature on the derivation of RSEs is presented. Gaps in previous literature as well as the contributions from the outcomes of this work are addressed.

3.2.1 Background

The basic principles behind noise power measurements for a mismatched source connected to a two-port network that is terminated in a load are described in references [64-66]. Naming conventions from reference [64] have been mixed with the conventions from reference [62] for improved cohesion. Figure 3.2 shows the basic noise measurement system with the schematic representation of a noise source with impedance Z_S in-cascade with a two-port network (with scattering matrix S and characteristic line impedances of Z_1 and Z_2) that is terminated in a load with impedance Z_L. The following reflection coefficients are present for the source Γ_S, the load Γ_L, looking into port 1 from the left side Γ_1, and looking into port 2 from the right side Γ_2. The net spectral power delivered (denoted by P^{del}) to the right of reference planes 1 and 2 are P_1^{del} and P_2^{del}, respectively. The mismatch factors M_1 and M_2 at reference planes 1 and 2, respectively, are defined as the ratios of the delivered spectral power to the available spectral power (denoted by P^{av}), given by

$$\begin{aligned} M_1 &= \frac{P_1^{del}}{P_1^{av}} = \frac{(1-|\Gamma_S|^2)(1-|\Gamma_1|^2)}{|1-\Gamma_S\Gamma_1|^2}, \\ M_2 &= \frac{P_2^{del}}{P_2^{av}} = \frac{(1-|\Gamma_L|^2)(1-|\Gamma_2|^2)}{|1-\Gamma_L\Gamma_2|^2}. \end{aligned} \tag{3.1}$$

The efficiency $\eta_{21}\left(P_2^{del}/P_1^{del}\right)$ and the available power ratio $\alpha_{21}\left(P_2^{av}/P_1^{av}\right)$ are

www.manaraa.com

$$\eta_{21} = \frac{P_2^{del}}{P_1^{del}} = \frac{(Z_1/Z_2)(1-|\Gamma_L|^2)\cdot|S_{21}|^2}{(1-|\Gamma_1|^2)\cdot|1-S_{22}\Gamma_L|^2},$$
$$\alpha_{21} = \frac{P_2^{av}}{P_1^{av}} = \frac{M_1\cdot\eta_{21}}{M_2} = \frac{(Z_1/Z_2)(1-|\Gamma_S|^2)\cdot|S_{21}|^2}{(1-|\Gamma_2|^2)\cdot|1-S_{11}\Gamma_S|^2}. \quad (3.2)$$

The available power at reference plane 1 P_1^{av} is related to the delivered power at reference plane 2 P_2^{del} by

$$P_2^{del} = M_2[P_2^{av}] = M_2[\alpha_{21}P_1^{av} + (1-\alpha_{21})P_a]. \quad (3.3)$$

where P_a is the noise power generated by the two-port network at an ambient physical temperature T_a.

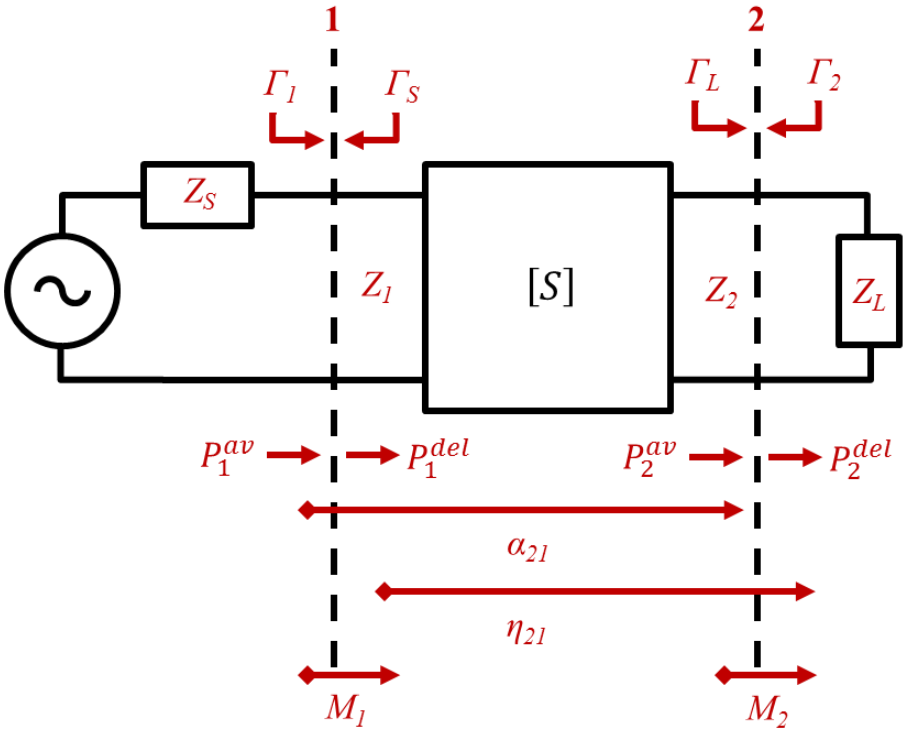

Figure 3.2 Schematic representation of a mismatched noise source with impedance Z_S in-cascade with a two-port network (with scattering matrix S and characteristic line impedances of Z_1 and Z_2) that is terminated in a load with impedance Z_L.

The aforementioned noise theory led to the seminal derivation of the radiometer system equation (RSE) by the National Institutes of Standards and Technology (NIST) [67, 68] where two sources with known delivered powers are used to determine the noise temperature of an unknown source. A similar treatment by other scientists at NIST was used in [59, 60] to derive a system

www.manaraa.com

equation for a radiometer (Figure 3.3) where three sources are connected to a single-pole triple-throw (SP3T) switch cascaded with a well-isolated radiometric receiver (herein referred to as an indirectly-connected, well-isolated radiometer set-up). The classic RSE for the indirectly-connected, perfectly-isolated, partially-corrected condition (assuming the cold source is at an ambient temperature T_a) is

$$\begin{aligned} T_X &= T_a + (T_H - T_a)\,\frac{\mathrm{M}_{out,h}\cdot\alpha_{out,h}}{\mathrm{M}_{out,x}\cdot\alpha_{out,x}}\,\frac{\mathrm{Y}_x - 1}{\mathrm{Y}_h - 1} + \cancel{(\Delta T_x)_{iso}} \\ &= T_a + (T_H - T_a)\,\frac{\mathrm{M}_{out,h}\cdot\alpha_{out,h}}{\mathrm{M}_{out,x}\cdot\alpha_{out,x}}\,\frac{\mathrm{Y}_x - 1}{\mathrm{Y}_h - 1}, \end{aligned} \tag{3.4}$$

where the DUT Y-factor is $Y_x = P_x^{del}/P_a^{del}$, the hot standard Y-factor is $Y_h = P_h^{del}/P_a^{del}$, T_h is the available noise temperature of the hot source, T_X is the available noise temperature of the DUT, $\alpha_{out,src}$ is the available-power ratio between the 'src' and 'out' planes, $M_{out,src}$ is the mismatch factor at the 'rec' plane when the switch is connected to a source at the 'src' plane (e.g. hot source- 'h', cold source- 'c', DUT- 'x'), and $(\Delta T_X)_{iso}$ is an error in T_X due to an imperfect isolator. It is important to note that the derivation above from equation (3.4) ignores the $(\Delta T_X)_{iso}$ term, but treats the error resulting from ignoring this term as an uncertainty error due to imperfect isolation.

Likewise, NIST suggested the use of 50 dB of isolation (with a minimum acceptable isolation of 40 dB) to justify the use of the classic partially-corrected RSE in (3.4) and ultimately ensure a negligible uncertainty due to imperfect isolation [59]. Reference [69] also showed that increased isolation results in decreased measurement uncertainty, and that a well-isolated and corrected radiometer with 40 dB isolation would not contribute significant measurement uncertainty for standards with temperatures greater than 76K (e.g. $\pm$ 0.2K uncertainty for a 76K $\pm$ 0.6K standard). Non-isolated, uncorrected radiometer measurements are shown to be less accurate than well-isolated, corrected and uncorrected radiometer measurements in references [61, 63]. System equations for directly-connected, non-isolated, corrected radiometers, assuming (1) the mismatch from both the cold source and hot source are equal, and (2) with no assumptions, are derived in

www.manaraa.com

[70] and [71], respectively. Reference [70] highlighted the error resulting from using simplified forms of the directly-connected, non-isolated, corrected RSE.

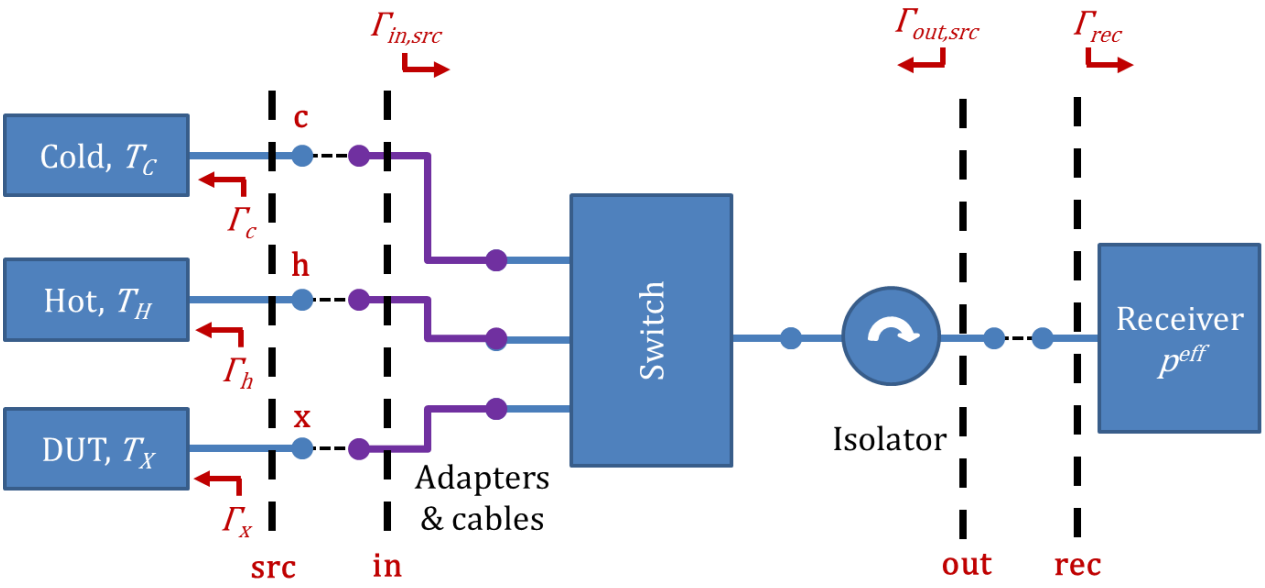

Figure 3.3 Schematic of an indirectly-connected, isolated, radiometric receiver chain including, the 'src' plane: three separate sources (hot source, DUT, and cold source), the 'in' plane: input of cable, adapter, and switch mismatches and losses for each port, the 'out' plane: output of isolator for each port, and the 'rec' plane: input to the receiver. Γ_{src} is the reflection coefficient looking into each source. $\Gamma_{in,src}$ is the reflection coefficient looking into the input of the switch port 'src'. $\Gamma_{out,src}$ is the reflection coefficient looking into the output of the isolator when the switch is connected to source 'src'. Γ_{rec} is the reflection coefficient looking into the input of the receiver.

In contrast to the corrected Y-factor based equations mentioned above that only correct for the source mismatch error, noise-parameter based RSE's [62] (herein referred to as vector-corrected RSE) offer an over-determined set of solutions (a generalized radiometer equation which contains the impedance dependent radiometer noise-parameters). Vector-corrected RSE's allow the user to correct for both source mismatch error and secondary mismatch effects (including both the receiver gain variations and changes in noise temperature due to varying source impedances [61]). While the vector-corrected RSE's correct for both source mismatch error and secondary mismatch effects it cannot be used in standalone radiometer measurements because it requires a separate tuner to achieve varying impedances. References [63, 69, 72] showed that an indirectly-connected, non-isolated, vector-corrected radiometer can have a similar accuracy to an indirectly-

www.manaraa.com

connected, well-isolated, corrected radiometer. Table 3.1 highlights the available RSEs derived in literature and the corresponding assumptions that are present for each case.

Table 3.1 Radiometer system equation (RSE) with assumptions applied

Author (Date)	Actual radiometer set-up	Type of radiometer system equation used (with assumptions applied)
Dawitt (1989) Pucic (1994) Randa (1997) Grosvenor (2000)	Indirectly-connected, well-isolated (50 dB, 60 dB)	Indirectly-connected, perfectly-isolated, corrected ($T_C = T_a$, ignores the $(\Delta T_X)_{iso}$ term)
Wait (1995)	Indirectly-connected, non-isolated to well-isolated (10 dB, 20 dB, 30 dB, 40 dB)	Indirectly-connected, non-isolated/ perfectly-isolated, corrected/ uncorrected / vector-corrected
Weatherspoon (2002, 2005)	Indirectly-connected, non-isolated	Indirectly-connected, non-isolated, vector-corrected (four traditional noise parameters are known)
Weatherspoon (2001, 2002)	Indirectly-connected, non-isolated	Indirectly-connected, perfectly-isolated, uncorrected ($T_C = T_a$, similar source mismatch where $M_{out,c} = M_{out,h} = M_{out,x}$, similar front-end path loss where $\alpha_{out,c} = \alpha_{out,h} = \alpha_{out,x}$)
Weatherspoon (2001, 2002)	Indirectly-connected, well-isolated (20 dB, 25 dB)	Directly-connected, perfectly-isolated, uncorrected ($T_C = T_a$, $M_{out,c} = M_{out,h} = M_{out,x}$, $\alpha_{out,c} = \alpha_{out,h} = \alpha_{out,x}$)
Weatherspoon (2001, 2002)	Indirectly-connected, well-isolated (20 dB, 25 dB)	Indirectly-connected, perfectly-isolated, corrected ($T_C = T_a$, ignores the $(\Delta T_X)_{iso}$ term)
Randa (2005)	Directly-connected, non-isolated	Directly-connected, non-isolated, corrected ($M_{out,c} = M_{out,h}$)
Kang (2011)	Directly-connected, non-isolated	Directly-connected, perfectly-isolated, fully-corrected (no assumptions)

3.2.2 Gap in Literature

The available radiometer system equations derived in literature either (1) have an indirectly-connected and perfectly-isolated RSEs that assumes that an ambient standard is always being used [59, 60] or (2) have a directly-connected RSEs that allow for the use of both cold and hot calibration sources [70, 71]. Reference [70] also showed the error resulting from using simplified forms of the directly-connected, non-isolated, corrected RSEs. To this point, there is no available indirectly-connected, perfectly-isolated, fully-corrected radiometer system equation that adequately accounts

www.manaraa.com

for all potential source temperatures. Nor has any study looked at the error resulting from using simplified RSEs with respect to different amounts of system isolation.

3.2.3 Contribution of Research

This work derives an indirectly-connected, perfectly-isolated, fully-corrected RSE that accounts for all available noise source combinations. Varying assumptions are applied which lead to simpler, more convenient forms of the RSE. Noise temperature is extracted for an unknown DUT using varying amounts of system isolation and applying each form of the RSE. Accuracy is accessed for each combination of the RSE with the resulting system isolation.

3.3 Radiometer System Equation Derivation with Explanation of Underlying Assumptions

Radiometer system equations are derived for both indirectly-connected and directly-connected setups, while accounting for different scenarios of similar and dissimilar front-end path-losses and source mismatches. Varying assumptions are applied which lead to simpler, more convenient forms of the system equation. Matlab's symbolic solver is used to verify the correctness of the presented sets of solved linear equations for the unknown DUT temperature.

3.3.1 Indirectly-Connected, Perfectly-Isolated, Fully-Corrected Radiometer System Equation

The block diagram from Figure 3.3 is used to describe an indirectly-connected, perfectly-isolated radiometer noise temperature measurement setup. The delivered spectral powers for this unique case at the 'rec' plane when the switch is connected to each source at the 'src' plane $P_{rec,src}^{del}$ are given by

$$\begin{aligned}
P_{rec,c}^{del} &= M_{out,c}\left[\propto_{out,c} P_c^{av} + (1-\propto_{out,c})P_a\right] + P^{eff} \\
&= k\,\Delta f \cdot M_{out,c}\left[\propto_{out,c} T_c + (1-\propto_{out,c})T_a\right] + k\,\Delta f \cdot T_{eff}\,, \\
P_{rec,h}^{del} &= M_{out,h}\left[\propto_{out,h} P_h^{av} + (1-\propto_{out,h})P_a\right] + P^{eff} \\
&= k\,\Delta f \cdot M_{out,h}\left[\propto_{out,h} T_h + (1-\propto_{out,h})T_a\right] + k\,\Delta f \cdot T_{eff}\,, \\
P_{rec,x}^{del} &= M_{out,x}\left[\propto_{out,x} P_x^{av} + (1-\propto_{out,x})P_a\right] + P^{eff} \\
&= k\,\Delta f \cdot M_{out,x}\left[\propto_{out,x} T_x + (1-\propto_{out,x})T_a\right] + k\,\Delta f \cdot T_{eff}\,,
\end{aligned} \tag{3.5}$$

where T_{src} is the noise temperature for each source at the 'src' plane, $P^{eff} = k\Delta f{\cdot}T_{eff}$ is the effective delivered spectral power at the 'rec' plane due to the perfectly-isolated receiver's intrinsic noise

www.manaraa.com

when the switch is connected to the switch port 'src', and T_{eff} is the effective input noise temperature of the receiver. Solving equation (3.5) for the unknown DUT noise temperature T_x, assuming a perfectly-isolated radiometer with dissimilar front-end path-losses and dissimilar source mismatches, the fully-corrected or general-form of the radiometer equation is

$$T_x = T_a + (T_h - T_a)\,\frac{\mathrm{M}_{out,h}\cdot\alpha_{out,h}}{\mathrm{M}_{out,x}\cdot\alpha_{out,x}}\,\frac{\mathrm{Y}_x - 1}{\mathrm{Y}_h - 1} + (T_c - T_a)\,\frac{\mathrm{M}_{out,c}\cdot\alpha_{out,c}}{\mathrm{M}_{out,x}\cdot\alpha_{out,x}}\,\frac{(\mathrm{Y}_h - \mathrm{Y}_x)}{(\mathrm{Y}_h - 1)} + \left[\frac{\mathrm{Y}_x\left(\mathrm{M}_{out,h} - \mathrm{M}_{out,c}\right) + \mathrm{Y}_h\left(\mathrm{M}_{out,c} - \mathrm{M}_{out,x}\right) - \left(\mathrm{M}_{out,h} - \mathrm{M}_{out,x}\right)}{\mathrm{M}_{out,x}\cdot\alpha_{out,x}}\right]\frac{\mathrm{T}_a}{\mathrm{Y}_h - 1}, \tag{3.6}$$

where the available-power ratio between the 'src' and 'out' planes $\alpha_{out,src}$ and the mismatch factor at the 'rec' plane when the switch is connected to a source at the 'src' plane $M_{out,src}$ are given by

$$\begin{aligned} M_{out,src} &= \frac{P_{rec,src}^{del}}{P_{src}^{av}} = \frac{(1 - |\Gamma_{rec}|^2)\left(1 - \left|\Gamma_{out,src}\right|^2\right)}{\left|1 - \Gamma_{rec}\Gamma_{out,src}\right|^2}, \\ \alpha_{out,src} &= \frac{P_{rec,src}^{av}}{P_{src}^{av}} = \frac{(1 - |\Gamma_{src}|^2)\cdot|\mathrm{S}_{21}|^2}{\left(1 - \left|\Gamma_{out,src}\right|^2\right)\cdot|1 - \mathrm{S}_{11}\Gamma_{src}|^2}. \end{aligned} \tag{3.7}$$

It is important to note that the scattering matrices $S_{sw\text{-}src}$ between the 'in' and 'out' planes (when the switch is connected to a source at the 'src' plane) is different for each switch path.

3.3.2 Indirectly-Connected, Perfectly-Isolated, Partially-Corrected Radiometer System Equation

The fully-corrected RSE in (3.6), for a perfectly-isolated radiometer with dissimilar front-end path-losses and dissimilar source mismatches, reduces to the following partially-corrected forms when several assumptions are applied. The results from applying these partial corrections are described below.

Assuming there are similar source mismatches and dissimilar path-losses (where $M_{out,c} = M_{out,h} = M_{out,x}$), the general radiometer equation in (3.6) can be reduced to

$$T_x = T_a + (T_h - T_a)\,\frac{\alpha_{out,h}}{\alpha_{out,x}}\,\frac{(\mathrm{Y}_x - 1)}{(\mathrm{Y}_h - 1)} + (T_c - T_a)\,\frac{\alpha_{out,c}}{\alpha_{out,x}}\,\frac{(\mathrm{Y}_h - \mathrm{Y}_x)}{(\mathrm{Y}_h - 1)}. \tag{3.8}$$

Assuming there are dissimilar source mismatches and similar path-losses (where $\alpha_{out,c} = \alpha_{out,h} = \alpha_{out,x}$), the general radiometer equation in (3.6) can be reduced to

www.manaraa.com

$$T_x = T_a + (T_h - T_a)\,\frac{\mathrm{M}_{out,h}}{\mathrm{M}_{out,x}}\,\frac{\mathrm{Y}_x - 1}{\mathrm{Y}_h - 1} + (T_c - T_a)\,\frac{\mathrm{M}_{out,c}}{\mathrm{M}_{out,x}}\,\frac{(\mathrm{Y}_h - \mathrm{Y}_x)}{(\mathrm{Y}_h - 1)} + \left[\frac{\mathrm{Y}_x\left(\mathrm{M}_{out,h} - \mathrm{M}_{out,c}\right) + \mathrm{Y}_h\left(\mathrm{M}_{out,c} - \mathrm{M}_{out,x}\right) - \left(\mathrm{M}_{out,h} - \mathrm{M}_{out,x}\right)}{\mathrm{M}_{out,x} \cdot \alpha_{out,x}}\right]\frac{\mathrm{T}_a}{\mathrm{Y}_h - 1}. \tag{3.9}$$

Alternatively, with similar source mismatches and similar path-losses (where $M_{out,c} = M_{out,h} = M_{out,x}$ and $\alpha_{out,c} = \alpha_{out,h} = \alpha_{out,x}$), the general radiometer equation in (3.6) can be reduced to

$$T_x = T_a + (T_h - T_a)\frac{(\mathrm{Y}_x - 1)}{(\mathrm{Y}_h - 1)} + (T_c - T_a)\frac{(\mathrm{Y}_h - \mathrm{Y}_x)}{(\mathrm{Y}_h - 1)}. \tag{3.10}$$

Assuming there are dissimilar source mismatches, dissimilar path-losses and the cold source is a termination at ambient temperature ($T_c = T_a$), the general radiometer equation in (3.6) can be reduced to

$$T_x = T_a + (T_h - T_a)\,\frac{\mathrm{M}_{out,h} \cdot \alpha_{out,h}}{\mathrm{M}_{out,x} \cdot \alpha_{out,x}}\,\frac{(\mathrm{Y}_x - 1)}{(\mathrm{Y}_h - 1)} + \left[\frac{\mathrm{Y}_x\left(\mathrm{M}_{out,h} - \mathrm{M}_{out,c}\right) + \mathrm{Y}_h\left(\mathrm{M}_{out,c} - \mathrm{M}_{out,x}\right) - \left(\mathrm{M}_{out,h} - \mathrm{M}_{out,x}\right)}{\mathrm{M}_{out,x} \cdot \alpha_{out,x}}\right]\frac{\mathrm{T}_a}{\mathrm{Y}_h - 1}, \tag{3.11}$$

The above version of the RSE is similar to the classic partially-corrected RSE shown in equation (3.4) with the exception of the omission of the second term that is treated as an uncertainty due to finite isolation. Omitting the second term in (3.11), the classic partially-corrected RSE is formed in

$$T_x = T_a + (T_h - T_a)\,\frac{\mathrm{M}_{out,h} \cdot \alpha_{out,h}}{\mathrm{M}_{out,x} \cdot \alpha_{out,x}}\,\frac{(\mathrm{Y}_x - 1)}{(\mathrm{Y}_h - 1)}\,, \tag{3.12}$$

Assuming there are similar source mismatches, dissimilar path-losses and the cold source is at ambient temperature (where $T_c = T_a$ and $M_{out,c} = M_{out,h} = M_{out,x}$), the general radiometer equation in (3.6) takes the form of

$$T_x = T_a + (T_h - T_a)\,\frac{\alpha_{out,h}}{\alpha_{out,x}}\,\frac{(\mathrm{Y}_x - 1)}{(\mathrm{Y}_h - 1)}. \tag{3.13}$$

Assuming there are dissimilar source mismatches, similar path-losses and the cold source is at ambient temperature (where $T_c = T_a$ and $\alpha_{out,c} = \alpha_{out,h} = \alpha_{out,x}$), the general radiometer equation in (3.6) can be reduced to

www.manaraa.com

$$T_x = T_a + (T_h - T_a)\,\frac{\mathrm{M}_{out,h}}{\mathrm{M}_{out,x}}\,\frac{(\mathrm{Y}_x - 1)}{(\mathrm{Y}_h - 1)} + \left[\frac{\mathrm{Y}_x(\mathrm{M}_{out,h} - \mathrm{M}_{out,c}) + \mathrm{Y}_h(\mathrm{M}_{out,c} - \mathrm{M}_{out,x}) - (\mathrm{M}_{out,h} - \mathrm{M}_{out,x})}{\mathrm{M}_{out,x} \cdot \alpha_{out,x}}\right]\frac{\mathrm{T}_a}{\mathrm{Y}_h - 1}\,. \tag{3.14}$$

Alternatively, with similar source mismatches, similar path-losses and the cold source is at ambient temperature (where $T_c = T_a$, $M_{out,c} = M_{out,h} = M_{out,x}$, and : $\alpha_{out,c} = \alpha_{out,h} = \alpha_{out,x}$), the general radiometer equation in (3.6) can be reduced to

$$T_x = T_a + (T_h - T_a)\frac{(\mathrm{Y}_x - 1)}{(\mathrm{Y}_h - 1)}. \tag{3.15}$$

3.4 Analysis and Validation of Radiometer System Equations through Simulations

The derived radiometer system equations from Section 3.3 are analyzed and validated with an EM circuit simulation. An RF System Budget Analysis in Keysight Advanced Design System (ADS) is used to model an ideal radiometer receiver chain at 1.4 GHz. The delivered power to the receiver from each source is calculated by the ADS simulation and each calculated power is input into the respective RSE. The noise resolution bandwidth is 1Hz. The schematic for the receiver chain is shown in Figure 3.4. The chain consists of multiple measurement planes which begin with the output of three reference sources and end with the connection to the radiometer. Plane 1 is defined as the output of three distinct sources connected to the radiometer (*i.e.* hot source, device under test (DUT), and cold source). Plane M represents the respective impedance mismatches for these sources. Plane 'C' consists of the input and output path for the cables, adapters, and switch paths following each source. Each cable/switch path has a unique set of scattering parameters. Plane I includes the input and output ports for the isolator immediately before the receiver. Plane 2 is defined as the input to the first pre-amplifier of the receiver.

The ideal radiometer includes the path from planes 1:2, where the sources are connected directly to the receiver. A realistic directly-connected scenario can either include (1a) the non-isolated radiometer path from planes 1:M:2, where the sources experience an impedance mismatch and are connected directly to the receiver, or (1b) the isolated radiometer path from planes 1:M:I:2,

www.manaraa.com

where the sources experience a mismatch and are connected to an isolator and the receiver. A realistic indirectly-connected scenario can either include (2a) the non-isolated radiometer path from planes 1:M:C:2, where the sources experience an impedance mismatch and are connected to the cables in cascade with adapters, the switch, and the receiver, or (2b) the isolated radiometer path from planes 1:M:C:I:2, where the sources experience a mismatch and are connected to the cables in cascade with adapters, the switch, an isolator, and the receiver.

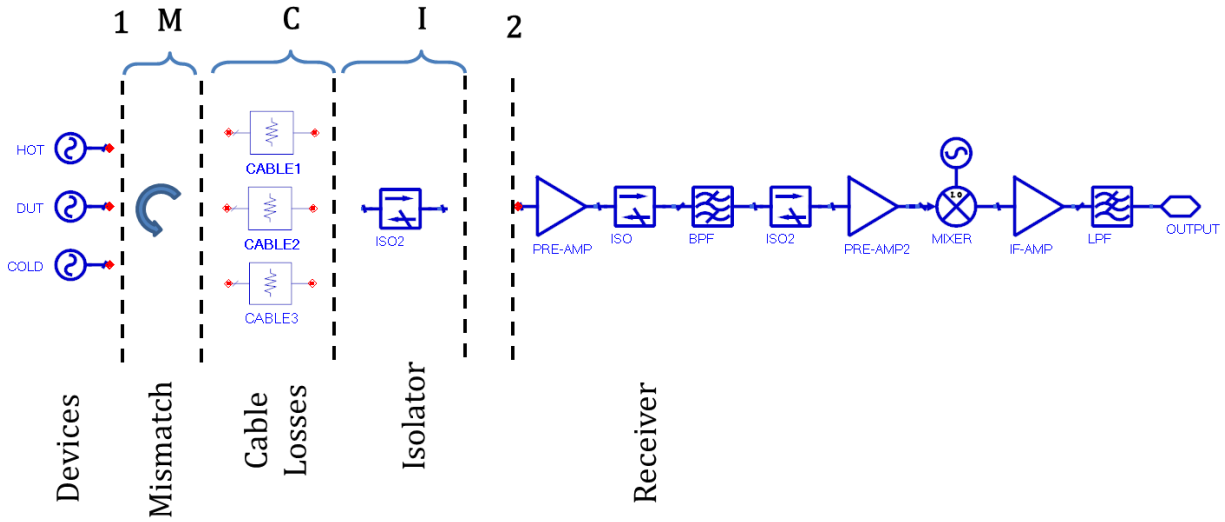

Figure 3.4 Schematic of ideal radiometer receiver chain including Plane 1: three separate loads (hot load, DUT, and cold load), Plane M: impedance mismatch for respective loads, Plane C: cable, adapter, and switch mismatches and losses, Plane I: isolator mismatch and loss, and Plane 2: input of receiver pre-amplifier.

Take for example that the noise temperatures for the cold source T_C, the hot source T_H, and the DUT T_X are equal to ambient temperature T_a (290K), 300·T_a, and 150·T_a respectively. Electrical device characteristics at 1.4 GHz (scattering parameters, gain/loss, isolation, effective noise temperature, etc.) are described in Table 3.2, Table 3.3, Table 3.4, and Table 3.5 for the sources, cable/switch paths, isolators, and the receiver, respectively. In general, all devices are well-matched to a 50-ohm system. The predicted unknown DUT temperature T_X using select forms of the radiometer system equation are described below. Figure 3.5 shows the predicted unknown DUT temperature T_X using the sources found in Table 3.2. Source combinations of either T_a and T_H or T_C

www.manaraa.com

and T_H are used in conjunction with RSEs (3.15) and (3.10). Using the correct RSE with the intended source temperature (*e.g.* $T_a \rightarrow$ (3.15) and $T_C \rightarrow$ (3.10)) gives very comparable results to the ideal simulation. However, if the cold source T_C is used with the RSE (3.15) then more error is introduced in comparison to using the intended RSE (3.10). This comparison is meant to highlight the need for a more generic RSE when a cold and hot source combination is used. The ambient temperature dependent RSE (3.15) is a variation of the generic cold temperature dependent RSE (3.10). For any given value of isolation, the directly-connected radiometer predicts a more accurate answer than the RSEs that do not include mismatch data. The same relationship holds for the indirectly-connected radiometer setup (*i.e.* that RSEs with no mismatch data provide better predictions than the RSEs which include mismatch data). Figure 3.6 shows the predicted unknown DUT temperature T_X using source combinations of either T_a and T_H or T_C and T_H in conjunction with RSEs (3.15), (3.13), (3.12), (3.11), (3.10), (3.8), and (3.6). The predicted temperatures using RSEs (3.15) and (3.10) (*i.e.* no mismatch and path-loss included) give the best answer for each respective cold source calibration. This is believed to be the case due to the original assumption of the derivation being for a perfectly-isolated radiometer. The full list of predicted unknown DUT temperatures resulting from each arrangement of calibration source combination and corresponding delivered powers can be found in Table 3.6 and Table 3.7.

Table 3.2 Ideal receiver chain electrical characteristics of the sources at the Plane 1

Device	**Temperature**	**Scattering parameters at 1.4 GHz (dB / degree)**			
		S_{11}	**S_{21}**	**S_{12}**	**S_{22}**
Hot source	$T_H = 300 \cdot T_a$	-11 / 0			
Cold source	$T_C = 0.15 \cdot T_a$	-12 / 0			
Ambient source	$T_C = T_a$	-12 / 0			
DUT	$T_X = 150 \cdot T_a$	-10 / 0			

www.manaraa.com

Table 3.3 Ideal receiver chain electrical characteristics of the cables and switch paths at the Plane C

Device	Temperature	Scattering parameters at 1.4 GHz (dB / degree)			
		S_{11}	S_{21}	S_{12}	S_{22}
Cables/switch (Hot path)	T_a	-12 / 0	-1.6 / 0	-1.6 / 0	-12 / 0
Cables/switch (Cold path)	T_a	-11 / 0	-1.8/ 0	-1.8 / 0	-11 / 0
Cables/switch (Ambient path)	T_a	-11 / 0	-1.8/ 0	-1.8 / 0	-11 / 0
Cables/switch (DUT path)	T_a	-10 / 0	-2 / 0	-2 / 0	-10 / 0

Table 3.4 Ideal receiver chain electrical characteristics of the isolators at the Plane I

Device	Temperature	Scattering parameters at 1.4 GHz (dB / degree)			
		S_{11}	S_{21}	S_{12}	S_{22}
Isolator 10 dB	T_a	-15 / 0	-0.1 / 0	-10 / 0	-15 / 0
Isolator 20 dB	T_a	-15 / 0	-0.2 / 0	-20 / 0	-15 / 0
Isolator 40 dB	T_a	-15 / 0	-0.4/ 0	-40 / 0	-15 / 0
Isolator 60 dB	T_a	-15 / 0	-0.6/ 0	-60 / 0	-15 / 0

Table 3.5 Ideal receiver chain electrical characteristics of the receiver at the Plane 2

Device	Temperature	Scattering parameters at 1.4 GHz (dB / degree)			
		S_{11}	S_{21}	S_{12}	S_{22}
Receiver	$T_{eff}=0.15 \cdot T_a$	-20 / 0	100 / 0		

www.manaraa.com

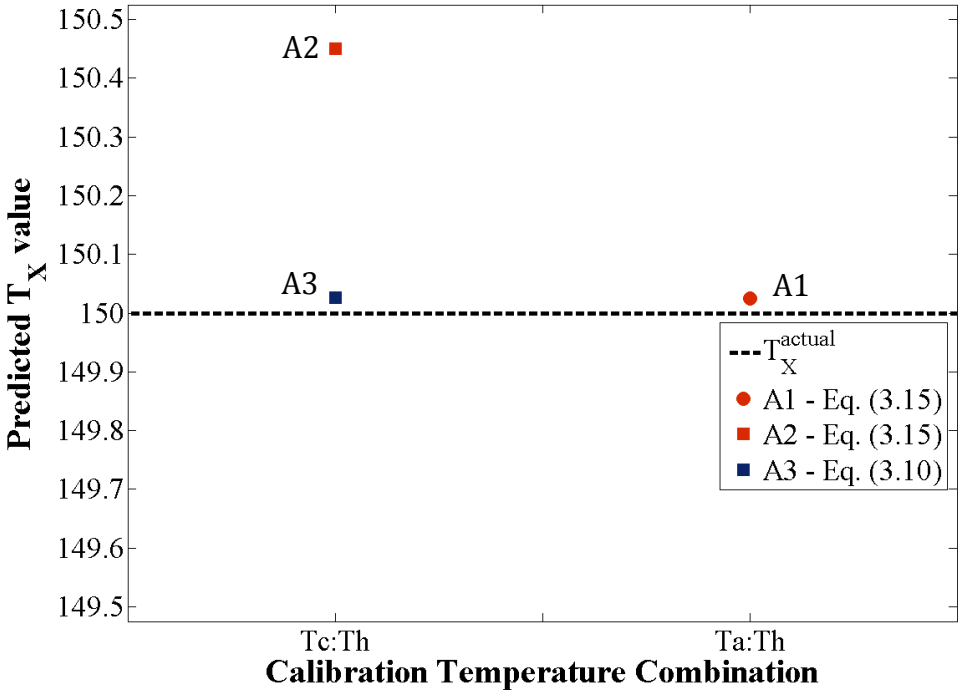

Figure 3.5 Predicted unknown DUT noise temperature for a directly-connected radiometer setup using source combinations of either T_a and T_H or T_C and T_H. Noise temperatures are calculated with RSEs (3.15) and (3.10). Using the correct RSE with the intended source temperature (*e.g.* $T_a \rightarrow$ (3.15) and $T_C \rightarrow$ (3.10)) gives very comparable results to the ideal simulation, but using the RSE intended for the ambient source with a cold source introduces more error.

www.manaraa.com

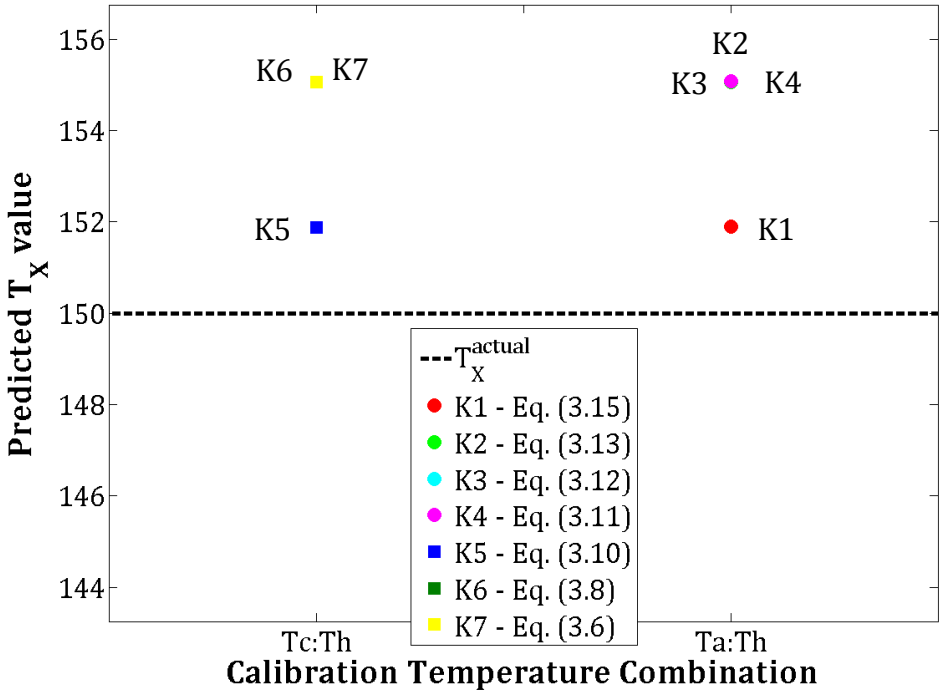

Figure 3.6 Predicted unknown DUT noise temperature for an indirectly-connected radiometer setup using source combinations of either T_a and T_H or T_C and T_H. Noise temperatures are calculated with RSEs (3.15), (3.13), (3.12), (3.11), (3.10), (3.8), and (3.6). Best unknown DUT noise temperature predictions come from equations without mismatch included in formulation (*i.e.* RSEs (3.15) and (3.10)).

www.manaraa.com

Table 3.6 Predicted DUT noise temperature T_X using multiple forms of the directly-connected RSE

Path	RSE #	Description of Radiometer System Equation (RSE) Used	Delivered powers (dBm)			Predicted $T_X = [?] \cdot T_a$
			P_H	P_C	P_X	
1:2	(3.15)	Directly-connected, perfectly-isolated, uncorrected RSE, $T_C = T_a$, similar source mismatches, similar path-losses	-61.267	P_a -73.188	-64.019	**A1** 150.025
				P_C -73.372		**A2** 150.451
	(3.10)	Directly-connected, perfectly-isolated, uncorrected RSE, $T_C = T_C$, similar source mismatches, similar path-losses		P_C -73.372		**A3** 150.026
1:M:2	(3.15)	Directly-connected, perfectly-isolated, uncorrected RSE, $T_C = T_a$	-61.019	P_a -72.987	-63.743	**B1** 151.232
				P_C -73.171		**B2** 151.649
	(3.14)	Directly-connected, perfectly-isolated, partially-corrected RSE, $T_C = T_a$, dissimilar source mismatches, similar path-losses		P_a -72.987		**B3** 153.600
				P_C -73.171		**B4** 154.025
	(3.10)	Directly-connected, perfectly-isolated, uncorrected RSE, $T_C = T_C$		P_C -73.171		**B5** 151.228
	(3.9)	Directly-connected, perfectly-isolated, partially-corrected RSE, $T_C = T_G$, dissimilar source mismatches, similar path-losses		P_C -73.171		**B6** 153.591
1:M: I_{10dB}:2	(3.15)	Directly-connected, perfectly-isolated, uncorrected RSE, $T_C = T_a$	-60.686	P_a -72.728	-63.377	**C1** 152.701
				P_C -72.915		**C2** 151.063
	(3.14)	Directly-connected, perfectly-isolated, partially-corrected RSE, $T_C = T_a$		P_a -72.728		**C3** 153.425
				P_C -72.915		**C4** 151.778
	(3.10)	Directly-connected, perfectly-isolated, uncorrected RSE, $T_C = T_C$		P_C -72.915		**C5** 150.639
	(3.9)	Directly-connected, perfectly-isolated, partially-corrected RSE, $T_C = T_C$		P_C -72.915		**C6** 151.351
1:M: I_{20dB}:2	(3.15)	Directly-connected, perfectly-isolated, uncorrected RSE, $T_C = T_a$	-60.840	P_a -72.849	-63.533	**D1** 152.547
				P_C -73.034		**D2** 152.959
	(3.14)	Directly-connected, perfectly-isolated, partially-corrected RSE, $T_C = T_a$		P_a -72.849		**D3** 152.680
				P_C -73.034		**D4** 153.093
	(3.10)	Directly-connected, perfectly-isolated, uncorrected RSE, $T_C = T_C$		P_C -73.034		**D5** 152.541
	(3.9)	Directly-connected, perfectly-isolated, partially-corrected RSE, $T_C = T_C$		P_C -73.034		**D6** 152.674

www.manaraa.com

Table 3.6 (Continued)

Path	RSE #	Radiometer System Equation Used	Delivered powers (dBm)			Predicted
			P_H	P_C	P_X	$T_X = [?] \cdot T_a$
1:M: I_{40dB}:2	(3.15)	Directly-connected, perfectly-isolated, uncorrected RSE, $T_C = T_a$	-61.054	P_a -72.934	-63.742	**E1** 152.446
				P_C -73.114		**E2** 152.860
	(3.14)	Directly-connected, perfectly-isolated, partially-corrected RSE, $T_C = T_a$		P_a -72.934		**E3** 152.455
				P_C -73.114		**E4** 152.870
	(3.10)	Directly-connected, perfectly-isolated, uncorrected RSE, $T_C = T_C$		P_C -73.114		**E5** 152.442
	(3.9)	Directly-connected, perfectly-isolated, partially-corrected RSE, $T_C = T_C$		P_C -73.114		**E6** 152.452
1:M: I_{60dB}:2	(3.15)	Directly-connected, perfectly-isolated, uncorrected RSE, $T_C = T_a$	-61.244	P_a -72.943	-63.920	**F1** 152.487
				P_C -73.115		**F2** 152.901
	(3.14)	Directly-connected, perfectly-isolated, partially-corrected RSE, $T_C = T_a$		P_a -72.943		**F3** 152.488
				P_C -73.115		**F4** 152.902
	(3.10)	Directly-connected, perfectly-isolated, uncorrected RSE, $T_C = T_C$		P_C -73.115		**F5** 152.483
	(3.9)	Directly-connected, perfectly-isolated, partially-corrected RSE, $T_C = T_C$		P_C -73.115		**F6** 152.484

Table 3.7 Predicted DUT noise temperature T_X using multiple forms of the indirectly-connected RSE

Path	RSE #	Radiometer System Equation Used	Delivered powers (dBm)			Predicted
			P_H	P_C	P_X	$T_X = [?] \cdot T_a$
1:M:C:2	(3.15)	Indirectly-connected, perfectly-isolated, uncorrected RSE, $T_C = T_a$	-61.789	P_a -73.369	-64.560	**G1** 148.435
	(3.13)	Indirectly-connected, perfectly-isolated, partially-corrected RSE, $T_C = T_a$				**G2** 140.990
	(3.12)	Indirectly-connected, perfectly-isolated, partially-corrected (classic) RSE, $T_C = T_a$				**G3** 153.631
	(3.11)	Indirectly-connected, perfectly-isolated, partially-corrected RSE, $T_C = T_a$				**G4** 153.723
	(3.10)	Indirectly-connected, perfectly-isolated, uncorrected RSE, $T_C = T_C$		P_C -73.529		**G5** 148.413
	(3.8)	Indirectly-connected, perfectly-isolated, partially-corrected RSE, $T_C = T_C$				**G6** 140.982
	(3.6)	Indirectly-connected, perfectly-isolated, partially-corrected RSE, $T_C = T_C$				**G7** 153.714

www.manaraa.com

Table 3.7 (Continued)

Path	RSE #	Radiometer System Equation Used	Delivered powers (dBm)			Predicted
			P_H	P_C	P_X	$T_X = [?] \cdot T_a$
1:M:C: I_{10dB}:2	(3.15)	Indirectly-connected, perfectly-isolated, uncorrected RSE, $T_C = T_a$	-61.267	P_a -72.938	-63.961	**H1** 151.701
	(3.13)	Indirectly-connected, perfectly-isolated, partially-corrected RSE, $T_C = T_a$				**H2** 151.365
	(3.12)	Indirectly-connected, perfectly-isolated, partially-corrected (classic) RSE, $T_C = T_a$				**H3** 153.950
	(3.11)	Indirectly-connected, perfectly-isolated, partially-corrected RSE, $T_C = T_a$				**H4** 153.968
	(3.10)	Indirectly-connected, perfectly-isolated, uncorrected RSE, $T_C = T_C$		P_C -73.102		**H5** 151.681
	(3.8)	Indirectly-connected, perfectly-isolated, partially-corrected RSE, $T_C = T_C$				**H6** 151.357
	(3.6)	Indirectly-connected, perfectly-isolated, partially-corrected RSE, $T_C = T_C$				**H7** 153.960
1:M:C: I_{20dB}:2	(3.15)	Indirectly-connected, perfectly-isolated, uncorrected RSE, $T_C = T_a$	-61.442	P_a -72.827	-64.108	**I1** 152.082
	(3.13)	Indirectly-connected, perfectly-isolated, partially-corrected RSE, $T_C = T_a$				**I2** 154.578
	(3.12)	Indirectly-connected, perfectly-isolated, partially-corrected (classic) RSE, $T_C = T_a$				**I3** 154.974
	(3.11)	Indirectly-connected, perfectly-isolated, partially-corrected RSE, $T_C = T_a$				**I4** 154.977
	(3.10)	Indirectly-connected, perfectly-isolated, uncorrected RSE, $T_C = T_C$		P_C -72.979		**I5** 152.060
	(3.8)	Indirectly-connected, perfectly-isolated, partially-corrected RSE, $T_C = T_C$				**I6** 154.568
	(3.6)	Indirectly-connected, perfectly-isolated, partially-corrected RSE, $T_C = T_C$				**I7** 154.967
1:M:C: I_{40dB}:2	(3.15)	Indirectly-connected, perfectly-isolated, uncorrected RSE, $T_C = T_a$	-61.668	P_a -72.891	-64.328	**J1** 151.882
	(3.13)	Indirectly-connected, perfectly-isolated, partially-corrected RSE, $T_C = T_a$				**J2** 155.003
	(3.12)	Indirectly-connected, perfectly-isolated, partially-corrected (classic) RSE, $T_C = T_a$				**J3** 155.027
	(3.11)	Indirectly-connected, perfectly-isolated, partially-corrected RSE, $T_C = T_a$				**J4** 155.027
	(3.10)	Indirectly-connected, perfectly-isolated, uncorrected RSE, $T_C = T_C$		P_C -73.037		**J5** 151.860
	(3.8)	Indirectly-connected, perfectly-isolated, partially-corrected RSE, $T_C = T_C$				**J6** 154.994
	(3.6)	Indirectly-connected, perfectly-isolated, partially-corrected RSE, $T_C = T_C$				**J7** 155.018

www.manaraa.com

Table 3.7 (Continued)

Path	RSE #	Radiometer System Equation Used	Delivered powers (dBm)			Predicted $T_X = [?] \cdot T_a$
			P_H	P_C	P_X	
1:M:C: I_{60dB}:2	(3.15)	Indirectly-connected, perfectly-isolated, uncorrected RSE, $T_C = T_a$	-61.857	P_a -72.901	-64.504	**K1** 151.899
	(3.13)	Indirectly-connected, perfectly-isolated, partially-corrected RSE, $T_C = T_a$				**K2** 155.067
	(3.12)	Indirectly-connected, perfectly-isolated, partially-corrected (classic) RSE, $T_C = T_a$				**K3** 155.070
	(3.11)	Indirectly-connected, perfectly-isolated, partially-corrected RSE, $T_C = T_a$				**K4** 155.070
	(3.10)	Indirectly-connected, perfectly-isolated, uncorrected RSE, $T_C = T_C$		P_C -73.041		**K5** 151.879
	(3.8)	Indirectly-connected, perfectly-isolated, partially-corrected RSE, $T_C = T_C$				**K6** 155.059
	(3.6)	Indirectly-connected, perfectly-isolated, partially-corrected RSE, $T_C = T_C$				**K7** 155.061

3.5 Conclusion

A generic isolated radiometer system equation is derived for all possible calibration source combinations. This derivation overcomes a gap in previous literature where, until now, no generic, anatomically accurate, radiometer system equation was available for a source combination utilizing both a cold (temperature lower than ambient) and hot (temperature greater than ambient) reference source. The generic isolated radiometer system equation predicts comparable results to that of an ideal simulation. While improved isolation decreases measurement uncertainty, it does not improve the accuracy of estimated noise temperatures using a perfectly-isolated radiometer system equation assumption. In order to test this assertion, an imperfectly-isolated radiometer system equation should be derived and compared to the results above.

www.manaraa.com

Chapter 4 Biological Tissue Phantoms

4.1 Introduction

This dissertation validates a comprehensive closed-form analytical radiometric model by performing radiometric measurements on an anatomically accurate artificial human body testbed. This chapter highlights the development of this anatomically accurate artificial human body testbed. Human tissue-mimicking biological phantoms (bio-phantoms) allow users to design and test bio-sensors in a controlled environment without the need for an actual human body to be present. Bio-phantoms are artificially created materials that mimic the electrical and mechanical properties of realistic human tissues. In regards to radiometric sensing, an effective testbed validation scenario consists of a well-controlled temperature source in contact with other layered materials that isolate the bio-sensor from the source. This isolated temperature source setup provides an ideal validation apparatus which can help to determine the microwave thermometer's ability to accurately predict subsurface temperature, provided that the temperature of the embedded source is precisely known. Bio-phantoms can come in liquid, semi-liquid, semi-solid, or solid states. Previous microwave thermometer testbeds have employed the use of either exclusively liquid phantom testbeds [12, 44] or hybrid phantom (a combination liquid and solid) testbeds [13, 73].

This chapter highlights the development of a layered hybrid bio-phantom (consisting of a solid skin phantom, a solid fat phantom, and a liquid muscle phantom). Section 4.2 reviews relevant bio-phantom literature. Section 4.3 covers the methods used during the phantom development. Section 4.4 highlights the results from the phantom development. This chapter concludes with Section 4.5.

www.manaraa.com

4.2 Review of Relevant Biological Tissue Phantom Literature

4.2.1 Background

Bio-phantoms are generally classified into liquid, semi-liquid, semi-solid, and solid states [74]. The distinction among a semi-liquid and a semi-solid state is that the semi-liquid is a material of a gel-like form and is more solid than a liquid but cannot hold its shape without an outside container, whereas the semi-solid is a material of a jelly-like form that is able to mold to any shape independently. A number of bio-phantom recipes are reviewed in Table 4.1 with respect to the recipe's applicability to facilitate biomedical radiometric sensing. The reader is referred to [74-76] for exhaustive reviews on currently available literature for bio-phantom development.

Table 4.1 Overview of available bio-phantoms and the applicability to enable radiometric sensing

Work	Main Ingredient	Phantom Type	State	Applicability for Radiometric Sensing
[77]	Water, TX151, polyethylene powder	Muscle, brain, skin	Wet solid	· Dries out · bacteria prone · breaks if you flex too much
[78]	Water, gelatin, detergent	Skin, fat, blood, muscle	Gel	· Has to be stored in an outside container · hard to control thickness
[79]	Water, cooking oil, detergent, TX151, agar	Fat	Gel	· Falls apart · wet · hard to control thickness
[80]	Water, sugar, HEC	Muscle	Liquid	· Good properties for a liquid phantom over a narrow band
[13, 73]	Water, TX151	Skin-muscle hybrid	Solid	· Dries out · hard to control thickness
[81]	Silicon rubber, carbon powder	Skin, fat, bone, muscle	Solid	· Can flex · solid · thickness easily controlled with certain recipes · dry
[82-84]	Urethane rubber, graphite powder	Skin, fat	Solid	· Can flex · solid · thickness easily controlled with certain recipes · dry · need to use a mechanical press to flatten mixtures with higher powder concentrations · granular surface

www.manaraa.com

4.2.2 Gap in Literature

The availability of hybrid bio-phantom testbeds to validate radiometric thermometer systems is limited [13, 73]. Specifically, currently available skin bio-phantom recipes do not provide adequate processes to realize highly reproducible solid state phantoms that provide consistent mechanical and electrical properties. Previous solid state skin phantoms either (1) do not provide adequate details to recreate the phantom recipe [81, 85], (2) require specialized equipment to realize the phantom recipe [86], or (3) have inconsistencies between the phantom recipe and the actual mixing processes which lead to significant variations between the predicted and realized dielectric properties or require extremely invasive mixing techniques (*e.g.* the user is required to knead the messy phantom material by hand) [82-84].

4.2.3 Contribution of Research

The dissertation contributes to the body of knowledge by providing a novel recipe for a solid state skin tissue mimicking phantom that accurately mimics the electrical properties of actual dry human skin versus frequency up to 18 GHz. The developed solid state skin phantom begins in pourable liquid form and then cures at room temperature into a dry solid state mold. Pourable solid state skin phantoms make realizing any desired thickness much easier as compared to previous recipes which require kneading by hand.

4.3 Methodology

Methods for the development of the skin, fat, and muscle bio-phantoms are presented. The muscle tissue-mimicking phantom is developed from a mixture of water, sugar, salt, hydroxethylcellulose (HEC), and bactericide. The presented recipe is adapted from methods originally used in [73, 80]. A similar recipe is ultimately employed, but weight proportions are chosen to give the proper EM response in the desired frequency range. The water is heated then the sugar, salt, and bactericide are added and are allowed to dissolve. Next, HEC is added and the mixture is stirred until dissolved.

www.manaraa.com

The skin and fat tissue-mimicking phantoms are created from a combination of urethane rubber, graphite powder, and liquid solvents (acetone and amyl acetate, respectively). The presented recipes are adapted from methods originally used in [82-84]. Table 4.2 highlights the specific materials used during the solid phantom development. Urethane rubber was chosen as the matrix material because it could be developed with standard lab equipment and it would allow for curing at room temperature [82, 83]. Graphite powder is selected because it is shown to adequately provide permittivity values within the range of human body tissues when used in conjunction with a rubber matrix [82-84]. Urethane-graphite mixtures are cited to have a viscosity-based maximum mixing limit [82] so the liquid solvents are introduced to allow for the addition of more graphite (more graphite leads to higher permittivity values from cured mixtures).

Table 4.2 Materials used for skin and fat tissue-phantom development

Material	Type	Particle Size	Supplier
Urethane Rubber	Vytaflex 20	-----	Smooth-On
Graphite powder	Synthetic (7782-42-5)	7-11 μm	Alfa-Aesar
Solvent	Acetone	-----	Rust-Oleum
	Amyl Acetate (628-63-7)	-----	ConsolidatedChemical

All materials are weighed for proper ratio and are mixed by hand with wooden sticks in either paper or polyethylene cups. The choice of cup should be carefully chosen due to the possibility of the solvent reacting with certain plastic-based cups. Polypropylene reacts with both solvents and is not a good choice for the mixing cup. Mixture homogeneity is assessed by both visual inspection and the perceived resistance to flow by the mixing stick (i.e. for homogenous mixtures the resistance to flow would be minimal). Any mixtures that either appeared inhomogeneous or exhibited a high resistance to flow are kneaded by hand. The addition of the solvent removes the need for kneading by hand. Typically, the high graphite content samples that are prepared without using a solvent are more likely to require kneading by hand. The time required to mix a single sample is completed well before one-fourth of the total published pot life (the amount of time it takes for the initial mixed viscosity value to double). Mixtures are poured

www.manaraa.com

into a mold and are allowed to cure over 24 hours. Agilent's open-ended coaxial probe is used to measure dielectric properties for all phantoms over a frequency range of 0.1 GHz to 18 GHz. An average value is calculated from five recorded dielectric measurements.

4.4 Skin, Fat, and Muscle Tissue-Mimicking Bio-Phantoms

4.4.1 Bio-Phantom Recipes

Phantom recipes designed to mimic dry human skin, fat, and muscle tissue are introduced. Table 4.3 highlights all phantom recipes. The skin phantom is composed of urethane → 55% of the total graphite/urethane weight, graphite → 45% of the total graphite/urethane weight, and acetone → 42% of the graphite weight. The fat phantom is made up of urethane → 92% of the total graphite/urethane weight, graphite → 8% of the total graphite/urethane weight, and amyl acetate → 10% of the total graphite/urethane weight. The muscle phantom is comprised of water → 57% of the total weight, sugar → 41% of the total weight, salt → 0.35 % of the total weight, HEC → 0.1% of the total weight, and bactericide → 0.27% of the total weight.

Table 4.3 Recipes for hybrid tissue-phantom

Material	Skin (weight %)	Fat (weight %)	Muscle (weight %)
Urethane rubber	55%	92%	-----
Graphite powder	45%	8%	-----
Acetone	42% of graphite weight	-----	-----
Amyl Acetate	-----	10% of total graphite/urethane weight	-----
Water	-----	-----	57%
Sugar	-----	-----	41%
Salt	-----	-----	0.35%
Hydroxethylcellulose (HEC)	-----	-----	0.1%
Bactericide (Borax)	-----	-----	0.27%

4.4.2 Bio-Phantom Electrical Properties

The dielectric properties of the hybrid phantoms are presented. Figure 4.1 compares the dielectric constant and the loss-tangent for the developed skin, fat, and muscle phantoms to the industry standard Gabriel measured dielectric properties [33-36]. The liquid muscle phantom

www.manaraa.com

predicts the industry standard values very closely from 0.5 to 2.5 GHz. This feature of a well-matched dielectric constant over a relatively small bandwidth is expected for liquid state tissue phantoms. The fat phantom mimics the dielectric constant extremely close over the full 18 GHz measurement bandwidth. The skin phantom also mimics the dielectric constant closely over the bandwidth, with the exception of lower frequencies. The dispersive nature of the graphite powder has to be further accommodated for at lower frequencies (*i.e.* a different urethane/graphite mixture to decrease phantom permittivity values at lower frequencies). It is also important to note that the loss-tangent for the skin phantom is decreasing as frequency increases. This EM response may be caused by the graphite powder that is closer to the top surface possibly settling and ultimately not forming a dense matrix of graphite and urethane. This EM response is highly favorable for other applications which may need higher dielectric constants and lower loss-tangents at higher frequencies (*e.g.* antenna and electronic circuit designs).

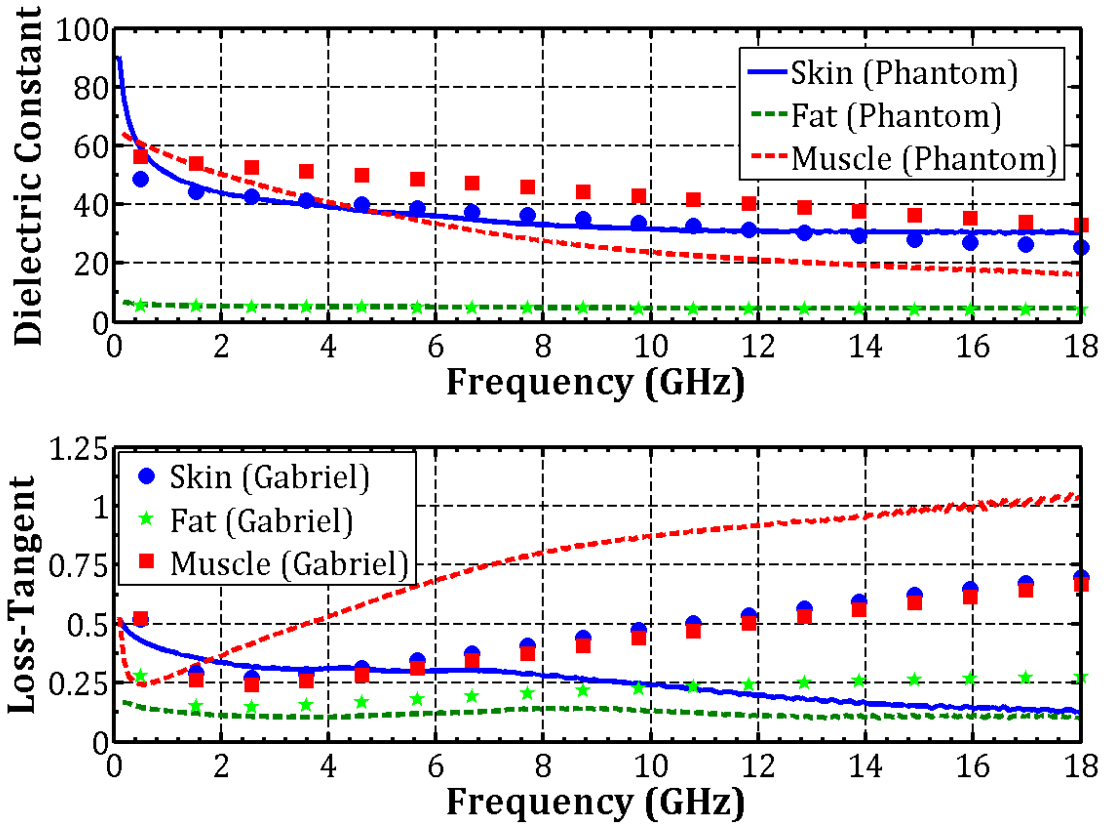

Figure 4.1 Dielectric constants and loss-tangents of human tissue-mimicking phantoms compared to the industry standard Gabriel measured values.

www.manaraa.com

4.4.3 Bio-Phantom Mechanical Properties

The relevant mechanical properties of the developed skin bio-phantom are presented and are compared against the mechanical properties of older phantom recipes. Figure 4.2 compares the finished surfaces from the newly developed skin bio-phantom to the skin bio-phantom developed in [82, 83] (*i.e.* composed of urethane → 63%, graphite → 30%, and carbon black → 7%). The surface finish from the new sample is smoother and has fewer cracks than the old recipe. This surface finish difference is due to the new recipe being a pourable mixture as opposed to the old recipe requiring the use of hand kneading and has to be pressed against a plane in order to form a flat surface.

Figure 4.2 Comparison of cured samples from old recipe sample [82, 83] (left) to new recipe sample (right). Surface finish of the new sample is finer and has fewer cracks than the old recipe.

4.5 Conclusion

An electrically accurate skin and fat bio-phantom design are presented. The addition of solvents to a urethane and graphite based solid state tissue phantom recipe helps to control the bio-phantom permittivity and allows for improved physical properties. However, the addition of solvents also increases the formation of air bubbles. Degassing is needed to remove the air bubbles more quickly and the use of an oven allows for faster curing times.

www.manaraa.com

Chapter 5 Design of On-Body Inward Facing Antennas

5.1 Introduction

Microwave (MW) radiometric sensing is a means to realize portable, non-invasive, wireless thermometry in order to detect internal body temperatures [12, 13]. The antennas used in MW radiometry have special considerations in that they must meet high beam efficiency, low ohmic loss, narrow beam solid angle, and high input matching requirements [28, 87]. In [88], the antenna is regarded as one of the most critical components limiting radiometer system performance as being viable for both treatment and detection in the biomedical realm.

Human body antenna designs should explicitly show that all requirements for successful sensing have been met. Many antenna designs for human body sensing exhibit adequate in-band return loss (≥10dB) [12, 13, 15-27], but the radiation characteristics are not always presented. Significant shortcomings in the antenna pattern can be masked if the radiation pattern is not provided. Particularly, the antenna should radiate in the broadside direction toward the body and should not be sensitive to the ambient environment nor other areas outside of the body. The microstrip antenna is a popular category of antenna to use during human body sensing due to its compact size, planar structure, and ability to be made conformal. Also, it is well documented that unwanted and augmented side lobes occur when surface waves reach the edge of a finite ground plane and radiate into the propagation medium [89]. This surface wave propagation negatively affects both the efficiency and radiation pattern of microstrip antennas [89] and must be mitigated in order to accurately sense while the antenna is on-body.

This chapter presents a design process for inward facing spiral antennas used for on-body sensing. A novel implementation of an in-plane, continuous, quasi-corrugated, cylindrically-

www.manaraa.com

symmetric, electromagnetic bandgap (EBG) structure is used to mitigate unwanted side lobes that arise from on-body inward facing antennas. The effectiveness of the approach is highlighted by comparing both the simulated and measured radiation characteristics of an on-body spiral antenna with and without the EBG structure. Experimental measurements show an improvement in the broadside gain, side gain, and rear gain of +3.84 dB, -2.64 dB, and -8dB, respectively from the EBG antenna over the convention antenna. Likewise, simulations show an improvement in the broadside gain, side gain, and rear gain of +0dB, -7dB, and -7dB, respectively. Main beam efficiency is improved from 45.33% and 54.43% for the conventional antenna to 87.59% and 86.36% for the EBG antenna for simulated and measured beam efficiencies, respectively.

This chapter highlights the result of the inclusion of an in-plane electromagnetic bandgap structure within an on-body inward facing spiral antenna design and demonstrates an improvement in the antenna radiation characteristics. Section 5.2 overviews the available antennas for human body sensing with a particular focus on on-body sensing. Section 5.3 discusses the design of spiral antennas for contact sensing and highlights the problems that arise within the radiation pattern for this sensing scenario. Section 5.4 investigates the effect that a tuned electromagnetic bandgap surface plays on improving radiation characteristics. This work concludes with Section 5.5.

5.2 Overview of Human Body Sensing Antennas

Various antenna types (*e.g.* spiral, patch, waveguide, monopole, slot, elliptical) have been used for human body radiometric sensing. Typically these antennas fall within configurations of either on-body or off-body within the near-field. Table 5.1 highlights the types of human sensing antennas used, the applied antenna configuration, and the inclusion or exclusion of the antenna radiation pattern within each work. Most of the works do not include the antenna radiation pattern, but only specific absorption rate (SAR) information.

www.manaraa.com

Table 5.1 Review of inward facing human body sensing antennas

Work	Antenna Type	Configuration (On-Body or Off-Body)	Inclusion of radiation pattern
[12]	Dipole and spiral	On-body (water phantom)	-----
[15]	Dual concentric conductor, logarithmic spiral, Archimedean spiral, dielectric-filled rectangular waveguide	On-body (water-bath)	-----
[13, 16]	Cavity-backed slot	Off-body (hybrid phantom)	Far-field radiation pattern
[17]	L-shaped monopole	On-body (water)	-----
[18, 19]	Dielectric-filled rectangular waveguide	On-body (water-bath)	Power loss density (PLD)
[20]	Circular-slot	On-body (water-bolus)	Specific absorption rate (SAR)
[21]	Elliptical antenna	On-body (human hand, chest, hip, belly)	-----
[22]	Loop-less antenna	Embedded (gel phantom)	-----
[23-25]	Logarithmic spiral	On-body (head/urine phantom)	PLD, SAR
[26]	Slot with dual concentric square patch	On-body (multilayered liquid phantom)	SAR
[27]	Co-planar grounded ring antenna	On-body	SAR

5.2.1 Gap in Literature

Designing antennas for human body contact sensing imposes a number of restrictions that are unique to this specific case. In this scenario, antenna input match along with radiation and beam efficiencies must be precisely known and maximized. Few works exist in literature that explicitly outlines how to design antennas for on-body inward facing applications [12, 13, 15-27]. Of the available on-body antenna designs most provide SAR patterns, but do not include antenna radiation patterns for the scenario when the antenna is in contact with the body [12, 15, 17-27]. Most of these works also do not discuss the proper way to mitigate unwanted side lobes that become apparent during an on-body or near-field sensing application.

5.2.2 Contribution of Research

The dissertation contributes to the body of knowledge by providing a novel implementation of a quasi-corrugated, cylindrically symmetric, electromagnetic bandgap (EBG) structure that is

www.manaraa.com

used to mitigate unwanted side lobes that arise from inward facing antennas. This work also highlights the differences in designing for embedded antennas versus on-body inward facing antennas. To the best of the authors' knowledge, this is the first time that this type of in-plane quasi-corrugated cylindrically- symmetric EBG has been used for an on-body spiral antenna.

5.3 Conventional Spiral Antenna Design for Contact Sensing

The design of an on-body inward sensing spiral antenna is presented. A one-arm Archimedean spiral antenna is chosen as the candidate antenna due to its wideband impedance characteristics, high efficiency, and the relative ease in realizing a feeding network. A design process is presented to attain satisfactory impedance match for an antenna in contact with a human tissue-mimicking phantom. Simulated and measured results are shown for the conventional spiral antenna.

5.3.1 Archimedean Spiral Governing Equations

Archimedean spiral antennas are considered frequency independent because of the broadband pattern and impedance characteristics they exhibit [90]. A one-arm Archimedean spiral antenna [91] is modeled using the curves specified in

$$R_M = r_{in,M} + C_{exp} \cdot \Phi_{angle}, \tag{5.1}$$

where M = curve 'a' or 'b', R_M represents the radial distance along the surface, C_{exp} is the expansion coefficient of spiral (equals 1 for Archimedean spiral), Φ_{angle} is the rotation angle which is equal to 2π·(# of spiral turns), r_{in} is the inner radius of spiral at a rotation angle of zero, r_{out} is the outer radius of spiral at the maximum rotation angle, and w is the spiral width which equals to $r_{in,b}(\Phi_{angle})$ – $r_{in,a}(\Phi_{angle})$. The active region of a spiral (where coherent radiation occurs because currents along the spiral arms have identical phase) is realized when the circumference of the spiral equals one wavelength. The theoretical minimum, f_{min}, and maximum, f_{max}, frequency limit of operation are given in equation (5.2), respectively

www.manaraa.com

$$f_{min} = {}^{c}/_{\left(2\pi \cdot r_{out}\sqrt{\varepsilon_{r,eff}}\right)},$$
$$f_{max} = {}^{c}/_{\left(2\pi \cdot r_{in}\sqrt{\varepsilon_{r,eff}}\right)}, \tag{5.2}$$

where c is the speed of light, $\varepsilon_{r,eff}$ is the effective relative permittivity of the propagation medium, $r_{in} = r_{in,a}(\Phi_0)$, and $r_{out} = C_{exp} \cdot \Phi_{max} + r_{in,b}(\Phi_0)$.

5.3.2 Design Flow for On-body Inward Facing Spiral Antennas

The design process for an on-body, inward facing, one-arm Archimedean spiral antenna is described. The initial antenna dimensions are obtained from equation (5.2). A composite dielectric quantity is defined for the stratified body tissue layers. The composite or effective permittivity is the sum of all dielectric constants for each tissue layer up to the plane wave power penetration depth. The Lorentz–Lorenz effective medium approximation (EMA) is used to average the components into a composite material. The Lorentz–Lorenz EMA [92] is shown by

$$\frac{\varepsilon_{r,eff} - 1}{\varepsilon_{r,eff} + 2} = \sum_{i=1}^{N} v_i \cdot \frac{\varepsilon_i - 1}{\varepsilon_i + 2}, \tag{5.3}$$

where ε_i and v_i are complex dielectric constants and volume fractions, respectively, of layer i. The antenna is designed in a lossless effective propagation medium ($\varepsilon_{r,eff}$ from equation (5.3)) with no ground plane using the above spiral parameters. A substrate and a ground plane are added to the design at a distance very near to $\lambda_{eff}/4$ from antenna. Manufacturing process restrictions determine the closet obtainable substrate height to the $\lambda_{eff}/4$ distance. Dielectric losses are added to the full-space composite medium and the antenna parameters are re-tuned. The full space medium is replaced by finite thickness stratified lossy tissue layers and the antenna is retuned. After a satisfactory impedance match is obtained, the radiation pattern is corrected (refer to Section 5.4).

5.3.3 Conventional Spiral Antenna Geometry and Phantom Testbed Setup

The structure and final dimensions of the proposed antenna are outlined in Figure 5.1. The antenna is printed on a 6.35 mm-thick FR-4 substrate using a commercial PCB printing process. The antenna is fed with a panel mount SMA-connector with an extruded Teflon insulator. Open-ended

www.manaraa.com

stubs are inserted between the spiral windings to allow for the integration of resistive loading in order to artificially emulate substrate loss. This artificial addition of loss, highlighted in [93], is meant to intentionally reduce the radiation efficiency of the spiral antenna (by increasing substrate loss) for a future project, and is outside of the scope of this chapter. The previous statement regarding the resistive loading is only mentioned to explain the presence of the open-ended stubs.

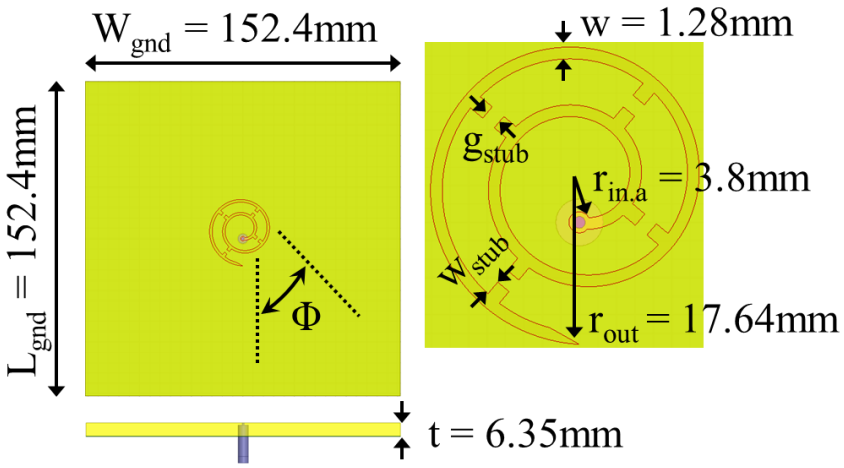

Figure 5.1 Antenna structure and dimensions. (Left) full antenna. (Right) enlarged spiral. L_{gnd} (ground length) = W_{gnd} (ground width) = 152.4mm, t (substrate thickness) = 6.35mm, $r_{in.a}$ = 3.8mm, r_{out} = 17.64mm, w = 1.28mm, Φ_a = 12.36 rad-mm, Φ_b = 12.56 rad-mm, g_{stub} (stub gap) = 1.635mm, w_{stub} (stub width) = 1.65mm.

A four-layer human tissue-mimicking phantom, where layer 1 represents solid skin phantom with a thickness of 3.3 mm, layer 2 represents solid fat phantom with a thickness of 6.25 mm, layer 3 represents a liquid muscle phantom with a thickness of 76.2 mm, and layer 4 represents air with an infinite thickness, is used during testing (Figure 5.2). Each human tissue-mimicking phantom is developed from separate recipes. More detail on the tissue phantom development is included in Chapter 4. All dielectric constants for the phantoms are independently measured and are used as theoretical values during the design phase. The frequency dependent dielectric constants of the skin, fat, and muscle human tissue-mimicking phantoms as well as a composite phantom from skin, fat and muscle are given in Figure 5.3.

www.manaraa.com

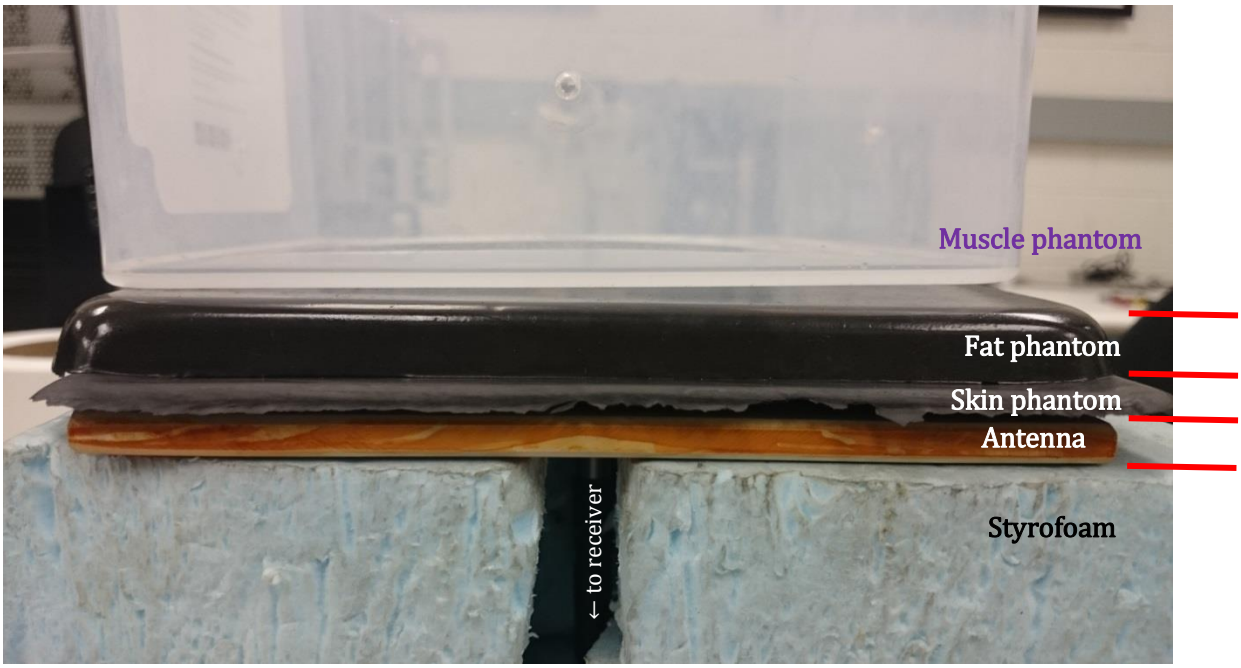

Figure 5.2 Setup for antenna in contact with tissue phantom testbed.

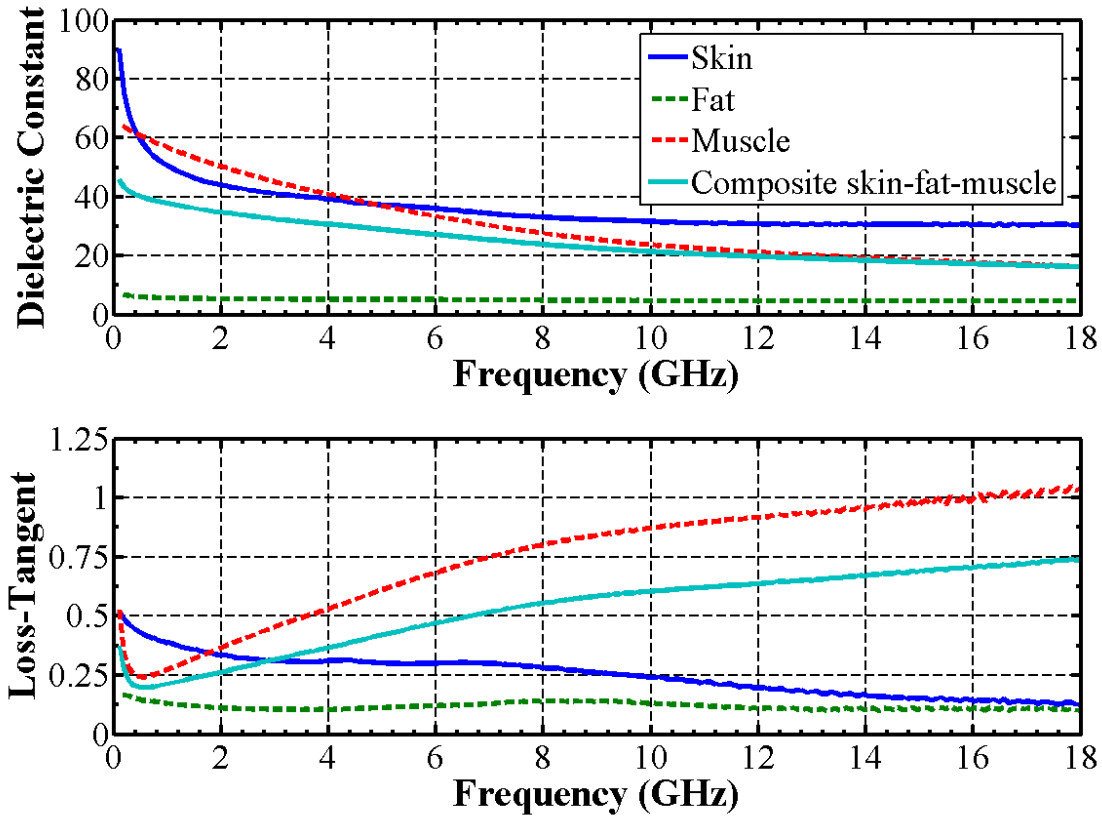

Figure 5.3 Dielectric constants and loss-tangents of human tissue-mimicking phantoms.

www.manaraa.com

5.3.4 Conventional Spiral Antenna Performance

Ansys HFSS is used to simulate the conventional antenna reflection coefficient across a frequency range of 0.1 to 3 GHz for four different propagation environments. The four propagation environments are illustrated with Figure 5.4: (a) embedded in full-space air, (b) embedded within a full-space effective dielectric body, (c) in contact with an infinite volume upper half-space effective dielectric body, and (d) in contact with a finite volume multi-layered upper space dielectric body. Figure 5.5 shows the simulated reflection coefficients for the conventional antenna with the four abovementioned cases. Each simulated case gives a similar reflection coefficient response. These reflection coefficient similarities imply that simpler design scenarios (the full-space and half-space composite setups) can be used as an initial approximation for more complex design scenarios (the stratified multi-layer setup). Figure 5.6 compares the conventional antenna simulated and measured reflection coefficients for propagation environment's (a) in air and (d) in contact with a finite volume multilayer upper half-space dielectric body. A network analyzer is used to measure the reflection coefficient for the fabricated conventional antenna in contact with the stratified human tissue phantom. The reflection coefficient for both the measured and simulated on-body sensing scenario is better than -10dB over the frequency range of 0.4 to 3+ GHz. Likewise, the reflection coefficient is better than -20dB over the frequency ranges of 0.9 to 1.55 GHz and 1.8 to 2.4 GHz for the measured on-body sensing scenario and better then -20dB over the frequency range of 0.72 to 2.52 GHz for the same simulated scenario. The measured and simulated reflection coefficients for the antenna in the air match reasonably well. However, the measured reflection coefficient for the on-body antenna displays more resonances than the simulated response. These differences are believed to be due to the uncertainty in the measurement of the actual permittivity value of the phantoms used during measurements. A notable difference between the simulation and actual setup lies in the assumption that there is a static dielectric constant per frequency for each

www.manaraa.com

individual phantom when in reality the actual phantom exhibits changes in the dielectric constant with spatial area and depth.

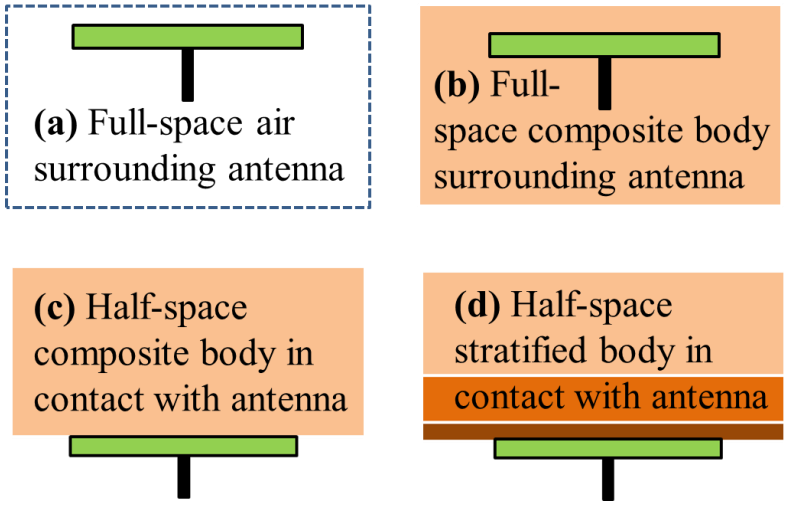

Figure 5.4 Setup for antenna in different propagation environments: (a) full-space air, (b) full-space composite body, (c) infinite volume upper half-space composite body, (d) finite volume half-space stratified body.

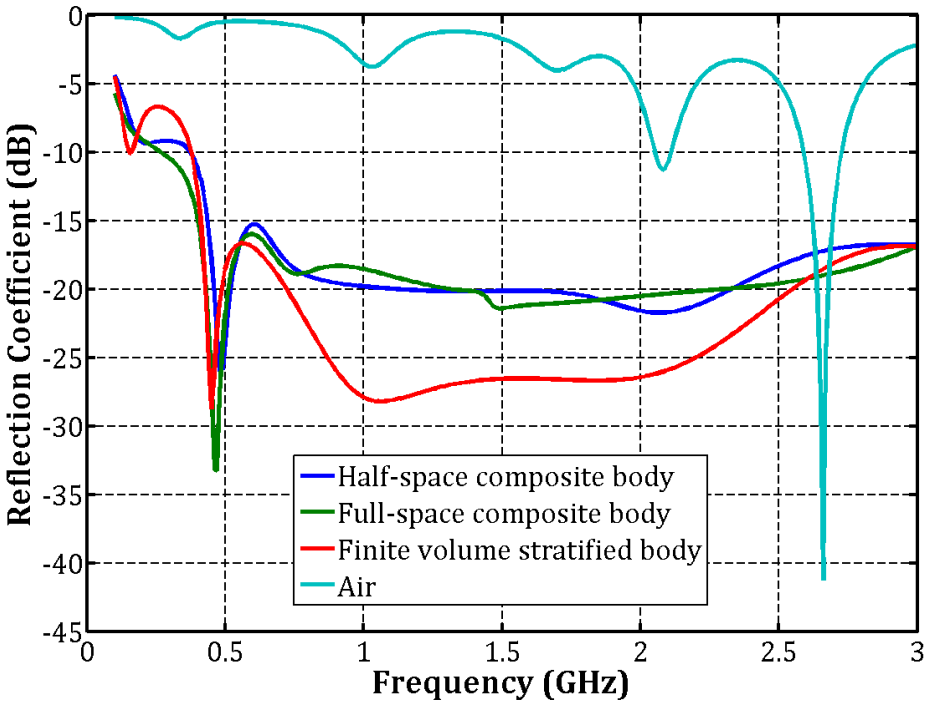

Figure 5.5 Simulated reflection coefficient for conventional antenna within propagation environments include: (a) full-space air, (b) full-space composite body, (c) infinite volume half-space composite body, (d) finite volume half-space stratified body.

www.manaraa.com

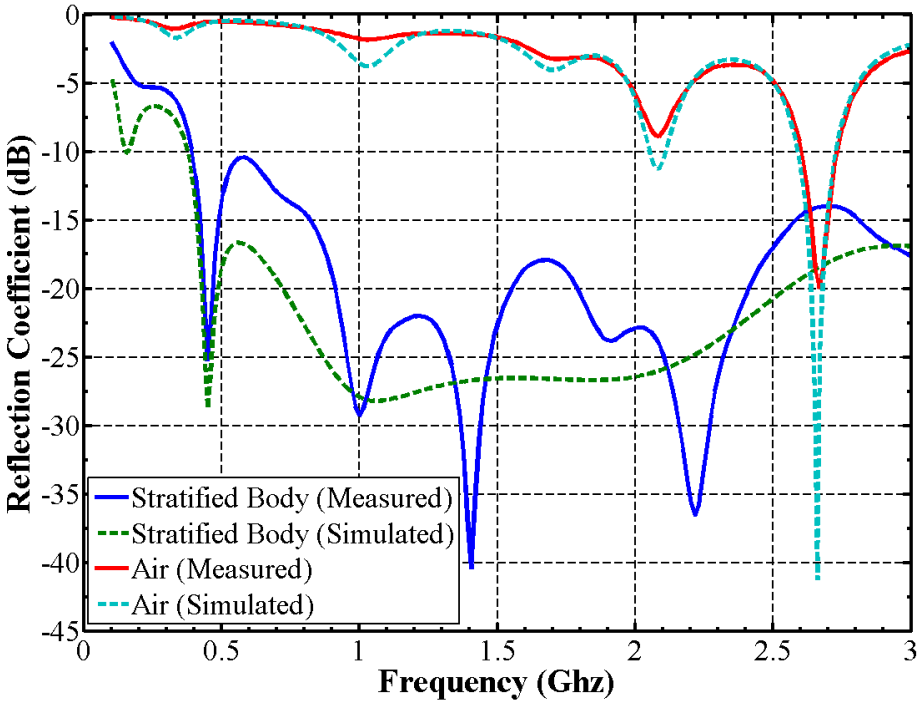

Figure 5.6 Measured and simulated reflection coefficient for conventional antenna in propagation environments (a) full-space air and (d) finite volume stratified half-space body.

Ansys HFSS is also used to simulate the antenna radiation patterns at 1.4 GHz. The fabricated antenna radiation patterns are measured in an anechoic chamber. The normalized realized gains for the four simulated cases are given in Figure 5.7. The antenna pattern is maximized in the side direction for the full-space case, while the pattern is maximized in the reverse direction for the half-space cases. The difference in the propagation environment is notable because the full-space lossy body (which emulates an embedded antenna) provides equal attenuation in all directions and helps to more evenly distribute the antenna pattern. The nulls in all patterns (which are more pronounced in the full-space pattern) are the result of surface wave propagation causing destructive interference. In contrast, on-body inward facing antennas only have attenuation in the forward direction from the body and no losses in all other directions from air. As the half-space patterns suggest, a surface wave suppression method must be implemented in order to ensure that the antenna has an adequate pattern for on-body sensing. Both half-space patterns are similar which implies that the composite scenario can be used as an initial

www.manaraa.com

approximation for the stratified scenario. The measured and simulated radiation patterns for the antenna in air and in contact with the body are given in Figure 5.8 and Figure 5.9, respectively.

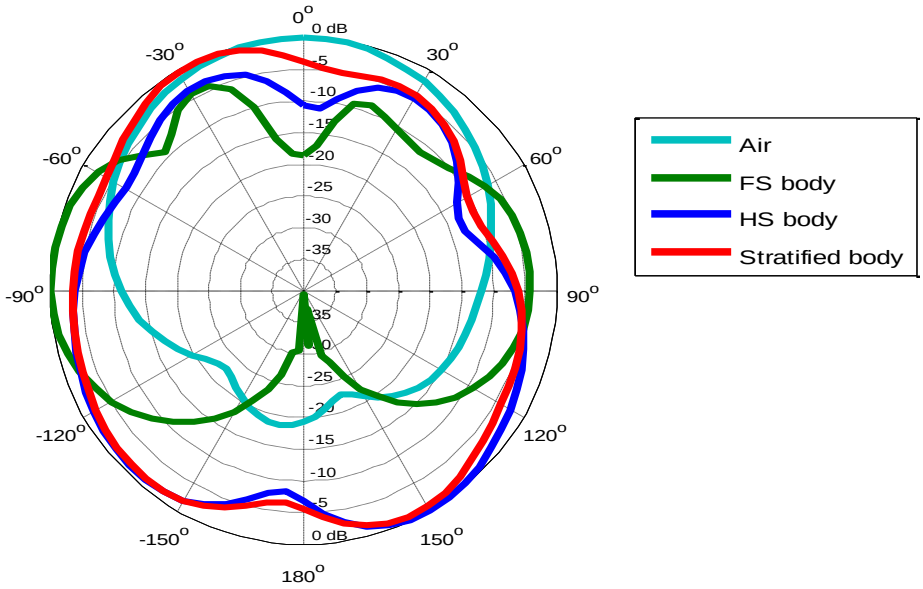

Figure 5.7 Simulated radiation pattern for conventional antenna within propagation environments include: (a) full-space air, (b) full-space composite body, (c) infinite volume half-space composite body, (d) finite volume half-space stratified body.

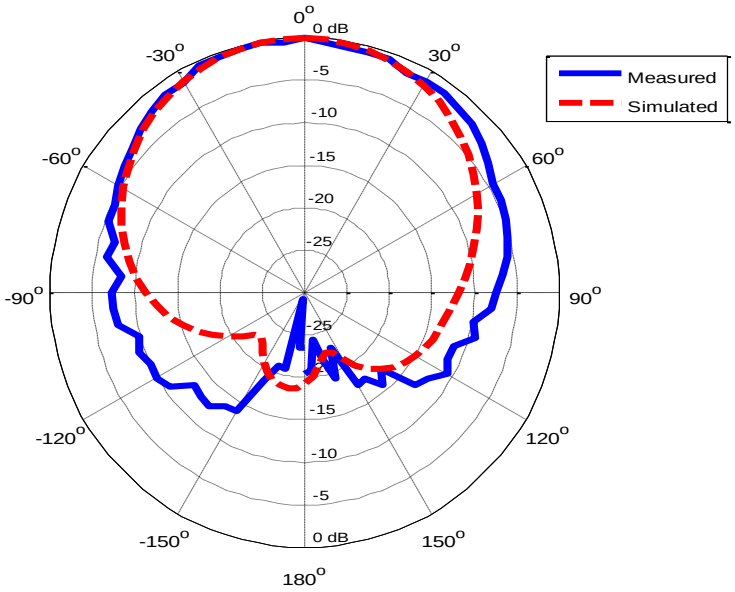

Figure 5.8 Measured and simulated radiation pattern for conventional antenna in propagation environment (a) full-space air.

www.manaraa.com

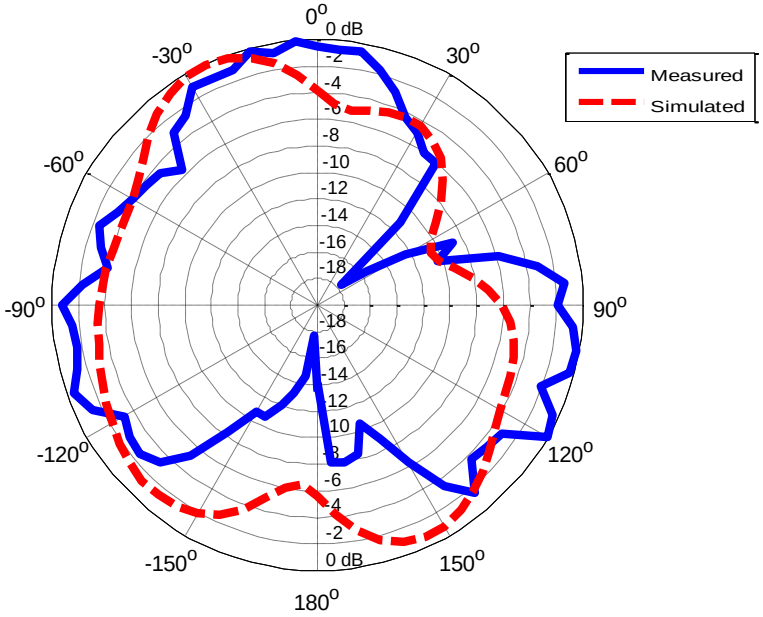

Figure 5.9 Measured and simulated radiation pattern for conventional antenna in propagation environment (d) finite volume half-space stratified body.

5.3.4.1 Conventional Spiral Antenna Efficiency

The efficiencies for the conventional spiral antenna are calculated with the principles highlighted in Appendix A. The simulated and measured main beam efficiency at 1.4 GHz for the propagation environment (d), where the spiral antenna is in contact with a finite volume multi-layered upper space dielectric body, are 45.33% and 54.43%, respectively. The simulated radiation efficiency at 1.4 GHz for the propagation environments (b), where the spiral antenna is embedded within a full-space lossless effective dielectric body, and (c), where the spiral antenna is in contact with an infinite volume upper half-space lossless effective dielectric body, are 96.908% and 95.797%, respectively. The radiation efficiency for the lossless propagation environments (b) and (c) are simulated instead of the lossless propagation environment (d) due to the increased memory constraints involved with simulating the multi-layered finite volume body.

5.4 Improvement to On-Body Inward Facing Antenna Design using an EBG Structure

The design of an in-plane continuous EBG cylindrical structure is presented and integrated with the previous conventional spiral antenna design. Simulated and measured results are

www.manaraa.com

presented for a spiral antenna integrated with the EBG structure. Radiation characteristics are compared for the scenarios with and without the EBG structure.

5.4.1 Pattern Correction Using an EBG Structure

Special attention must be paid to the design of inward facing on-body antennas in order to mitigate unwanted side lobes that arise in the antenna pattern. For microstrip antennas, these augmented side lobes can occur due to the unwanted propagation of surface waves. Dielectric slabs and metal surfaces over a ground plane (non-grounded structures) support surface waves. As Figure 5.10 suggests, surface waves radiate when discontinuities exist within an antenna structure. The surface waves that become trapped in the substrate, travel toward and lead to diffraction at the edges of a finite ground plane. This ground plane edge diffraction leads to unwanted radiation into the propagation medium. Surface wave propagation can negatively affect the efficiency and radiation pattern of a microstrip antenna and can also cause undesirable mutual coupling between neighboring devices [89].

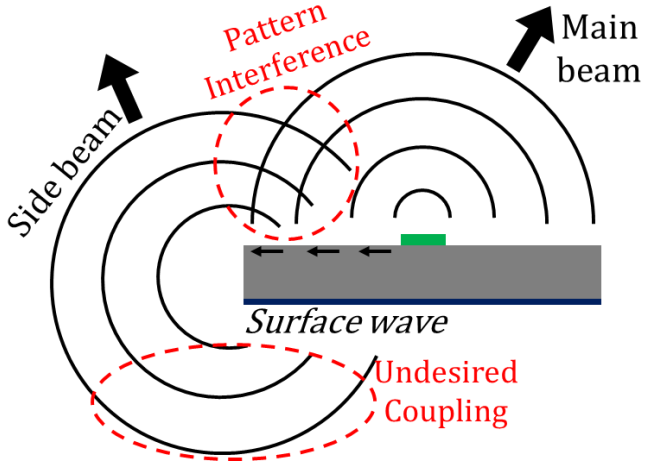

Figure 5.10 Surface-wave propagation for a conventional antenna above a finite ground plane.

Electromagnetic bandgap (EBG) structures have been used to alter the geometry of a structure so that surface waves can be attenuated as they travel across the structure [89]. The corrugated structure (Figure 5.11), a type of EBG, is a metal slab where vertical slots have been cut

www.manaraa.com

out [94]. The slots are treated as a parallel-plate transmission line where the slot depth is typically one-quarter wavelength long. The ground plane (or short circuit) at the bottom of the slot is transformed into an open circuit at the top of the slot and this transformation results in a high impedance value. Describing this process in another way, the corrugated structure makes the ground plane appear electrically larger due to the current travelling a longer distance in contrast to a planar ground plane. Also, the slot depths can be reduced by introducing a loading material. Dielectric loading for the corrugated structure has drawbacks due to special machining which is not practical, along with an increased cost and weight that is required to realize the one-quarter wavelength corrugated structure slot depth for lower frequencies.

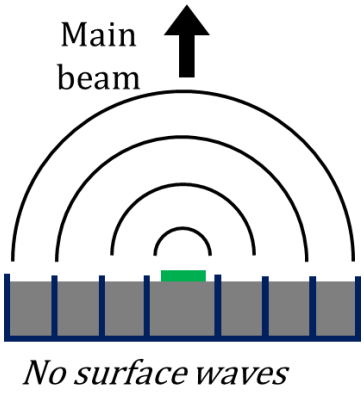

Figure 5.11 Corrugated EBG structure limiting surface-wave propagation for a conventional antenna above a finite ground plane.

The EBG structure used in this work is an evolution from the typical corrugated structure. The presented structure combines the advantages of the typical corrugated structure with the low profile geometry of the Sievenpiper mushroom-like structure [95]. The basic premise of the proposed EBG is that both dielectric loading and the inductance to ground can be increased to lower the EBG structure resonance frequency. There must be many corrugations per wavelength, but the number of corrugations is managed with consideration to both the amount of available surface area on the substrate and the manufacturing process limitations (*e.g.* smallest feature size capability).

www.manaraa.com

5.4.2 Spiral Surrounded by a Cylindrically Symmetric EBG

The structure and final dimensions for the proposed antenna are identical to the conventional antenna, described in Section 5.3.3, with the exception of an array of in-plane continuous grounded concentric annular rings surrounding the antenna (herein referred to the EBG spiral antenna). Figure 5.12 shows both a full-view and zoomed-in view of the EBG spiral antenna. Annular rings, 0.64 mm-wide, on the substrate surface are spaced 1.92 mm-apart. Vias to ground with diameters of 0.3048 mm are placed every 11.25° on each annular ring. A floating conductor with a width of 1.1276 mm is wedged between every two consecutive grounded annular rings. The floating and grounded conductors are separated with a 0.3962 mm-gap.

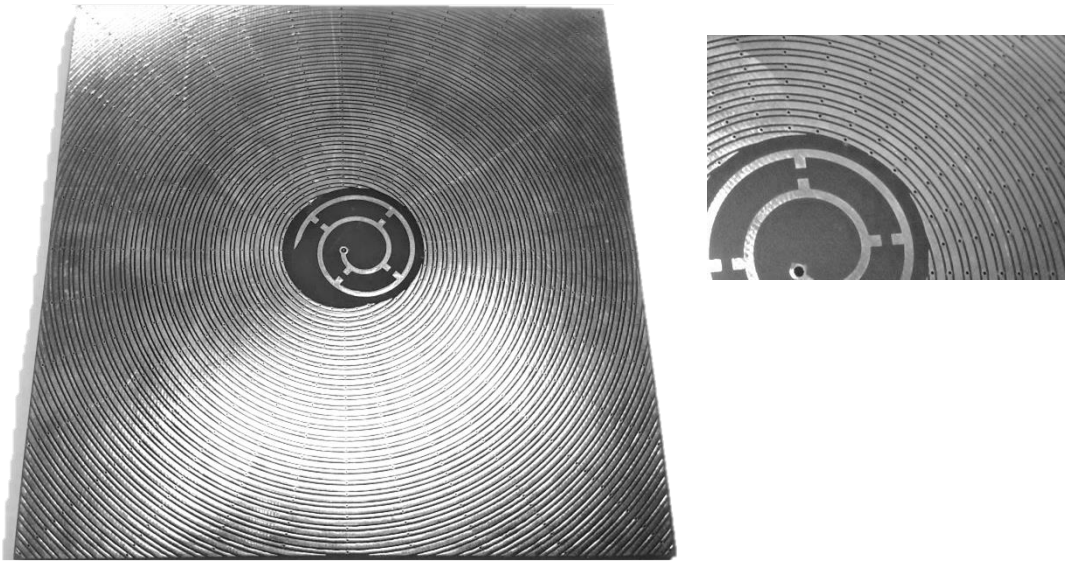

Figure 5.12 Full-view (left) and zoomed-in view (right) of the EBG spiral antenna.

5.4.3 EBG Structure Unit-Cell and an Equivalent Circuit for Dispersion Analysis

The EBG structure surrounding the antenna is cylindrically periodic, so a radial unit-cell is formed from a slice of the EBG array sectored halfway between two vias and the center of board (Figure 5.13). The radial unit-cell is transformed into the rectangular unit-cell (seen in Figure 5.14). The corresponding rectangular unit-cell of the EBG structure consists of a grounded conductor with a 0.64 mm-width (w_{cond_gnd}) and a via with a 0.3048 mm-diameter (dia_{via}) wedged between floating

www.manaraa.com

conductors with a 1.1276 mm-width (w_{cond_float}) and a 0.3962 mm-gap width (gap). The unit cell 9.5504 mm-length ($length_{uc}$) represents the average radial arc length of the EBG array for an 11.25° via separation ($spacing_{via}$). An average arc length is calculated since the arc length varies from the maximum $r_{corr,max}$ and minimum $r_{corr,min}$ corrugation radius.

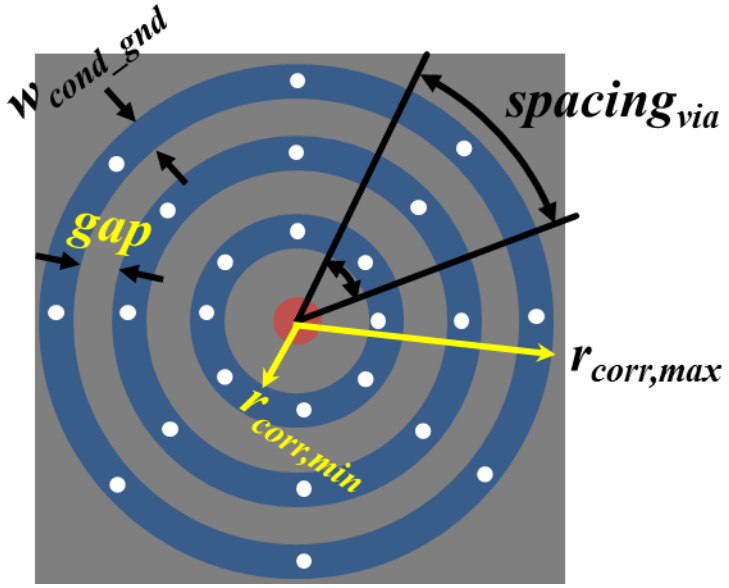

Figure 5.13 Generic EBG structure showing how the radial unit-cell is transformed into a rectangular unit-cell.

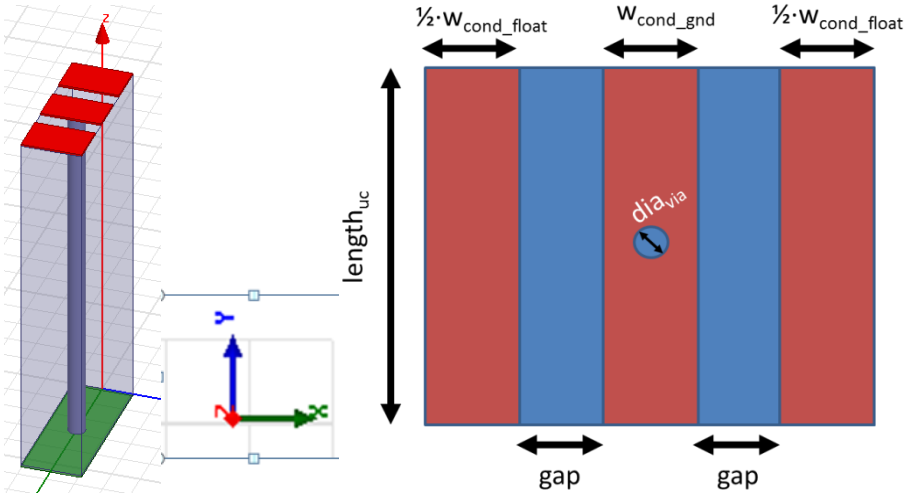

Figure 5.14 Rectangular EBG unit cell.

www.manaraa.com

5.4.3.1 EBG Unit-Cell Equivalent Circuit Dispersion Analysis

The equivalent circuit for the EBG unit-cell is given in Figure 5.15. The unit cell is modeled by (1) a transmission line section of length $0.5 \cdot l_1$, (2) a capacitive pi-network modeling the gaps between t-lines, (3) another transmission line section of length $0.5 \cdot l_2$, and (4) a shunt inductance at the midpoint of the unit cell modeling the via to ground. The unit cell is symmetric about the inductor.

Applying dispersion analysis concepts similar to [30, 96], the ABCD matrix parameters for a cascade of all unit-cell elements are given by

$$\begin{aligned}\begin{bmatrix} A & B \\ C & \mathrm{D} \end{bmatrix} &= T_{TL_1} T_{C_2} T_{C_1} T_{C_2} T_{TL_2} T_{2L} \cdot T_{2L} T_{TL_2} T_{C_2} T_{C_1} T_{C_2} T_{TL_1} \\ &= \begin{bmatrix} \cos\left(\frac{\beta l_1}{2}\right) & jZ_0 \sin\left(\frac{\beta l_1}{2}\right) \\ jY_0 \sin\left(\frac{\beta l_1}{2}\right) & \cos\left(\frac{\beta l_1}{2}\right) \end{bmatrix} \begin{bmatrix} 1 & 0 \\ j\omega C_2 & 1 \end{bmatrix} \begin{bmatrix} 1 & \frac{-j}{2\omega C_1} \\ 0 & 1 \end{bmatrix} \cdot \begin{bmatrix} 1 & 0 \\ j\omega C_2 & 1 \end{bmatrix} \cdots \\ &\quad \cdot \begin{bmatrix} \cos\left(\frac{\beta l_2}{2}\right) & jZ_0 \sin\left(\frac{\beta l_2}{2}\right) \\ jY_0 \sin\left(\frac{\beta l_2}{2}\right) & \cos\left(\frac{\beta l_2}{2}\right) \end{bmatrix} \begin{bmatrix} 1 & 0 \\ \frac{-j}{2\omega L} & 1 \end{bmatrix} \cdots \\ &\quad \cdot \begin{bmatrix} 1 & 0 \\ \frac{-j}{2\omega L} & 1 \end{bmatrix} \begin{bmatrix} \cos\left(\frac{\beta l_2}{2}\right) & jZ_0 \sin\left(\frac{\beta l_2}{2}\right) \\ jY_0 \sin\left(\frac{\beta l_2}{2}\right) & \cos\left(\frac{\beta l_2}{2}\right) \end{bmatrix} \begin{bmatrix} 1 & 0 \\ j\omega C_2 & 1 \end{bmatrix} \cdots \\ &\quad \cdot \begin{bmatrix} 1 & \frac{-j}{2\omega C_1} \\ 0 & 1 \end{bmatrix} \begin{bmatrix} 1 & 0 \\ j\omega C_2 & 1 \end{bmatrix} \begin{bmatrix} \cos\left(\frac{\beta l_1}{2}\right) & jZ_0 \sin\left(\frac{\beta l_1}{2}\right) \\ jY_0 \sin\left(\frac{\beta l_1}{2}\right) & \cos\left(\frac{\beta l_1}{2}\right) \end{bmatrix}, \end{aligned} \tag{5.4}$$

where T_{TL1}, T_{C1}, T_{C2}, T_{TL2}, and T_{2L} are the individual transmission matrices of the first t-line section with length l_1, capacitor C_1, capacitor C_2, the second t-line section with length l_2, and inductor L, respectively, and β is the propagation constant of the unloaded line. The equivalent circuit dispersion relation, which defines the passband of the structure, is given by

$$\cos(\theta) = (A + D)/2, \tag{5.5}$$

where θ is the phase shift across the full unit cell.

www.manaraa.com

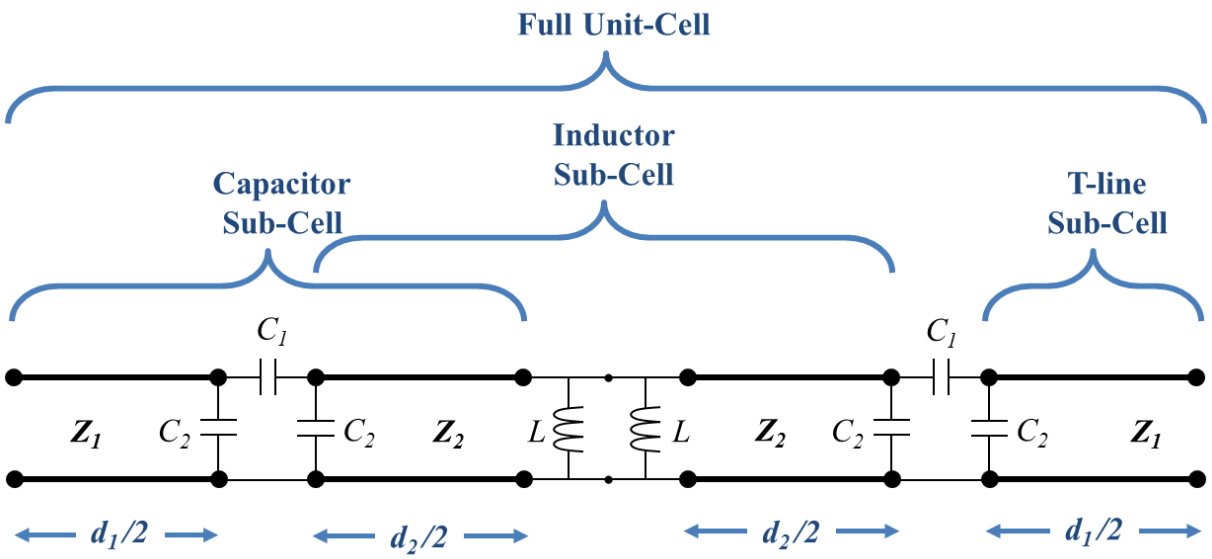

Figure 5.15 Equivalent circuit for the EBG unit-cell and designation of capacitor, inductor and transmission-line sub-cells.

While the EBG unit-cell equivalent circuit is provided above the lumped element circuit values from the sub-cell elements must be extracted. Ansys HFSS is used to model the scattering parameters of the individual sub-cell elements. The corresponding wave-port setups for the HFSS sub-cell equivalent circuit value extraction is shown for the capacitive pi-network, the shunt inductor network, and the transmission-line network in Figure 5.16, Figure 5.17, and Figure 5.18, respectively.

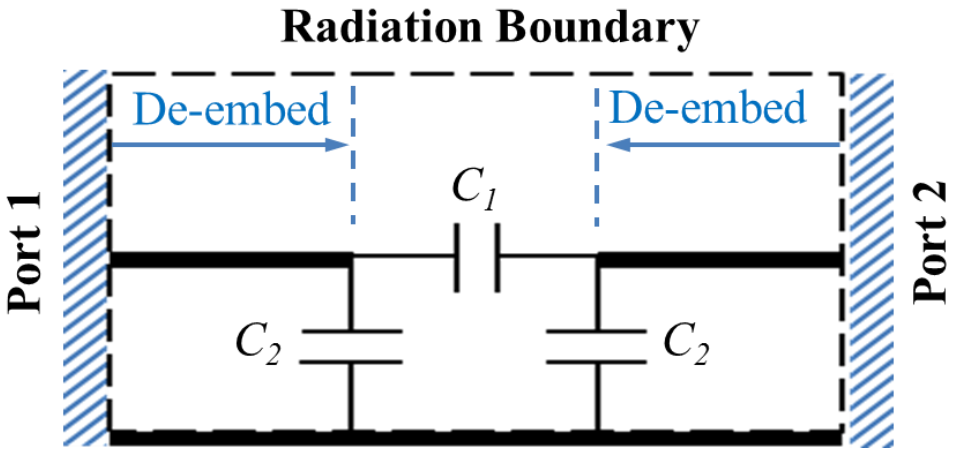

Figure 5.16 HFSS setup for capacitive pi-network.

www.manaraa.com

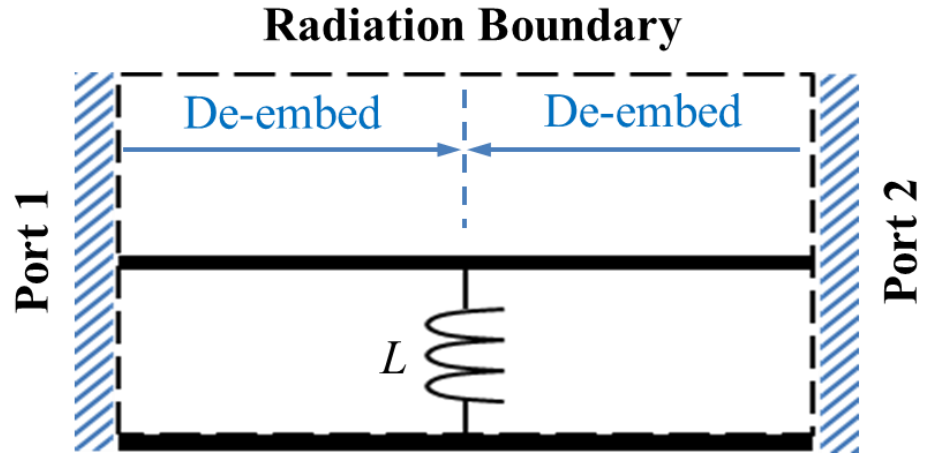

Figure 5.17 HFSS setup for inductor network.

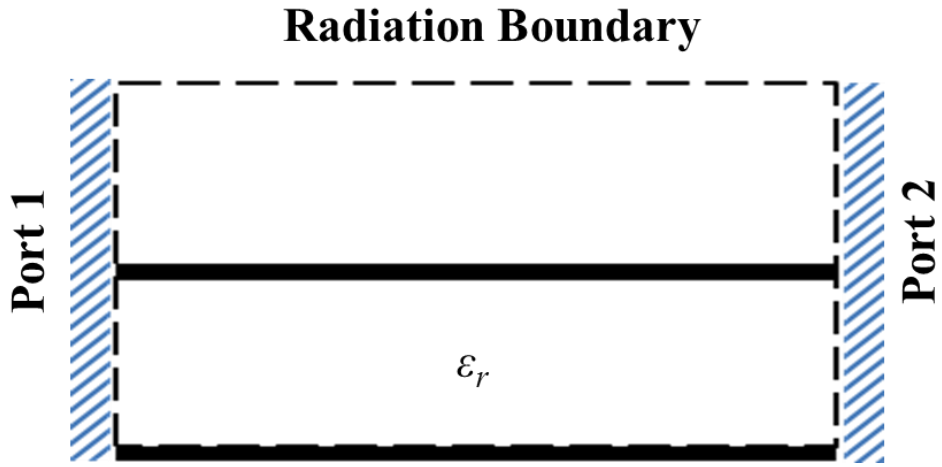

Figure 5.18 HFSS setup for transmission-line network.

The equivalent circuit lumped element values are extracted for the capacitive pi-network, the shunt inductance, and the transmission line sections using ABCD parameters [30]. The series capacitance C_{gap} in the capacitive pi-network is found by

$$C_{gap} = C_1 = \frac{-j}{\omega \cdot \mathrm{imag}(Z_C)}, \qquad Z_C = \frac{1}{-Y_{12}}. \tag{5.6}$$

where Z_c is the impedance of the capacitive pi-network and Y_{12} are the corresponding Y-parameters of the capacitive network. The shunt capacitance C_{shunt} in the capacitive pi-network is found by

www.manaraa.com

$$C_{shunt} = C_2 = \frac{\text{imag}(Y_C)}{j\omega}, \qquad Y_C = Y_{11} + Y_{12}. \tag{5.7}$$

where Y_c is the admittance of the capacitive pi-network and Y_{11} are the corresponding Y-parameters of the capacitive network. The shunt inductance L_{shunt} is found by

$$L_{shunt} = L = \frac{-j}{\omega \cdot \text{imag}(Y_L)}, \qquad Y_L = -\frac{Y_{11}Y_{22} - Y_{12}Y_{21}}{Y_{21}}. \tag{5.8}$$

where Y_L is the admittance of the inductive network and Y_{11}, Y_{12}, Y_{21}, Y_{22} are the corresponding Y-parameters of the inductive network.

5.4.3.2 EBG Unit Cell Dispersion Analysis from HFSS Simulations

Ansys HFSS eigenmode solver is used to simulate the dispersion diagram for the unit cell of the EBG surface contour along the x-direction. The x-directed bandgap, seen in Figure 5.19, falls between 1.25 to 5.97 GHz. Only the x-directed dispersion is simulated since the spiral antenna E-field propagates in the direction perpendicular to the EBG surface.

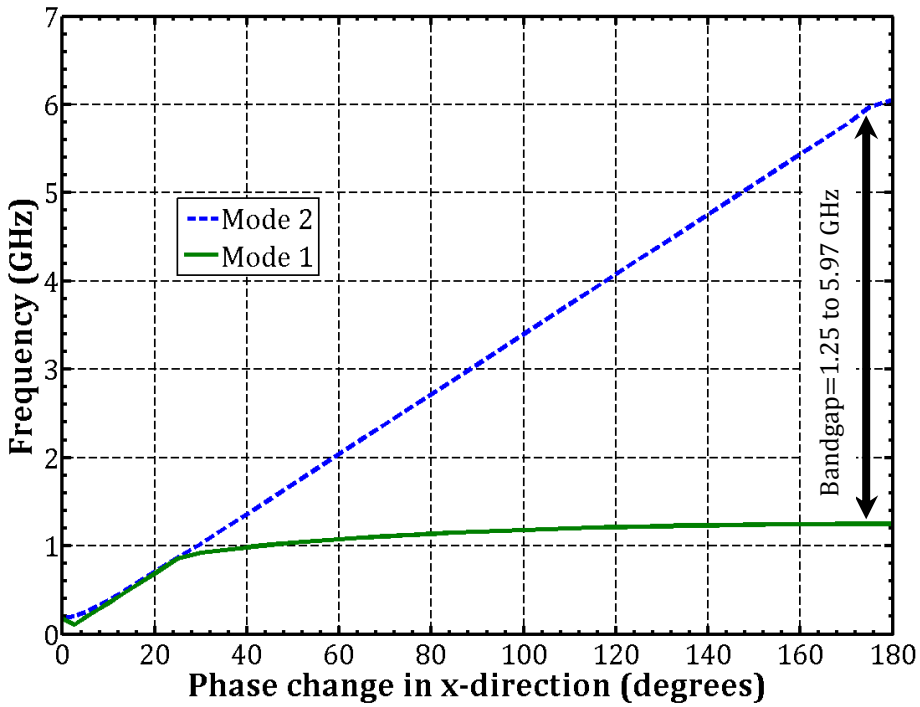

Figure 5.19 The x-directed dispersion diagram for EBG unit-cell using the ADS eigenmode solver.

www.manaraa.com

5.4.4 Spiral Antenna with EBG Performance and Results

Figure 5.20 shows the simulated reflection coefficients for the EBG antenna with the four propagation environments mentioned in Figure 5.4. The reflection properties for the antenna surrounded by the EBG structure give similar responses for both the composite and stratified propagation environments. Again, this comparable reflection coefficient response makes the composite environment ideal for the initial antenna matching design phase. The simulated and measured reflection coefficients for the on-body spiral antenna surrounded by the EBG are given in Figure 5.21. The reflection coefficient is better than -10dB over the frequency range of 0.65 to 2.1 GHz for the simulated results and better than -10dB over the frequency range of 0.65 to 1.6 GHz for the measured results.

The normalized realized gains for the four simulated cases are given in Figure 5.22. All cases exhibit higher broadside gains than in any other direction. The simulated and measured normalized gains for the on-body EBG spiral antenna at 1.4 GHz are given in Figure 5.23. The maximum side lobe and rear lobe are ~7dB and ~8dB lower, respectively, than the broadside value in both cases. Figure 5.24 compares the radiation characteristics of the EBG spiral antenna to the conventional antenna for the same on-body stratified propagation environment. A noticeable appreciation to the forward propagating antenna pattern is seen for both the simulated and measured scenarios. The EBG spiral normalized gain has the following improvements over the respective simulated and measured conventional antenna gain: broadside gain ~+3.84dB/+0dB, side gain ~-2.64dB/-7dB, and rear gain ~-8dB/-7dB.

www.manaraa.com

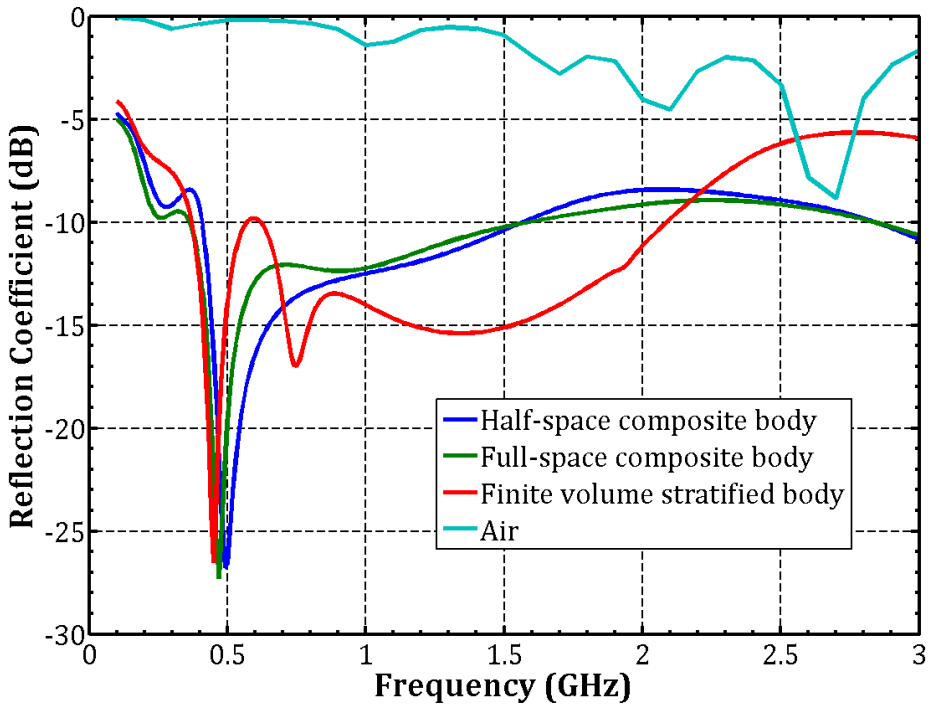

Figure 5.20 Simulated reflection coefficient of EBG antenna for four propagation environments.

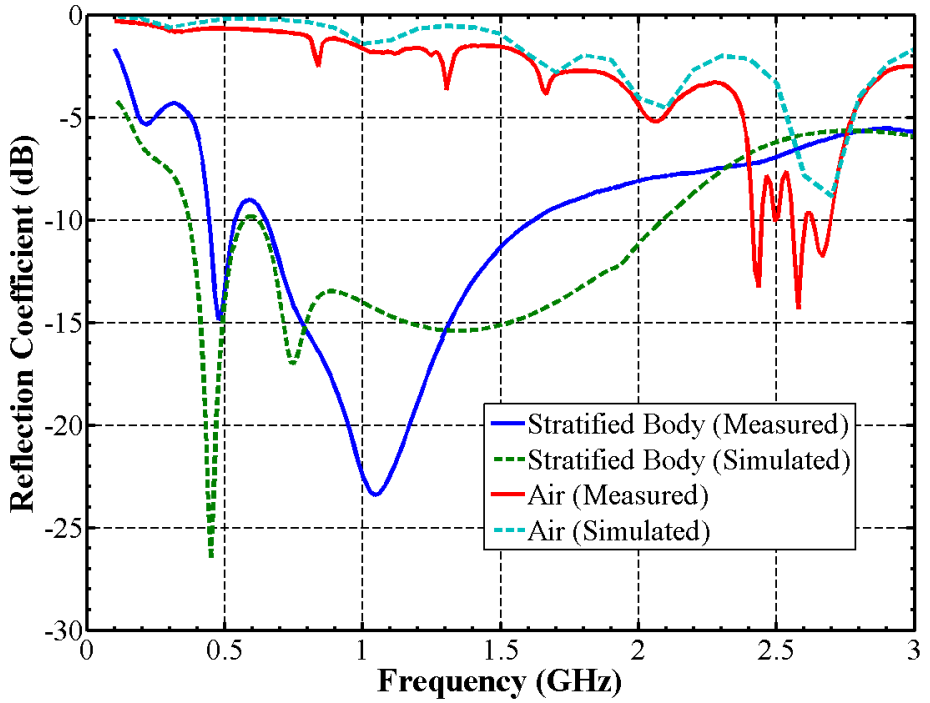

Figure 5.21 Simulated and measured reflection coefficient of EBG antenna in contact with half-space stratified human tissue phantom.

www.manaraa.com

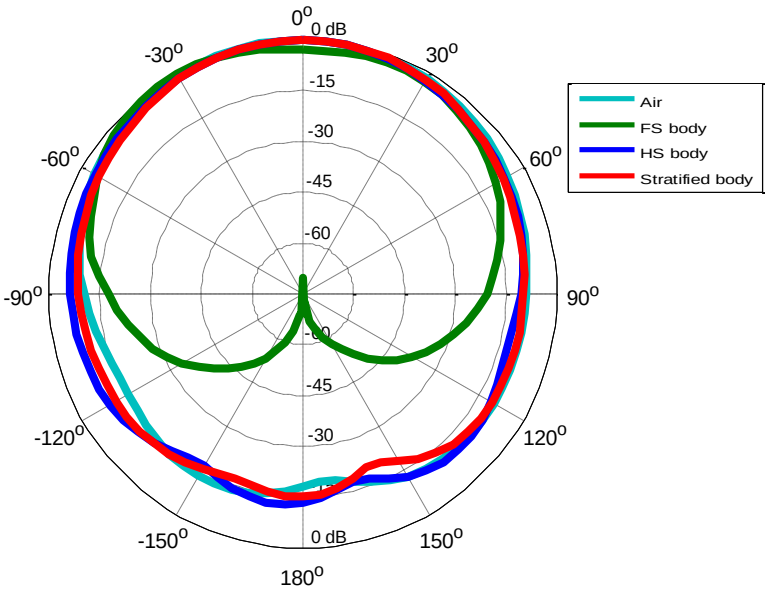

Figure 5.22 Simulated radiation pattern for EBG antenna within propagation environments include: (a) full-space air, (b) full-space composite body, (c) infinite volume half-space composite body, (d) finite volume half-space stratified body.

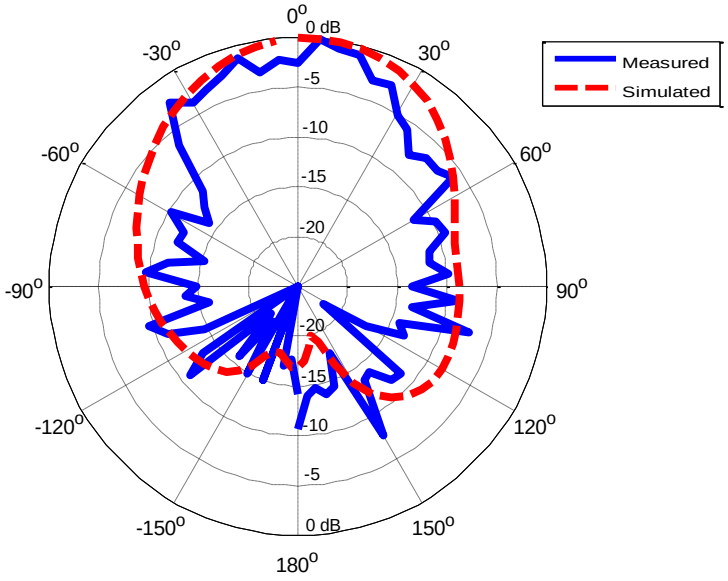

Figure 5.23 Simulated (red dashed line) and measured (blue solid line) normalized gain (dB) of EBG spiral antenna in contact with human tissue phantom.

www.manaraa.com

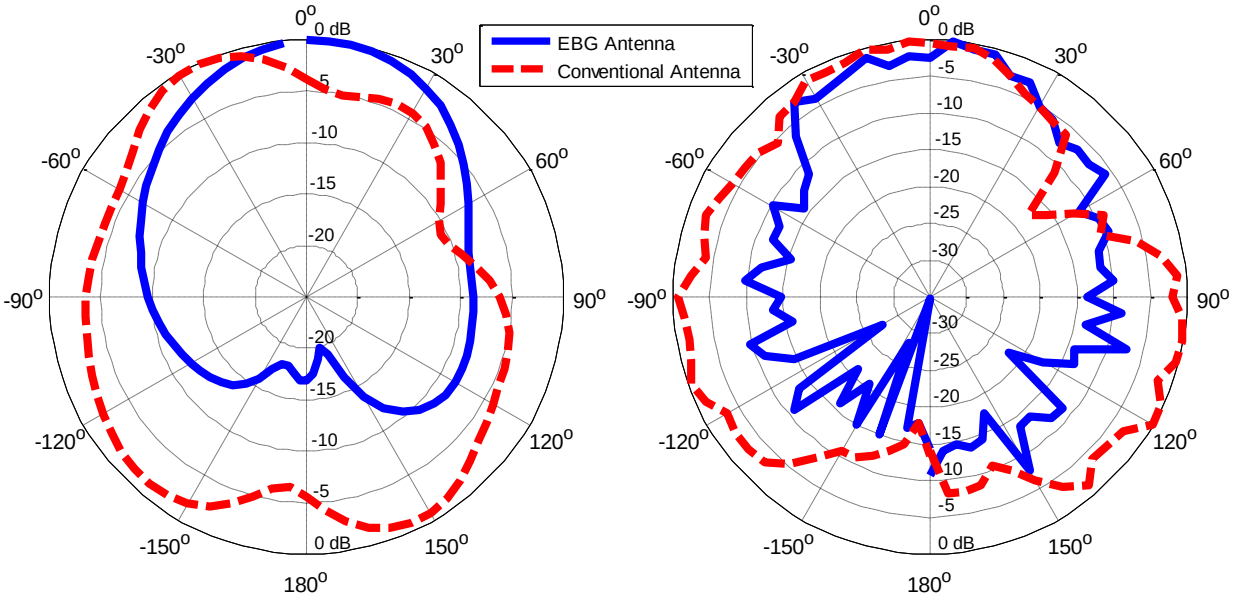

Figure 5.24 Simulated (left) and measured (right) normalized gain (dB) of EBG spiral antenna versus conventional spiral antenna in contact with human tissue phantom.

5.4.4.1 Spiral Antenna with EBG Efficiency

The efficiencies for the EBG spiral antenna are calculated with the principles highlighted in Appendix A. The simulated and measured main beam efficiency at 1.4 GHz for the propagation environment (d), where the spiral antenna is in contact with a finite volume multi-layered upper space dielectric body, are 87.59% and 86.36%, respectively. The simulated radiation efficiency at 1.4 GHz for the propagation environments (b), where the EBG spiral antenna is embedded within a full-space lossless effective dielectric body, and (c), where the EBG spiral antenna is in contact with an infinite volume upper half-space lossless effective dielectric body, are 93.58% and 95.429%, respectively.

5.5 Conclusion

Unwanted side lobes arise when designing antennas for contact human body sensing. If the antenna does not mostly radiate in the direction towards the body, it will be more sensitive to the

www.manaraa.com

outside environment and less to the body. An in-plane, continuous, quasi-corrugated, cylindrically symmetric, EBG structure is integrated with an on-body spiral antenna design to improve undesired radiation characteristics. Main beam efficiency is improved from 45.33% and 54.43% for the conventional antenna to 87.59% and 86.36% for the EBG antenna for simulated and measured beam efficiencies, respectively. Likewise, the following gain improvements (from the conventional spiral antenna to the EBG spiral antenna) were realized for the simulated and measured antenna gain, respectively: broadside gain ~ +3.84dB/+0dB, side gain ~ -2.64dB/-7dB, and rear gain ~ -8 dB/-7dB. The inclusion of the EBG structure does indeed improve the radiation characteristics of on-body inward facing antennas.

www.manaraa.com

Chapter 6 Coherent and Non-Coherent Radiative Transfer Models

6.1 Introduction

Microwave radiometry has proven to be an effective approach to achieve internal body wireless thermometry [12, 13]. Since radiometric thermometry is an entirely passive sensing technique, prior knowledge of the scattering and emission within the stratified tissues of the human body must be known in order to accurately correlate the electromagnetic (EM) behavior of the multi-layered body tissues back to the passive measurement of absolute sub-skin temperature.

The effective scattering and emission within any multi-layered dielectric structure can be described by either a coherent or non-coherent process. The coherent process accounts for both the phases and amplitudes of the fields reflected within the medium, while the non-coherent process only accounts for the amplitudes of the reflected fields within the medium. Closed-form non-coherent models for predicting radiative transfer in stratified media are useful tools for microwave (MW) radiometry, but are generally limited to a small number of layers [13, 14, 28]. In remote sensing applications, it is often sufficient to model only two or three layers of a material, e.g. snow [97], ice [98], and soil [99]. However, MW radiometry has also been shown to be a viable method to monitor internal body temperature [12-14, 22-25, 50, 100]. In that application, the ability to easily scale the number of layers is desirable since the abdominal core can have as many as seven different connective tissues [101]. Existing non-coherent closed-form models able to predict the radiative transfer for a large number of layers either use simplified formulations which omit the higher-order electromagnetic plane-wave reflections present within stratified media [99, 102, 103] or use coherent formulations which are sensitive to phase variations [104, 105]. Numerical models can be used to predict the radiative transfer in multi-layered media [12, 22-25, 50, 100], but are

www.manaraa.com

computationally more expensive than closed-form models and may not be practical for applications that require real-time monitoring and analysis. The available coherent models in literature either are (1) only applicable to isothermal (uniform temperature) media [28], (2) need numerical simulators to solve the radiative transfer throughout the medium [12, 22-25, 50, 100], or (3) offer iterative radiative transfer solutions where proper implementation is sometimes unclear [104].

This chapter presents two techniques to address the modeling of both the coherent and non-coherent radiative transfer within multi-layered media. For non-coherent modeling, signal-flow graph theory is used to expand the derivation of the non-coherent steady-state radiative transfer model in [28] to be applicable for N layers. The scalable non-coherent steady-state radiative transfer model is validated for a four-layer human body tissue-mimicking phantom testbed. To the best of the authors' knowledge, no non-coherent steady-state closed-form model is available for more than two layers and the non-coherent steady-state radiative transfer within multi-layered dielectrics has not been analyzed before using signal-flow graph theory. For coherent modeling, signal-flow graph theory is used to provide an alternate means to explain an iterative coherent radiative transfer initially highlighted by [104]. Signal-flow graph theory offers a graphical representation to apply the iterative process from [104] in a more visually clear manner. This work derives the reflection and transmission for the general case (*i.e.* within both lossy and lossless networks) by applying the conventions of power waves and generalized scattering parameters. To the best of the author's knowledge, this is the first time that this approach has been used to explain the radiative transfer within multi-layered media with non-uniform temperature distributions.

This chapter highlights the use of signal-flow graph theory to explain both the coherent and non-coherent radiative transfer through multi-layered media. Section 6.2 reviews literature on the existing coherent and non-coherent radiative transfer models. Section 6.3 derives new techniques based on signal-flow graph theory to explain non-coherent and coherent radiative transfer. Section

www.manaraa.com

6.4 validates the derived radiative transfer models with comparisons to previous radiative transfer models and electromagnetic simulations. This chapter concludes with a summary in Section 6.5. A portion of this chapter was previously published in [106]. Permission is included in Appendix A.

6.2 Review of Radiative Transfer Models for the Scattering and Emission within Stratified Media with Non-Uniform Temperature and Dielectric Profiles

Radiative transfer modeling has been used to model the thermal emission and scattering within snow [97], ice [98], soil [99], and human body tissues [12-14, 22-25, 50, 100]. The radiative transfer within a stratified medium with dissimilar layers is characterized by either a coherent [12, 22-25, 28, 50, 100, 104, 105, 107, 108] or non-coherent [13, 14, 28, 99, 102, 103] process. The coherent process accounts for both the amplitudes and phases of the waves reflected in the medium, whereas the non-coherent process only accounts for the amplitudes [28]. The radiative transfer predicted by coherent and non-coherent models give correlated solutions [106]. Coherent solutions capture the damped oscillatory behavior of a propagating wave throughout a medium, while the non-coherent solution only captures the reduction in amplitude. As compared to non-coherent models, coherent models are more sensitive to variations in the layer thicknesses due to its oscillatory phase dependency [106]. Also, coherent models can be misleading when used to approximate the emission and scattering for discrete layers [28]. For example, [106] showed that a 15-percent change in the layer one thickness for a two-layer medium can result in a scattering approximation difference of ~52-percent for the coherent model due to the oscillatory phase dependency. In contrast, under the same conditions the non-coherent model results in a scattering approximation difference of less than two-percent due to the non-coherent model only accounting for the amplitude reduction effects. This difference in scattering approximation example is important to note since (1) thickness may not be accurately known in an actual sensing scenario and (2) the dielectric properties of a material are frequency dependent.

www.manaraa.com

6.2.1 Coherent Scattering and Emission Models

The basic coherent model for uniform temperature distributions (*i.e.* isothermal temperatures) is the transmission-line equivalent model. The transmission-line equivalent formulation [28] predicts the coherent scattering in multi-layered media. Figure 6.1 illustrates the modeling of a two-layer medium as depicted by a transmission line equivalent model. Layer 0, layer 1, and layer 2 are characterized by the impedances Z_0, Z_1, and Z_2, respectively. Layer 2 presents the input impedance Z_{in2} at the output of transmission line 1 since it extends out to infinity.

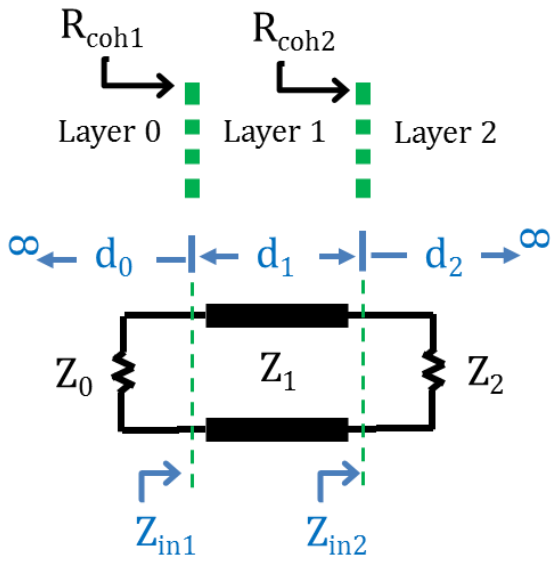

Figure 6.1 Reflection from a plane stratified medium consisting of a layer of thickness d_1 above a semi-infinite last layer: (top) cross-section of the two-layer problem; (bottom) transmission-line equivalent formulation.

The input impedance Z_{in1} looking into layer 1 is obtained by transforming the impedance Z_2 through layer 1, as given by

$$Z_{in1} = Z_1 \left[\frac{1 + (R_{coh2}/L_{P1}) e^{-j2\beta_1 d_1}}{1 - (R_{coh2}/L_{P1}) e^{-j2\beta_1 d_1}} \right], \tag{6.1}$$

where

$$R_{coh2} = \frac{Z_{in2} - Z_1}{Z_{in2} + Z_1} \quad \text{and} \quad Z_{in2} = Z_2 \tag{6.2}$$

and

www.manaraa.com

$$L_{P1} = e^{2\alpha_1 d_1}\,, \tag{6.3}$$

with

$$Z_o = 377\Omega\,, \quad Z_0 = Z_o/\sqrt{\varepsilon_{r0}}\,, \quad Z_1 = Z_o/\sqrt{\varepsilon_{r1}}\,, \quad Z_2 = Z_o/\sqrt{\varepsilon_{r2}}\,, \tag{6.4}$$

$$\alpha_1 = \frac{2\pi}{\lambda_0}\cdot\left|\,\Im\left[\sqrt{\varepsilon_{r1}}\,\right]\right|, \tag{6.5}$$

and

$$\beta_1 = \frac{2\pi}{\lambda_0}\cdot\Re\left[\sqrt{\varepsilon_{r1}}\,\right], \tag{6.6}$$

where Z_{in1} is the input impedance looking into medium 1, R_{coh2} is the reflection coefficient looking into boundary 2, L_{P1} is the dielectric power loss-factor through layer 1, α_1 is the attenuation coefficient of layer 1, β_1 is the propagation coefficient of layer 1, ε_{r1} is the complex relative permittivity, ε'_{r1} is the real relative permittivity, ε''_{r1} is the imaginary relative permittivity of layer 1, $\Im[\,]$ is the imaginary operator, and $\Re[\,]$ is the real operator. The reflection coefficient R_{coh1} looking into boundary 1 and coherent reflectivity Γ_{coh1} are given by

$$R_{coh1} = \frac{Z_{in1} - Z_0}{Z_{in1} + Z_0} \quad \text{and} \quad \Gamma_{coh1} = |R_{coh1}|^2. \tag{6.7}$$

Coherent formulations which account for the scattering and emission from stratified media with non-uniform temperature distributions can be found in [104, 105, 107, 108]. Reference [103] highlights that references [104, 105, 107] are based on similar assumptions, but the Wilheit formulation [104] is the easiest to implement because of its numerical form. The Wilheit formulation is highlighted below. Naming conventions have been changed to match with this work. In the Wilheit formulation, the field equations are solved for a multi-layered dielectric profile in order to find the thermal radiation from each layer. The thermal radiation calculated from each layer is used to solve the apparent temperature given by

$$\begin{aligned} T_{AP}^{[\text{Wilheit}]} &= T_B^{[\text{Wilheit}]} + T_0\cdot\Gamma_{iso.coh}^{[\text{Wilheit}]} \\ &= \left(1-\Gamma_{iso.coh}^{[\text{Wilheit}]}\right)\cdot T_{B,eff}^{[\text{Wilheit}]} + T_0\cdot\Gamma_{iso.coh}^{[\text{Wilheit}]}, \end{aligned} \tag{6.8}$$

www.manaraa.com

with

$$T_{B,eff}^{[\text{Wilheit}]} = \frac{1}{1 - \Gamma_{iso.coh}^{[\text{Wilheit}]}} \cdot \sum_{j=1}^{N} f_j \cdot T_j \tag{6.9}$$

where $T_B^{[\text{Wilheit}]}$ is the brightness temperature, $T_{B,eff}^{[\text{Wilheit}]}$ is the effective brightness temperature, $\Gamma_{iso.coh}^{[Wilheit]}$ is the isothermal coherent reflectivity, T_0 is the physical temperature of layer 0, T_j is the physical temperature of layer j, and f_j is the fraction of radiation incident on the first layer which would be absorbed by the j-th layer (*i.e.* the emissivity of each layer). For the isothermal case, equation (6.8) reduces to

$$1 = \sum_{j=1}^{N} f_j \; + \Gamma_{iso.coh}^{[\text{Wilheit}]}, \tag{6.10}$$

and accordingly satisfies the conservation of energy. The fraction of radiation absorbed by j-th layer is determined by

$$f_j = \frac{\Omega_{j-1} - \Omega_j}{\Omega_1} \tag{6.11}$$

where Ω_{j-1} is the net electromagnetic (EM) flux entering the j-th layer at the j-1'st interface and Ω_j is the net EM flux entering the j-th layer at the j-th interface for an EM flux Ω_1 incident on the first interface. Wilheit also provided an iterative FORTRAN subroutine that calculated the abovementioned thermal weighting functions and solved the EM field equations.

6.2.2 Non-Coherent Scattering and Emission Models

The non-coherent radiative transfer models currently available in literature include the zeroth-order [99, 103], first-order [102, 103] and steady-state [28, 103] radiative transfer models. The model order is determined by the number of plane-wave reflections accounted for within the medium (e.g. zeroth-order models account for no reflections while steady-state models account for all reflections). Each model calculates the emitted brightness temperature from a stratified medium with a non-uniform temperature and dielectric profile, as illustrated by

www.manaraa.com

$$T_{B.Nlayer}^{[\Gamma ord]} = \left(1 - \Gamma_{iso.ncoh.Nlayer}^{[\Gamma ord]}\right) \cdot T_{B,eff.Nlayer}^{[\Gamma ord]} = \left(1 - \Gamma_{ncoh.Nlayer}^{[\Gamma ord]}\right) \cdot T_0 \,, \tag{6.12}$$

where $T_{B.Nlayer}$ is the brightness temperature for an N-layer medium, Γ_{ord} is the order of reflections accounted for within the medium, $\Gamma_{iso.ncoh.Nlayer}$ is the isothermal non-coherent effective reflectivity, $\Gamma_{ncoh.Nlayer}$ is the non-coherent effective reflectivity, T_0 is the physical temperature of layer 0, and $T_{B,eff.Nlayer}$ is the effective brightness temperature for an N-layer medium. Diffuse scattering is ignored within all presented models, but it is discussed further in [28].

A zeroth-order general-form radiative transfer model [99, 103] ignores all reflection losses present within a stratified dielectric medium. The zeroth-order general-form brightness temperature is given in (6.12), where $\Gamma_{ord} = 0$ and

$$T_{B.Nlayer}^{[0]} = (1 - \Gamma_{B1}) \cdot \sum_{j=1}^{N} T_j \cdot \left(1 - \frac{1}{L_{Pj}}\right) \cdot \prod_{k=2}^{j} \left(\frac{1}{L_{Pk-1}}\right), \tag{6.13}$$

where T_j and L_{Pj} are the physical temperature and the dielectric loss factor, respectively, for layer j. Γ_{Bj} is the Fresnel reflectivity for the boundary between layers j and j-1. The N-th layer dielectric loss factor L_{PN} is equal to infinity since the last layer has an infinite thickness. The first-order general-form radiative transfer model [102, 103] contains both the forward propagation reflection losses at every interface and the dielectric loss factors in every layer above the emitting layer. The first-order general-form brightness temperature is presented in (6.12), where $\Gamma_{ord} = 1$ and

$$T_{B.Nlayer}^{[1]} = (1 - \Gamma_{B1}) \cdot \sum_{j=1}^{N} T_j \cdot \left(1 - \frac{1}{L_{Pj}}\right)\left(1 + \frac{\Gamma_{Bj+1}}{L_{Pj}}\right) \cdot \prod_{k=2}^{j} \left(\frac{1 - \Gamma_{Bk}}{L_{Pk-1}}\right) , \tag{6.14}$$

Using similar naming conventions as (6.13) and (6.14), a second-order general-form radiative transfer model is derived. The second-order general-form radiative transfer model contains all reflections and dielectric loss factors of the first-order model with the addition of the multiple reflections existing between bounded layers above the emitting layer. The second-order general-form brightness temperature is specified by (6.12), where $\Gamma_{ord} = 2$ and

www.manaraa.com

$$T_{B.Nlayer}^{[2]} = (1-\Gamma_{B1})\cdot\sum_{j=1}^{N} T_j\cdot\left(1-\frac{1}{L_{Pj}}\right)\left(1+\frac{\Gamma_{Bj+1}}{L_{Pj}}\right)\cdot\prod_{k=2}^{j}\left(\frac{1-\Gamma_{Bk}}{L_{Pk-1}}\right)\cdots \cdot\prod_{k=1}^{j}\left(1-\frac{\Gamma_{Bk}\cdot\Gamma_{Bk+1}}{L_{Pk}^2}\right)^{-1}. \quad (6.15)$$

A steady-state radiative transfer model is derived in [28] for a two-layer medium. The layer naming convention for this model has been changed to align with the naming conventions of this chapter. The steady-state two-layer brightness temperature is given in (6.12), where Γ_{ord} = SS and

$$T_{B.2layer}^{[SS]} = (1-\Gamma_{B1})\cdot\left(1-\frac{\Gamma_{B1}\Gamma_{B2}}{L_{P1}^2}\right)^{-1}\cdot\left[T_1\cdot\left(1-\frac{1}{L_{P1}}\right)\cdot\left(1+\frac{\Gamma_{B2}}{L_{P1}}\right)+T_2\cdot\left(\frac{1-\Gamma_{B2}}{L_{P1}}\right)\right]. \quad (6.16)$$

An abridged steady-state radiative transfer model for a three-layer medium is derived in [14] which follows a similar procedure as in [28], but ignores the reflection loss at interface 3. The existing procedure involved in calculating the steady-state non-coherent reflectivity for the two-layer medium, equation (6.16) originally presented in [28], is highlighted in Figure 6.1. Following the emission paths originating from layer 2, the temperature source T_{s2} transmits though boundary 2 (contributing to a reduction in the signal of $1-\Gamma_{B2}$). This resulting signal travels through layer 1 experiencing a loss of L_{P1} before it transmits through boundary 1 ($1-\Gamma_{B1}$). The portion of the signal that is not transmitted through boundary 1 gets reflected back toward boundary 2 and a series of multiple reflections between boundaries 1 and 2 ensue (contributing to the term $1/[1-\Gamma_{B1}\Gamma_{B2}L_{P1}^{-1}]$). Thermal emissions originating from layer 1 also experience the same process.

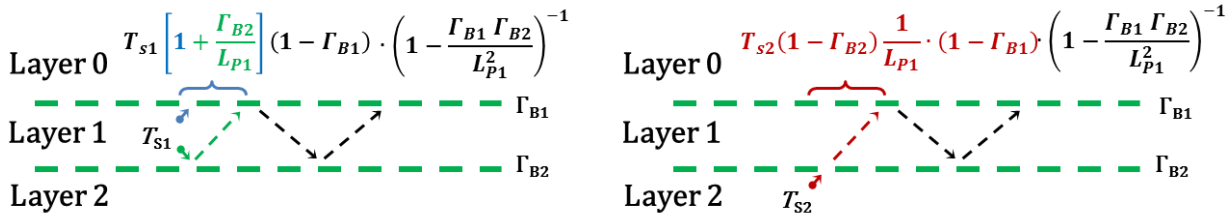

Figure 6.2 Derivation of the thermal emissions originating from layer 1 (left) and layer 2 (right) in the steady-state non-coherent brightness temperature derivation

www.manaraa.com

Expanding on the concept from above, the difference in the order of reflections from the zeroth-order model to the steady-state model can be observed from Figure 6.3. Figure 6.3 shows a cross-section of a three-layer stratified medium where all reflections are present for the thermal emissions originating from layer 1. $T^{[0]}_{B.3layer}$, $T^{[1]}_{B.3layer}$, $T^{[2]}_{B.3layer}$, and $T^{[SS]}_{B.3layer}$ are given by the emission paths illustrated in purple, blue, red, and gray, respectively. The emission paths omitted by the lower-order models are illustrated in gray. The number of omitted emission paths increase as the number of stratified layers increase.

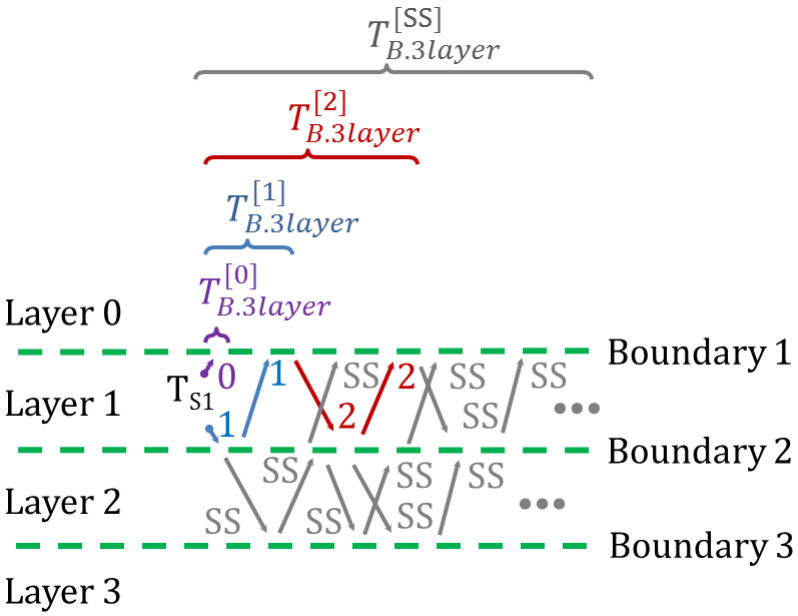

Figure 6.3 Cross-section of a three-layer stratified medium showing reflections originating from layer 1 with the following emission paths: zeroth-order → [0] (purple), first-order → [1] (blue), second-order → [2] (red), steady-state → [SS] (grey).

6.2.3 Gap in Literature

In current literature, the derivation for both coherent and non-coherent emission and scattering models are not always straightforward to comprehend and implement. Speaking to this point, two gaps are addressed in this chapter (one for coherent modeling and another for non-coherent modeling). Addressing the need in coherent modeling leads to a focus on the Wilheit coherent model. While the Wilheit coherent formulation provides an adequate means to predict the

www.manaraa.com

coherent radiative transfer emitting from multi-layered dielectrics, proper implementation of the concepts highlighted in the Wilheit paper are difficult to implement in its current form. In regards to the gap in non-coherent modeling, omission of emitted radiative transfer paths in the non-coherent formulations translate into increasingly more error being introduced into the brightness temperature model as the layer count increases. All lower order models are presented in the general form, but a steady-state general-form model does not currently exist in literature.

6.2.4 Contribution of Research

This dissertation contributes to the body of knowledge by using signal-flow graph theory to (1) to derive the non-coherent steady-state radiative transfer for stratified dielectrics with any number of layers, and (2) to provide executional clarity to graphically represent the iterative process that explains the coherent radiative transfer within multi-layered dielectrics. This work also provides the framework to realize such a non-coherent steady-state general-form radiative transfer model. To the best of the author's knowledge, this is the first time that these approaches have been used to explain the radiative transfer within multi-layered media with non-uniform temperature distributions.

6.3 Derivation of Non-Coherent and Coherent Radiative Transfer Models

The derivation of both a non-coherent and coherent radiative transfer model is presented. Innovative modeling techniques for each approach are applied and overviewed below.

6.3.1 A Non-Coherent Radiative Transfer Model Based on Signal-Flow Graph Theory

Signal-flow graph theory is used to derive the steady-state radiative transfer within a four-layer stratified, non-uniform temperature, dielectric medium. The presented approach offers an alternative, less complex, method to derive the steady-state brightness temperature as was derived in [28] for a two-layer medium. Signal-flow graph theory offers a straightforward way to apply the process from [28] to any number of layers.

www.manaraa.com

6.3.1.1 Brightness Temperature (T_B)

The brightness temperature of a multi-layered structure is defined as the weighted sum of all thermal emissions up to interface 1. Figure 3.1 shows a cross-section of a four-layer stratified medium with a continuous dielectric profile and non-uniform temperatures and thicknesses. Both the total brightness temperature and the brightness temperature contributions per layer are depicted in this figure. The brightness temperature just above interface 1 at normal incidence is equal to

$$\begin{aligned} T_B &= T_{B.1} + T_{B.2} + T_{B.3} + T_{B.4} \\ &= (T_{B.1UP} + T_{B.1DOWN}) + (T_{B.2UP} + T_{B.2DOWN}) + (T_{B.3UP} + T_{B.3DOWN}) + T_{B.4UP}. \end{aligned} \tag{6.17}$$

$T_{B.j}$ is the brightness temperature contribution originating from layer j which consists of both upward $T_{B.jUP}$ and downward $T_{B.jDOWN}$ brightness temperature contributions per layer. The last layer only has an upward brightness temperature contribution since the N-th layer thickness is assumed to be semi-infinite. Γ_{Bj} represents the Fresnel reflectivity for the corresponding boundary between layers j and j-1. The Fresnel reflectivity is given by

$$\Gamma_{Bj} = \left|\mathrm{R}_{Bj}\right|^2 = \left|\frac{Z_j - Z_{j-1}}{Z_j + Z_{j-1}}\right|^2, \tag{6.18}$$

with

$$Z_j = Z_o/\sqrt{\varepsilon_{rj}} \qquad \text{and} \qquad Z_o = 377\Omega, \tag{6.19}$$

where R_{Bj} is the field reflection coefficient at the boundary between layers j and j-1, Z_j is the impedance of layer j, Z_o is the impedance of free space, and ε_{rj} is the complex relative permittivity of layer j. The term j increments from 1...N, where N is the maximum layer number. T_{jUP} and T_{jDOWN} are the upward and downward emitted radiation originating from layer j, respectively. Both T_{jUP} and T_{jDOWN} are equal to

$$T_{jUP} = T_{jDOWN} = \begin{cases} \left(1 - L_{Pj}^{-1}\right) \cdot T_j & \text{for } j \le N-1 \\ T_j & \text{for } j = N \end{cases}, \tag{6.20}$$

www.manaraa.com

where L_{Pj} and T_j are the dielectric power loss factors and physical temperatures of layer j, respectively. The N-th layer temperature contribution is equal to T_j since the last layer thickness is semi-infinite ($1/L_{PN} = 0$). The dielectric power loss-factor is calculated by

$$L_{Pj} = e^{2\alpha_j d_j}, \tag{6.21}$$

with

$$\alpha_j = \frac{2\pi}{\lambda_0} \cdot \left| \Im\left[\sqrt{\varepsilon_{rj}}\right] \right|, \tag{6.22}$$

where d_j is the thickness of layer j, α_j is the attenuation constant of layer j, λ_0 is the free space wavelength, ε_{rj} is the complex relative permittivity of layer j and $\Im[\,]$ is the imaginary operator.

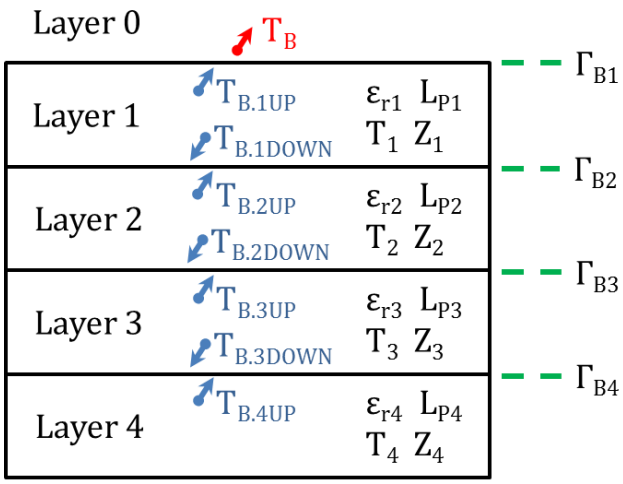

Figure 6.4 Cross-section of a four-layer stratified medium showing total brightness temperature T_B and individual layer brightness temperature contributions T_{Bj} for layers with temperature T_j, complex relative permittivity ε_{rj}, dielectric power loss-factor L_{Pj}, impedance Z_j, and the boundary reflectivity Γ_{Bj}.

6.3.1.2 Brightness Temperature (T_B) Derivation for a Four-Layer Medium Using Signal-Flow Graph Theory

The SFG model derived in this work is similar to the lossless, coherent SFG model found in [109], with the exception of this model being adapted for non-coherent emission and scattering formerly emphasized in [28]. The signal-flow graph (SFG) in Figure 6.5 models the entire thermal emissions incident on boundary 1 for the four-layer medium. Nodes in the signal-flow graph

www.manaraa.com

represent points in the medium at distances slightly above (to the left of boundary) or slightly below (to the right of boundary) the interface. The green dashed line represents a boundary between two media. T_{jUP} and T_{jDOWN} propagate left and right, respectively, in the SFG. Observing the SFG from left to right, the nodes sandwiching boundary 1 represent the transmitted (1- Γ_{B1}) and reflected (Γ_{B1}) portion at boundary 1. The portion transmitted through boundary 1 gets attenuated by L_{P1} (the power loss of layer 1) as it travels toward boundary 2. The portion reflected from interface 2 also gets attenuated by L_{P1} as it travels back toward boundary 1. These processes are repeated for each additional layer.

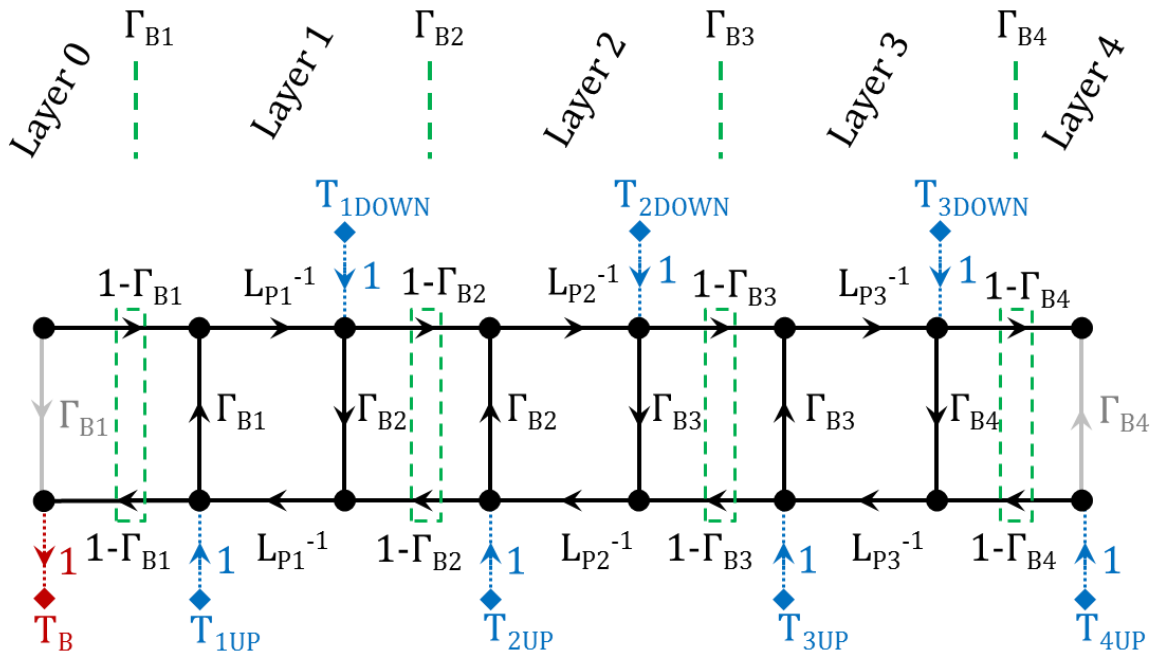

Figure 6.5 Signal-flow graph (SFG) of all emissions present within a four-layer medium with a continuous and non-uniform dielectric profile.

Appendix B describes the total gain from a source node to output node using Mason's signal-flow gain formula. Path gains are determined by following the traversed path originating from the layer of interest. The path gains for each layer contribution are

www.manaraa.com

$$G_{4U1} = T_{4UP} \cdot (1 - \Gamma_{B4}) \cdot \frac{1}{L_{P3}}(1 - \Gamma_{B3}) \cdot \frac{1}{L_{P2}}(1 - \Gamma_{B2}) \cdot \frac{1}{L_{P1}}(1 - \Gamma_{B1}),$$

$$G_{3U1} = T_{3UP} \cdot (1 - \Gamma_{B3}) \cdot \frac{1}{L_{P2}}(1 - \Gamma_{B2}) \cdot \frac{1}{L_{P1}}(1 - \Gamma_{B1}),$$

$$G_{3D1} = T_{3DOWN} \cdot \Gamma_{B4} \cdot \frac{1}{L_{P3}}(1 - \Gamma_{B3}) \cdot \frac{1}{L_{P2}}(1 - \Gamma_{B2}) \cdot \frac{1}{L_{P1}}(1 - \Gamma_{B1}),$$

$$G_{2U1} = T_{2UP} \cdot (1 - \Gamma_{B2}) \cdot \frac{1}{L_{P1}}(1 - \Gamma_{B1}),$$

$$G_{2D1} = T_{2DOWN} \cdot \Gamma_{B3} \cdot \frac{1}{L_{P2}}(1 - \Gamma_{B2}) \cdot \frac{1}{L_{P1}}(1 - \Gamma_{B1}),$$

$$G_{2D2} = T_{2DOWN} \cdot (1 - \Gamma_{B3}) \cdot \frac{1}{L_{P3}}\Gamma_{B4} \cdot \frac{1}{L_{P3}}(1 - \Gamma_{B3}) \cdot \frac{1}{L_{P2}} \cdot (1 - \Gamma_{B2}) \cdot \frac{1}{L_{P1}}(1 - \Gamma_{B1}),$$

$$G_{1U1} = T_{1UP} \cdot (1 - \Gamma_{B1}),$$

$$G_{1D1} = T_{1DOWN} \cdot \Gamma_{B2} \cdot \frac{1}{L_{P1}}(1 - \Gamma_{B1}),$$

$$G_{1D2} = T_{1DOWN} \cdot (1 - \Gamma_{B2}) \cdot \frac{1}{L_{P2}}\Gamma_{B3} \cdot \frac{1}{L_{P2}}(1 - \Gamma_{B2}) \cdot \frac{1}{L_{P1}}(1 - \Gamma_{B1}),$$

and

$$G_{1D3} = T_{1DOWN} \cdot (1 - \Gamma_{B2}) \cdot \frac{1}{L_{P2}}(1 - \Gamma_{B3}) \cdot \frac{1}{L_{P3}}\Gamma_{B4} \cdot \frac{1}{L_{P3}} \cdot (1 - \Gamma_{B3}) \cdot \frac{1}{L_{P2}}(1 - \Gamma_{B2}) \cdot \frac{1}{L_{P1}}(1 - \Gamma_{B1}), \quad (6.23)$$

where G_{jUk} is the k-th upward emitting path gain contribution from layer j and G_{jDk} is the k-th downward emitting path gain contribution from layer j.

All first order loops present for the four-layer case are

$$\mathrm{Loop}_1 = \frac{\Gamma_{B1}\Gamma_{B2}}{L_{P1}^2}$$

$$\mathrm{Loop}_2 = \frac{\Gamma_{B1} \cdot (1 - \Gamma_{B2})^2 \cdot \Gamma_{B3}}{(L_{P1}L_{P2})^2}$$

$$\mathrm{Loop}_3 = \frac{\Gamma_{B1} \cdot (1 - \Gamma_{B2})^2 \cdot (1 - \Gamma_{B3})^2 \cdot \Gamma_{B4}}{(L_{P1}L_{P2}L_{P3})^2}$$

$$\mathrm{Loop}_4 = \frac{\Gamma_{B2}\Gamma_{B3}}{L_{P2}^2}$$

$$\mathrm{Loop}_5 = \frac{\Gamma_{B2} \cdot (1 - \Gamma_{B3})^2 \cdot \Gamma_{B4}}{(L_{P2}L_{P3})^2}$$

and

$$\mathrm{Loop}_6 = \frac{\Gamma_{B3}\Gamma_{B4}}{L_{P3}^2}. \quad (6.24)$$

The second-order loops present for the four-layer case are

www.manaraa.com

$$\begin{aligned}
\text{Loop}_1 \cdot \text{Loop}_4 &= \frac{\Gamma_{B1}\Gamma_{B2}}{L_{P1}^2} \cdot \frac{\Gamma_{B2}\Gamma_{B3}}{L_{P2}^2} \\
\text{Loop}_1 \cdot \text{Loop}_5 &= \frac{\Gamma_{B1}\Gamma_{B2}}{L_{P1}^2} \cdot \frac{\Gamma_{B2} \cdot (1-\Gamma_{B3})^2 \cdot \Gamma_{B4}}{(L_{P2}L_{P3})^2} \\
\text{Loop}_1 \cdot \text{Loop}_6 &= \frac{\Gamma_{B1}\Gamma_{B2}}{L_{P1}^2} \cdot \frac{\Gamma_{B3}\Gamma_{B4}}{L_{P3}^2} \\
\text{Loop}_2 \cdot \text{Loop}_6 &= \frac{\Gamma_{B1} \cdot (1-\Gamma_{B2})^2 \cdot \Gamma_{B3}}{(L_{P1}L_{P2})^2} \cdot \frac{\Gamma_{B3}\Gamma_{B4}}{L_{P3}^2}
\end{aligned} \tag{6.25}$$

and

$$\text{Loop}_4 \cdot \text{Loop}_6 = \frac{\Gamma_{B2}\Gamma_{B3}}{L_{P2}^2} \cdot \frac{\Gamma_{B3}\Gamma_{B4}}{L_{P3}^2}.$$

The third-order loop present for the four-layer case is

$$\text{Loop}_1 \cdot \text{Loop}_4 \cdot \text{Loop}_6 = \frac{\Gamma_{B1}\Gamma_{B2}}{L_{P1}^2} \cdot \frac{\Gamma_{B2}\Gamma_{B3}}{L_{P2}^2} \cdot \frac{\Gamma_{B3}\Gamma_{B4}}{L_{P3}^2}. \tag{6.26}$$

The determinant of the SFG for the four-layer case is

$$\begin{aligned}
\Delta_{N.4} &= 1 - (\text{Loop}_1 + \text{Loop}_2 + \text{Loop}_3 + \text{Loop}_4 + \text{Loop}_5 + \text{Loop}_6) \\
&\quad + \begin{pmatrix} \text{Loop}_1 \cdot \text{Loop}_4 + \text{Loop}_1 \cdot \text{Loop}_5 + \text{Loop}_1 \cdot \text{Loop}_6 \cdots \\ +\text{Loop}_2 \cdot \text{Loop}_6 + \text{Loop}_4 \cdot \text{Loop}_6 \end{pmatrix} \\
&\quad - (\text{Loop}_1 \cdot \text{Loop}_4 \cdot \text{Loop}_6)
\end{aligned}$$

$$\begin{aligned}
&= 1 - \left(\begin{array}{c} \frac{\Gamma_{B1}\Gamma_{B2}}{L_{P1}^2} + \frac{\Gamma_{B1} \cdot (1-\Gamma_{B2})^2 \cdot \Gamma_{B3}}{(L_{P1}L_{P2})^2} + \frac{\Gamma_{B1}(1-\Gamma_{B2})^2(1-\Gamma_{B3})^2 \cdot \Gamma_{B4}}{(L_{P1}L_{P2}L_{P3})^2} \cdots \\ + \frac{\Gamma_{B2}\Gamma_{B3}}{L_{P2}^2} + \frac{\Gamma_{B2} \cdot (1-\Gamma_{B3})^2 \cdot \Gamma_{B4}}{(L_{P2}L_{P3})^2} + \frac{\Gamma_{B3}\Gamma_{B4}}{L_{P3}^2} \end{array} \right) \\
&\quad + \left(\begin{array}{c} \frac{\Gamma_{B1}\Gamma_{B2}}{L_{P1}^2} \cdot \frac{\Gamma_{B2}\Gamma_{B3}}{L_{P2}^2} + \frac{\Gamma_{B1}\Gamma_{B2}}{L_{P1}^2} \cdot \frac{\Gamma_{B2} \cdot (1-\Gamma_{B3})^2 \cdot \Gamma_{B4}}{(L_{P2}L_{P3})^2} + \frac{\Gamma_{B1}\Gamma_{B2}}{L_{P1}^2} \cdot \frac{\Gamma_{B3}\Gamma_{B4}}{L_{P3}^2} \cdots \\ + \frac{\Gamma_{B1} \cdot (1-\Gamma_{B2})^2 \cdot \Gamma_{B3}}{(L_{P1}L_{P2})^2} \cdot \frac{\Gamma_{B3}\Gamma_{B4}}{L_{P3}^2} + \frac{\Gamma_{B2}\Gamma_{B3}}{L_{P2}^2} \cdot \frac{\Gamma_{B3}\Gamma_{B4}}{L_{P3}^2} \end{array} \right) \\
&\quad - \left(\frac{\Gamma_{B1}\Gamma_{B2}}{L_{P1}^2} \cdot \frac{\Gamma_{B2}\Gamma_{B3}}{L_{P2}^2} \cdot \frac{\Gamma_{B3}\Gamma_{B4}}{L_{P3}^2} \right),
\end{aligned} \tag{6.27}$$

The resulting cofactors of the SFG for the four-layer case are

$$\begin{aligned}
\Delta_{1D3} = \Delta_{2D2} = \Delta_{3U1} = \Delta_{3D1} = \Delta_{4U1} &= 1 \\
\Delta_{1D2} = \Delta_{2U1} = \Delta_{2D1} &= 1 - \frac{\Gamma_{B3}\Gamma_{B4}}{L_{P3}^2} \\
\Delta_{1U1} = \Delta_{1D1} &= 1 - \left(\frac{\Gamma_{B2}\Gamma_{B3}}{L_{P2}^2} + \frac{\Gamma_{B2} \cdot (1-\Gamma_{B3})^2 \cdot \Gamma_{B4}}{(L_{P2}L_{P3})^2} + \frac{\Gamma_{B3}\Gamma_{B4}}{L_{P3}^2} \right) + \left(\frac{\Gamma_{B2}\Gamma_{B3}}{L_{P2}^2} \cdot \frac{\Gamma_{B3}\Gamma_{B4}}{L_{P3}^2} \right),
\end{aligned} \tag{6.28}$$

www.manaraa.com

where Δ_{jUk} is the k-th upward emitting cofactor from layer j and Δ_{jDk} is the k-th downward emitting cofactor from layer j. Applying Mason's signal-flow gain formula from Appendix A, the brightness temperature contributions per layer are

$$T_{B.1} = T_1 \cdot \left(1 - \frac{1}{L_{\mathrm{P1}}}\right)(1 - \Gamma_{\mathrm{B1}}) \cdot \Delta_{N.4}^{-1} \cdots$$
$$\cdot \left(\begin{array}{c} 1 \cdot \left[1 - \left(\frac{\Gamma_{\mathrm{B2}}\Gamma_{\mathrm{B3}}}{L_{\mathrm{P2}}^2} + \frac{\Gamma_{\mathrm{B3}}\Gamma_{\mathrm{B4}}}{L_{\mathrm{P3}}^2} + \frac{\Gamma_{\mathrm{B2}}\Gamma_{\mathrm{B4}}(1-\Gamma_{\mathrm{B3}})^2}{(L_{\mathrm{P2}}L_{\mathrm{P3}})^2}\right) + \left(\frac{\Gamma_{\mathrm{B2}}\Gamma_{\mathrm{B3}}}{\mathrm{L}_{\mathrm{P2}}^2} \cdot \frac{\Gamma_{\mathrm{B3}}\Gamma_{\mathrm{B4}}}{\mathrm{L}_{\mathrm{P3}}^2}\right) \right] \\ + \frac{\Gamma_{\mathrm{B2}}}{L_{\mathrm{P1}}} \cdot \left[1 - \left(\frac{\Gamma_{\mathrm{B2}}\Gamma_{\mathrm{B3}}}{L_{\mathrm{P2}}^2} + \frac{\Gamma_{\mathrm{B3}}\Gamma_{\mathrm{B4}}}{L_{\mathrm{P3}}^2} + \frac{\Gamma_{\mathrm{B2}}\Gamma_{\mathrm{B4}}(1-\Gamma_{\mathrm{B3}})^2}{(L_{\mathrm{P2}}L_{\mathrm{P3}})^2}\right) + \left(\frac{\Gamma_{\mathrm{B2}}\Gamma_{\mathrm{B3}}}{\mathrm{L}_{\mathrm{P2}}^2} \cdot \frac{\Gamma_{\mathrm{B3}}\Gamma_{\mathrm{B4}}}{\mathrm{L}_{\mathrm{P3}}^2}\right) \right] \\ + \frac{\Gamma_{\mathrm{B3}} \cdot (1-\Gamma_{\mathrm{B2}})^2}{L_{\mathrm{P1}}L_{\mathrm{P2}}^2} \cdot \left[1 - \frac{\Gamma_{\mathrm{B3}}\Gamma_{\mathrm{B4}}}{L_{\mathrm{P3}}^2}\right] + \frac{\Gamma_{\mathrm{B4}} \cdot (1-\Gamma_{\mathrm{B3}})^2 \cdot (1-\Gamma_{\mathrm{B2}})^2}{L_{\mathrm{P1}}L_{\mathrm{P2}}^2L_{\mathrm{P3}}^2} \end{array} \right)$$
$$= T_1 \cdot \epsilon_{ncoh.1} = T_1 \cdot (1 - \Gamma_{ncoh.1}) = T_{Beff.1} \cdot \left(1 - \Gamma_{ncoh.1}^{iso}\right)$$

$$T_{B.2} = T_2 \cdot \left(1 - \frac{1}{L_{\mathrm{P2}}}\right)(1 - \Gamma_{\mathrm{B2}})(1 - \Gamma_{\mathrm{B1}}) \cdot \frac{1}{L_{\mathrm{P1}}} \cdot \Delta_{N.4}^{-1} \cdots$$
$$\cdot \left(1 \cdot \left[1 - \frac{\Gamma_{\mathrm{B3}}\Gamma_{\mathrm{B4}}}{L_{\mathrm{P3}}^2}\right] + \frac{\Gamma_{\mathrm{B3}}}{L_{\mathrm{P2}}} \cdot \left[1 - \frac{\Gamma_{\mathrm{B3}}\Gamma_{\mathrm{B4}}}{L_{\mathrm{P3}}^2}\right] + \frac{\Gamma_{\mathrm{B4}} \cdot (1-\Gamma_{\mathrm{B3}})^2}{L_{\mathrm{P2}}L_{\mathrm{P3}}^2}\right)$$
$$= T_2 \cdot \epsilon_{ncoh.2} = T_2\,(1 - \Gamma_{ncoh.2}) = T_{Beff.2} \cdot \left(1 - \Gamma_{ncoh.2}^{iso}\right)$$

$$T_{B.3} = T_3 \cdot \left(1 - \frac{1}{L_{\mathrm{P3}}}\right) \cdot \left(1 + \frac{\Gamma_{\mathrm{B4}}}{L_{\mathrm{P3}}}\right)(1 - \Gamma_{\mathrm{B3}})(1 - \Gamma_{\mathrm{B2}})(1 - \Gamma_{\mathrm{B1}}) \cdot \frac{1}{L_{\mathrm{P1}}L_{\mathrm{P2}}} \cdot \Delta_{N.4}^{-1}$$
$$= T_3 \cdot \epsilon_{ncoh.3} = T_3\,(1 - \Gamma_{ncoh.3}) = T_{Beff.3} \cdot \left(1 - \Gamma_{ncoh.3}^{iso}\right)$$

and

$$T_{B.4} = T_4 \cdot (1 - \Gamma_{\mathrm{B4}})(1 - \Gamma_{\mathrm{B3}})(1 - \Gamma_{\mathrm{B2}})(1 - \Gamma_{\mathrm{B1}}) \cdot \frac{1}{L_{\mathrm{P1}}L_{\mathrm{P2}}L_{\mathrm{P3}}} \cdot \Delta_{N.4}^{-1}$$
$$= T_4 \cdot \epsilon_{ncoh.4} = T_4\,(1 - \Gamma_{ncoh.4}) = T_{Beff.4} \cdot \left(1 - \Gamma_{ncoh.4}^{iso}\right), \quad (6.29)$$

where $\epsilon_{ncoh.\mathrm{j}}$ is the non-coherent effective emissivity or the composite of the residual terms not including the physical temperature T_j, $\Gamma_{ncoh.\mathrm{j}}$ is the non-coherent effective reflectivity, $\Gamma_{ncoh.\mathrm{j}}^{iso}$ is the isothermal non-coherent effective reflectivity, and $T_{Beff.j}$ is the effective brightness temperature for a N-layer medium originating from layer j. The final brightness temperature equation is

$$T_B = T_{B.1} + T_{B.2} + T_{B.3} + T_{B.4}$$
$$= T_1 \cdot \epsilon_{ncoh.1} + T_2 \cdot \epsilon_{ncoh.2} + T_3 \cdot \epsilon_{ncoh.3} + T_4 \cdot \epsilon_{ncoh.4}$$
$$= T_1 \cdot (1 - \Gamma_{ncoh.1}) + T_2 \cdot (1 - \Gamma_{ncoh.2}) + T_3 \cdot (1 - \Gamma_{ncoh.3}) + T_4 \cdot (1 - \Gamma_{ncoh.4})$$
$$= T_{Beff.1} \cdot \left(1 - \Gamma_{ncoh.1}^{iso}\right) + T_{Beff.2} \cdot \left(1 - \Gamma_{ncoh.2}^{iso}\right) + T_{Beff.3} \cdot \left(1 - \Gamma_{ncoh.3}^{iso}\right) + T_{Beff.4}$$
$$\cdot \left(1 - \Gamma_{ncoh.4}^{iso}\right). \quad (6.30)$$

with the non-coherent effective brightness temperature given as

www.manaraa.com

$$T_{B,eff}^{[\mathrm{ncoh}]} = \frac{T_B}{1-\Gamma_{ncoh}^{\mathrm{iso}}} = \frac{\epsilon_{ncoh.1}T_1 + \epsilon_{ncoh.2}T_2 + \epsilon_{ncoh.3}T_3 + \epsilon_{ncoh.4}T_4}{1-\Gamma_{ncoh}^{\mathrm{iso}}} = \frac{1}{1-\Gamma_{ncoh}^{\mathrm{iso}}} \cdot \sum_{j=1}^{n} \epsilon_{ncoh.j} \cdot T_j \tag{6.31}$$

6.3.1.3 Apparent Temperature (T_{AP}) Signal-Flow Graph

The apparent temperature T_{AP} is comprised of both the brightness temperature and a portion of external radiation T_0 from medium 0 impinging on boundary 1 that gets scattered by the surface of medium 1 T_{SCAT}, as modeled in Figure 6.6(a). The corresponding apparent temperature SFG is shown in Figure 6.6(b). $T_{AP}(H)$ and $T_{AP}(0)$ are the apparent temperature (emission contributions from all layers at this point) at a height of H above and right at interface 1, respectively. The final apparent temperature transfer function is

$$T_{AP}(H) = T_{AP}(0) \cdot L_{\mathrm{P0}}^{-1}(H) + T_{0UP}, \tag{6.32}$$

with

$$\begin{aligned} T_{AP}(0) &= T_B + T_{SCAT} = (1-\Gamma_{ncoh}) \cdot T_0 + \Gamma_{ncoh}^{iso} \cdot T_{0DOWN} \\ &= \left(1-\Gamma_{ncoh}^{iso}\right) \cdot T_{B,eff}^{[\mathrm{ncoh}]} + \Gamma_{ncoh}^{iso} \cdot T_{0DOWN}. \end{aligned} \tag{6.33}$$

where Γ_{ncoh} is the non-coherent effective reflectivity and Γ_{ncoh}^{iso} is the isothermal non-coherent effective reflectivity.

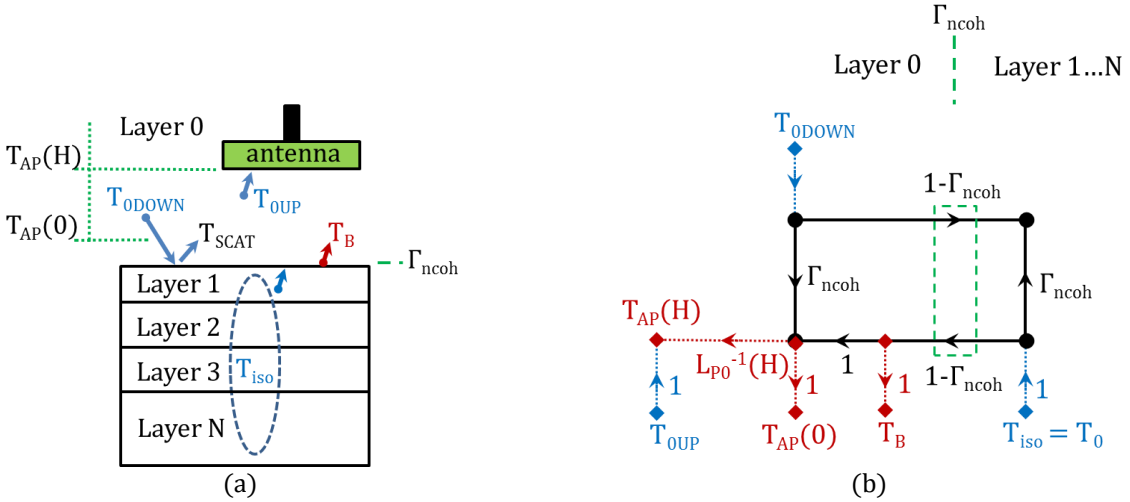

Figure 6.6 (a) Cross-section of a four-layer stratified medium depicting apparent temperature comprised of brightness temperature and scattered temperature. (b) Signal-flow graph (SFG) of apparent temperature.

www.manaraa.com

Using the apparent temperature relationship, it is shown that

$$T_B = (1 - \Gamma_{ncoh}) \cdot T_0. \tag{6.34}$$

Rearranging equation (6.34), it is seen that the non-coherent effective reflectivity for a four-layer medium is

$$\begin{aligned} \Gamma_{ncoh} &= 1 - \epsilon_{ncoh} = 1 - T_B/T_0 \\ &= 1 - (T_1 e_{ncoh.1} + T_2 e_{ncoh.2} + T_3 e_{ncoh.3} + T_4 e_{ncoh.4})/T_0, \end{aligned} \tag{6.35}$$

for the non-uniform temperature case and

$$\begin{aligned} \Gamma_{ncoh}^{iso} &= 1 - \epsilon_{ncoh}^{iso} \\ &= 1 - (\epsilon_{ncoh.1} + \epsilon_{ncoh.2} + \epsilon_{ncoh.3} + \epsilon_{ncoh.4}), \end{aligned} \tag{6.36}$$

for the isothermal case where $T_{iso} = T_0 = T_1 = T_2 = T_3 = T_4$, ϵ_{ncoh} is the non-coherent effective emissivity, and ϵ_{ncoh}^{iso} is the isothermal non-coherent effective emissivity.

6.3.2 A Coherent Radiative Transfer Model Based on Signal-Flow Graph Theory with a Generalized S-Parameter Matrix

The coherent radiative transfer within a four-layer stratified, non-uniform temperature, dielectric medium is derived using signal-flow graph theory. Signal-flow graph theory offers a graphical representation to apply the iterative process from [104] in a more visually clear manner. For a multi-layered medium with dissimilar dielectric constants, the reflection and transmission at each the boundary can be modeled with an impedance-transforming boundary scattering matrix. The boundary transforming scattering matrix is referenced to the specific impedance of each layer. Likewise, the transmission through each layer can also be modeled by a scattering matrix. Reference [109] implemented a similar impedance-transforming boundary scattering matrix for a lossless network. The lossless network makes for an ideal simplification, but does not apply when the reference impedance of the layers are complex. This work derives the reflection and transmission for the general case (*i.e.* within both lossy and lossless networks) by applying the conventions of power waves and generalized scattering parameters.

www.manaraa.com

6.3.2.1 Power Waves and Generalized Scattering Parameters

Power waves are used to analyze networks with complex reference impedances such that maximum power transfer is achieved between a source and load under complex conjugate match [30, 110-112] . Consider a two-port network in Figure 6.7 where the source and load impedance are both complex. The generalized power wave scattering parameters (S_p parameters), denoted by S_{p11}, S_{p12}, S_{p21}, S_{p22}, in terms of the incident and reflected power wave amplitudes are given by

$$\begin{aligned} b_{p1} &= S_{p11}a_{p1} + S_{p12}a_{p2} \\ b_{p2} &= S_{p21}a_{p1} + S_{p22}a_{p2}, \end{aligned} \tag{6.37}$$

where

$$\begin{aligned} a_{p1} &= \frac{V_1 + Z_1 I_1}{2\sqrt{\Re(Z_1)}} \\ a_{p2} &= \frac{V_2 + Z_2 I_2}{2\sqrt{\Re(Z_2)}} \\ b_{p1} &= \frac{V_1 - Z_1^* I_1}{2\sqrt{\Re(Z_1)}} \\ b_{p2} &= \frac{V_2 + Z_2^* I_2}{2\sqrt{\Re(Z_2)}}. \end{aligned} \tag{6.38}$$

Calculating the generalized power wave scattering parameters, the following relations are obtained

$$\begin{aligned} S_{p11} &= \left.\frac{b_{p1}}{a_{p1}}\right|_{a_{p2}=0} = \frac{Z_2 - Z_1^*}{Z_2 + Z_1} \\ S_{p21} &= \left.\frac{b_{p2}}{a_{p1}}\right|_{a_{p2}=0} = \frac{2\sqrt{\Re(Z_1)\cdot\Re(Z_2)}}{Z_2 + Z_1} \\ S_{p12} &= \left.\frac{b_{p1}}{a_{p2}}\right|_{a_{p1}=0} = \frac{2\sqrt{\Re(Z_1)\cdot\Re(Z_2)}}{Z_2 + Z_1} \\ S_{p22} &= \left.\frac{b_{p2}}{a_{p2}}\right|_{a_{p1}=0} = \frac{Z_1 - Z_2^*}{Z_1 + Z_2}. \end{aligned} \tag{6.39}$$

These generalized power wave scattering parameters characterize the impedance-transforming boundary scattering matrix.

www.manaraa.com

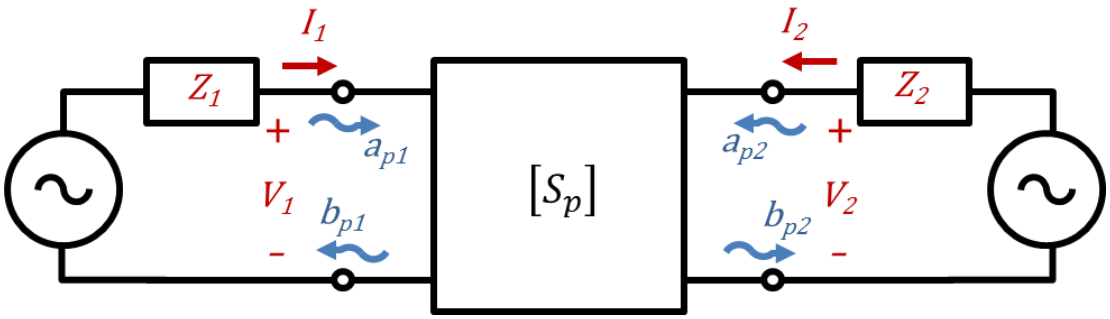

Figure 6.7 Two-port network for generalized power wave scattering parameters $[S_p]$ in terms of the incident and reflected power wave amplitudes.

6.3.2.2 Brightness Temperature (T_B) Derivation for a Four-Layer Medium Using Signal-Flow Graph Theory

The brightness temperature of a multi-layered medium is found using coherent emission and scattering principles. Figure 6.8 shows a signal-flow graph representation of a four-layer medium with a continuous dielectric profile and non-uniform layer temperatures. The power wave scattering matrix at each boundary $[S_B]^k$ is given by

$$\begin{aligned}[S_B]^k &= \begin{bmatrix} S^k_{B,11} & S^k_{B,12} \\ S^k_{B,21} & S^k_{B,22} \end{bmatrix} \\ &= \begin{bmatrix} R_{Bk} & \Psi_{Bk} \\ \Psi_{Bk} & R'_{Bk} \end{bmatrix} \\ &= \begin{bmatrix} \dfrac{Z_k - Z^*_{k-1}}{Z_k + Z_{k-1}} & \dfrac{2\sqrt{\Re(Z_{k-1})\cdot\Re(Z_k)}}{Z_k + Z_{k-1}} \\ \dfrac{2\sqrt{\Re(Z_{k-1})\cdot\Re(Z_k)}}{Z_k + Z_{k-1}} & \dfrac{Z_{k-1} - Z^*_k}{Z_{k-1} + Z_k} \end{bmatrix}. \end{aligned} \tag{6.40}$$

where R_{Bk} is the generalized power wave reflection coefficient at the kth boundary from the left side, R'_{Bk} is the generalized power wave reflection coefficient at the kth boundary from the right side, Ψ_{Bk} is the generalized power wave transmission coefficient at the kth boundary, and Z_k and Z_{k-1} are the impedances of the kth and k-1'st layer, respectively. Likewise, the scattering matrix through each layer $[S_L]^k$ is given by

www.manaraa.com

$$[S_L]^k = \begin{bmatrix} S_{L,11}^k & S_{L,12}^k \\ S_{L,21}^k & S_{L,22}^k \end{bmatrix} = \begin{bmatrix} 0 & \Psi_{Lk} \\ \Psi_{Lk} & 0 \end{bmatrix} = \begin{bmatrix} 0 & L_k^{-1} \\ L_k^{-1} & 0 \end{bmatrix}. \tag{6.41}$$

where Ψ_{Bk} is the generalized transmission coefficient at the kth boundary and L_k^{-1} is the dispersive loss-factor of the kth layer which is equal to $\exp(\alpha_k\ d_k)\cdot\exp(j\ \beta_k\ d_k)$. The scattering matrix representation for the SFG in Figure 6.8 indicating each boundary and layer is shown with

$$[S_{0,4}] = [S_B]^1 \leftrightarrow [S_L]^1 \leftrightarrow [S_B]^2 \leftrightarrow [S_L]^2 \leftrightarrow [S_B]^3 \leftrightarrow [S_L]^3 \leftrightarrow [S_B]^4. \tag{6.42}$$

The chain transfer-parameters (*i.e.* T-parameters [113]) provide useful relations for cascading individual scattering matrices. T-parameters $[T]^k$ can be calculated from either the boundary or layer S-parameters (herein denoted by $[S]^k \rightarrow [T]^k$) given the following relationship

$$[T]^k = \begin{bmatrix} T_{11}^k & T_{12}^k \\ T_{21}^k & T_{22}^k \end{bmatrix} = \begin{bmatrix} \frac{1}{S_{21}^k} & \frac{-S_{22}^k}{S_{21}^k} \\ \frac{S_{11}^k}{S_{21}^k} & \frac{S_{12}^k S_{21}^k - S_{11}^k S_{22}^k}{S_{21}^k} \end{bmatrix}. \tag{6.43}$$

The T-parameters can also be converted back into S-parameters (herein denoted by $[T]^k \rightarrow [S]^k$) with

$$[S]^k = \begin{bmatrix} S_{11}^k & S_{12}^k \\ S_{21}^k & S_{22}^k \end{bmatrix} = \begin{bmatrix} \frac{T_{21}^k}{T_{11}^k} & \frac{T_{11}^k T_{22}^k - T_{12}^k T_{21}^k}{T_{11}^k} \\ \frac{1}{T_{11}^k} & -\frac{T_{12}^k}{T_{11}^k} \end{bmatrix}. \tag{6.44}$$

Recalling the emissivity, transmissivity, and reflectivity conservation of energy relationship for a lossy two-layer, originally outlined in Section 2.2, it is well understood that $1 = \epsilon + \Gamma + \Upsilon$. Given these conservation of energy relationships, the emissivity of individual layers can be

www.manaraa.com

calculated if the full signal-flow graph in Figure 6.8 is broken into distinct two-layer scenarios. The iterative calculation of the emissivity for individual layers is outlined below.

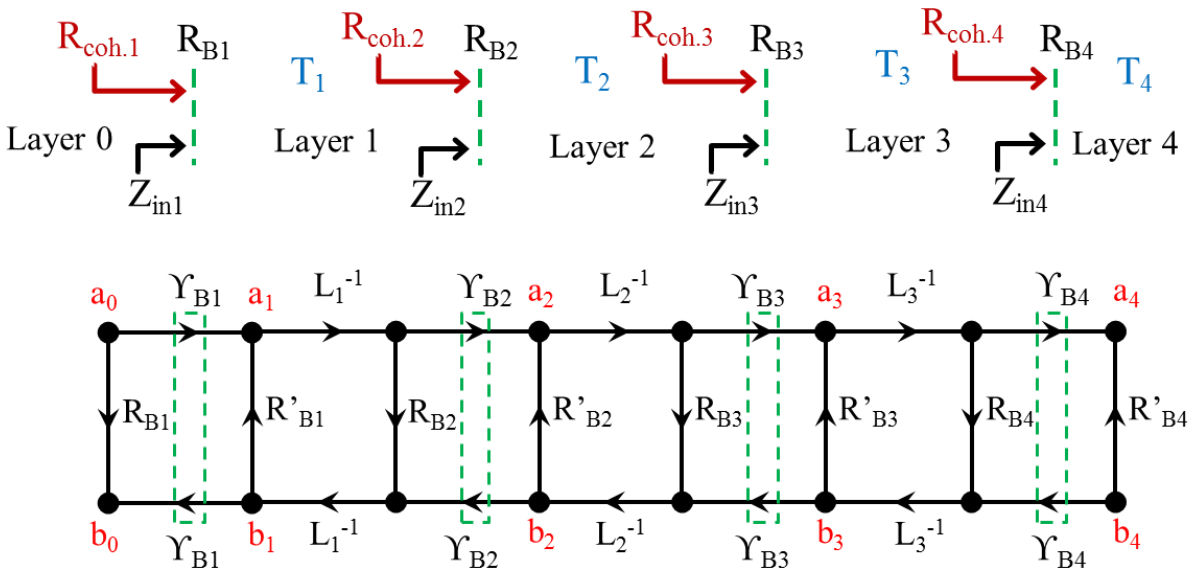

Figure 6.8 Signal-flow graph (SFG) of coherent radiative transfer present within a four-layer medium with a continuous dielectric profile and non-uniform temperatures.

The transmission from layer 0 to layer 4 $\Psi_{0,4}$ and the reflection from layer 0 to layer 0 $R_{0,0}$ can be depicted by Figure 6.9. The transfer matrix from layer 0 to layer 4 is calculated by

$$[T_{0,4}] = [T_B]^1 \cdot [T_L]^1 \cdot [T_B]^2 \cdot [T_L]^2 \cdot [T_B]^3 \cdot [T_L]^3 \cdot [T_B]^4. \tag{6.45}$$

Converting from $[T_{0,4}] \rightarrow [S_{0,4}]$, the following scattering matrix from layer 0 to layer 4 is obtained

$$[S_{0,4}] = \begin{bmatrix} R_{0,0} & \Psi_{0,4} \\ \Psi_{4,0} & R_{4,4} \end{bmatrix}. \tag{6.46}$$

The reflectivity from layer 0 to layer 0 $\Gamma_{0,0}$ and transmissivity from layer 0 to layer 4 $\Upsilon_{0,4}$ are found by

$$\begin{bmatrix} \Gamma_{0,0} & \Upsilon_{0,4} \\ \Upsilon_{4,0} & \Gamma_{4,4} \end{bmatrix} = \begin{bmatrix} |R_{0,0}|^2 & |\Psi_{0,4}|^2 \\ |\Psi_{4,0}|^2 & |R_{4,4}|^2 \end{bmatrix}. \tag{6.47}$$

The total emissivity resulting from layers 1/ 2/ 3 ϵ_{123} is found by

$$\epsilon_{123} = 1 - (\Gamma_{0,0} + \Upsilon_{0,4}). \tag{6.48}$$

www.manaraa.com

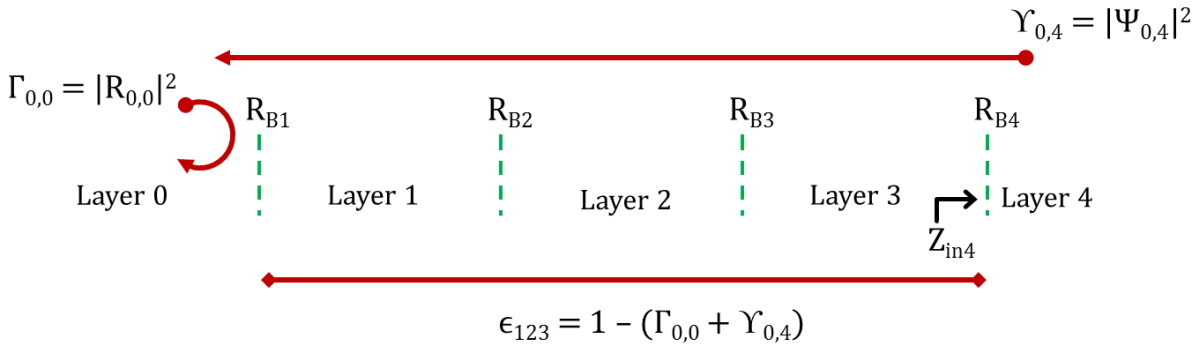

Figure 6.9 Transmission from layer 0 to layer 4 $\Psi_{0,4}$ and reflection from layer 0 to layer 0 $R_{0,0}$ related to the reflectivity from layer 0 to layer 0 $\Gamma_{0,0}$ and transmissivity from layer 0 to layer 4 $\Upsilon_{0,4}$.

The transmission from layer 0 to layers 2/3/4 $\Psi_{0,234}$ and the reflection from layer 0 to layer 0 $R_{0,0}$ can be depicted by Figure 6.10. The transfer matrix from layer 0 to layers 2/3/4 is found by

$$[T_{0,234}] = [T_B]^1 \cdot [T_L]^1 \cdot [T_B]^{234}. \tag{6.49}$$

Converting from $[T_{0,234}] \rightarrow [S_{0,234}]$, the following scattering matrix from layer 0 to layers 2/3/4 is obtained

$$[S_{0,234}] = \begin{bmatrix} R_{0,0} & \Psi_{0,234} \\ \Psi_{234,0} & R_{234,234} \end{bmatrix}. \tag{6.50}$$

The reflectivity from layer 0 to layer 0 Γ_{00} and the transmissivity from layer 0 to layers 2/3/4 $\Upsilon_{0,234}$ are found by

$$\begin{bmatrix} \Gamma_{0,0} & \Upsilon_{0,234} \\ \Upsilon_{234,0} & \Gamma_{234,234} \end{bmatrix} = \begin{bmatrix} |R_{0,0}|^2 & |\Psi_{0,234}|^2 \\ |\Psi_{234,0}|^2 & |R_{234,234}|^2 \end{bmatrix}. \tag{6.51}$$

The total emissivity resulting from layer 1 is found by

$$\epsilon_1 = 1 - (\Gamma_{0,0} + \Upsilon_{0,234}). \tag{6.52}$$

The boundary transforming transmission matrix is converted from the boundary transforming scattering matrix with $[T_B]^{234} \leftarrow [S_B]^{234}$. The boundary transforming scattering matrix from layer 1 to layers 2/3/4 $[S_B]^{234}$ is found by

$$[S_B]^{234} = \begin{bmatrix} R_{coh.2} & \Psi_{1,234} \\ \Psi_{234,1} & R'_{coh.2} \end{bmatrix}. \tag{6.53}$$

www.manaraa.com

The boundary reflection coefficient in terms of the input impedance Z_{in2} looking into layer 2 is found by

$$R_{coh.2} = \frac{Z_{in2} - Z_1^*}{Z_{in2} + Z_1}, \tag{6.54}$$

where the input impedance looking into layer 2 Z_{in2} is found with

$$Z_{in2} = Z_2 \left(\frac{1 + R_{234}}{1 - R_{234}}\right). \tag{6.55}$$

and the reflection looking into layers 2/3/4 just to the right of boundary 2 R_{234} is calculated with

$$\begin{gathered} [T_{234}] = [T_L]^2 \cdot [T_B]^3 \cdot [T_L]^3 \cdot [T_B]^4, \\ [S_{234}] \leftarrow [T_{234}], \\ [S_{234}] = \begin{bmatrix} R_{234} & - \\ - & - \end{bmatrix}. \end{gathered} \tag{6.56}$$

Similarly, the reflection coefficient in terms of the input impedance looking into layer 1 is

$$R'_{coh.2} = \frac{Z_1 - Z_{in2}^*}{Z_{in2} + Z_1}. \tag{6.57}$$

The transmission from layer 1 to layers 2/3/4 $\Psi_{234,1}$ or layers 2/3/4 to layer 1 $\Psi_{1,234}$ are found with

$$\Psi_{1,234} = \Psi_{234,1} = \frac{2\sqrt{\Re(Z_1) \cdot \Re(Z_{in2})}}{Z_{in2} + Z_1}. \tag{6.58}$$

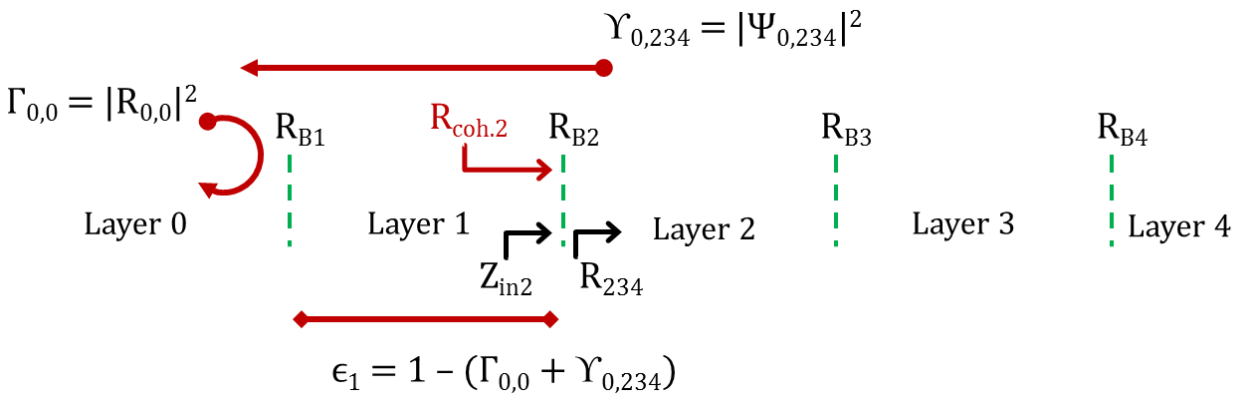

Figure 6.10 Transmission from layer 0 to layers 2/3/4 $\Psi_{0,234}$ and reflection from layer 0 to layer 0 $R_{0,0}$ related to the reflectivity from layer 0 to layer 0 $\Gamma_{0,0}$ and transmissivity from layer 0 to layers 2/3/4 $\Upsilon_{0,234}$.

www.manaraa.com

The reflection from layer 0 to layer 0 $R_{0,0}$ and the transmission from layer 0 to layers 3/4 $\Psi_{0,34}$ can be depicted by Figure 6.11. The transfer matrix from layer 0 to layers 3/4 is found by

$$[T_{0,34}] = [T_B]^1 \cdot [T_L]^1 \cdot [T_B]^2 \cdot [T_L]^2 \cdot [T_B]^{34}. \tag{6.59}$$

Converting from $[T_{0,34}] \rightarrow [S_{0,34}]$, the following scattering matrix from layer 0 to layers 3/4 is obtained

$$[S_{0,34}] = \begin{bmatrix} R_{0,0} & \Psi_{0,34} \\ \Psi_{34,0} & R_{34,34} \end{bmatrix}. \tag{6.60}$$

The reflectivity from layer 0 to layer 0 $\Gamma_{0,0}$ and the transmissivity from layer 0 to layers 3/4 $\Upsilon_{0,34}$ are found by

$$\begin{bmatrix} \Gamma_{0,0} & \Upsilon_{0,34} \\ \Upsilon_{34,0} & \Gamma_{34,34} \end{bmatrix} = \begin{bmatrix} |R_{0,0}|^2 & |\Psi_{0,34}|^2 \\ |\Psi_{34,0}|^2 & |R_{34,34}|^2 \end{bmatrix}. \tag{6.61}$$

The total emissivity resulting from layers 1 and 2 is calculated by

$$\epsilon_{12} = 1 - (\Gamma_{0,0} + \Upsilon_{0,34}). \tag{6.62}$$

The boundary transforming transmission matrix is converted from the boundary transforming scattering matrix with $[T_B]^{34} \leftarrow [S_B]^{34}$. The boundary transforming scattering matrix from layer 2 to layers 3/4 $[S_B]^{34}$ is found by

$$[S_B]^{34} = \begin{bmatrix} R_{coh.3} & \Psi_{2,34} \\ \Psi_{34,2} & R'_{coh.3} \end{bmatrix}. \tag{6.63}$$

The boundary reflection coefficient in terms of the input impedance looking into layer 2 is found by

$$R_{coh.3} = \frac{Z_{in3} - Z_2^*}{Z_{in3} + Z_2}, \tag{6.64}$$

where input impedance looking into layer 3 Z_{in3} is found with

$$Z_{in3} = Z_3\left(\frac{1 + R_{34}}{1 - R_{34}}\right), \tag{6.65}$$

and the reflection looking into layers 3/4 just to the right of boundary 3 R_{34} is calculated with

www.manaraa.com

$$\begin{gathered}[T_{34}] = [T_L]^3 \cdot [T_B]^4, \\ [S_{34}] \leftarrow [T_{34}], \\ [S_{34}] = \begin{bmatrix} R_{34} & - \\ - & - \end{bmatrix}.\end{gathered} \tag{6.66}$$

Similarly, the boundary reflection coefficient in terms of the input impedance looking into layer 3 is

$$R'_{coh.3} = \frac{Z_2 - Z_{in3}^*}{Z_{in3} + Z_2}, \tag{6.67}$$

The transmission from layer 2 to layers 3/4 $\Psi_{34,2}$ or layers 3/4 to layer 2 $\Psi_{2,34}$ are found with

$$\Psi_{2,34} = \Psi_{34,2} = \frac{2\sqrt{\Re(Z_2) \cdot \Re(Z_{in3})}}{Z_{in3} + Z_2}, \tag{6.68}$$

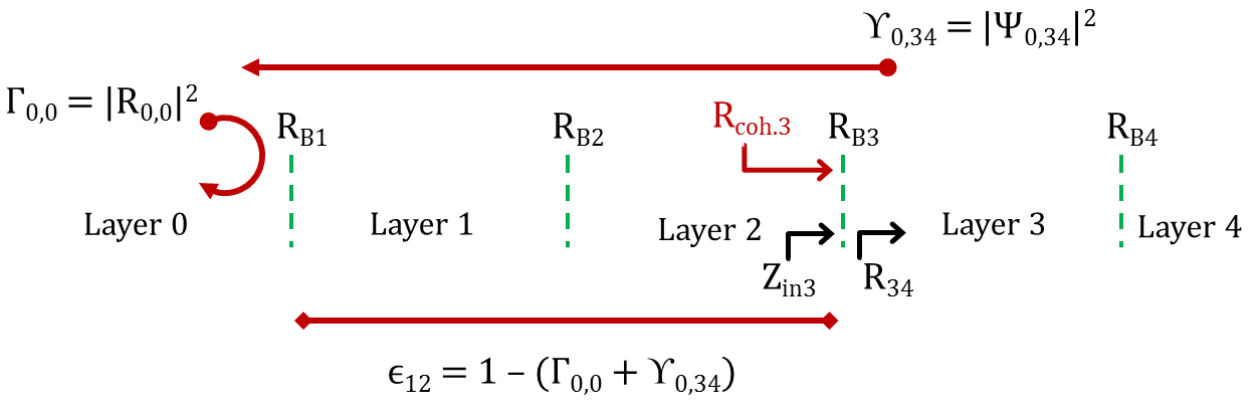

Figure 6.11 Transmission from layer 0 to layers 3/4 $\Psi_{0,34}$ and reflection from layer 0 to layer 0 $R_{0,0}$ related to the reflectivity from layer 0 to layer 0 $\Gamma_{0,0}$ and transmissivity from layer 0 to layers 3/4 $\Upsilon_{0,34}$.

The emissivity of each individual layer is given by

$$\begin{gathered}\epsilon_1 = 1 - (\Gamma_{0,0} + \Upsilon_{0,234}) \\ \epsilon_2 = \epsilon_{12} - \epsilon_1 \\ \epsilon_3 = \epsilon_{123} - \epsilon_{12} \\ \epsilon_4 = \Upsilon_{0,4}.\end{gathered} \tag{6.69}$$

The brightness temperature $T_B^{[\text{coh,pw}]}$ and the effective brightness temperature $T_{B,eff}^{[\text{coh,pw}]}$ using the coherent power wave formulation is

$$T_B^{[\text{coh,pw}]} = \epsilon_1 T_1 + \epsilon_2 T_2 + \epsilon_3 T_3 + \epsilon_4 T_4, \tag{6.70}$$

and

www.manaraa.com

$$T_{B,eff}^{[\mathrm{coh,pw}]} = \frac{\epsilon_1 T_1 + \epsilon_2 T_2 + \epsilon_3 T_3 + \epsilon_4 T_4}{1 - \Gamma_{iso.coh}^{[\mathrm{pw}]}} = \frac{1}{1 - \Gamma_{iso.coh}^{[\mathrm{pw}]}} \cdot \sum_{k=1}^{n} \epsilon_k T_k \tag{6.71}$$

where the isothermal coherent reflectivity using the power wave formulation is $\Gamma_{iso.coh}^{[\mathrm{pw}]} = \Gamma_{0,0}$. The apparent temperature at the surface of layer 1 using the coherent power wave formulation above can be calculated with

$$\begin{aligned} T_{AP}^{[\mathrm{coh,pw}]}(0) &= T_B^{[\mathrm{coh,pw}]} + T_0 \cdot \Gamma_{iso.coh}^{[\mathrm{pw}]}, \\ &= \left(1 - \Gamma_{iso.coh}^{[\mathrm{pw}]}\right) \cdot T_{B,eff}^{[\mathrm{coh,pw}]} + T_0 \cdot \Gamma_{iso.coh}^{[\mathrm{pw}]}. \end{aligned} \tag{6.72}$$

6.4 Validation of Coherent and Non-Coherent Scattering and Emission Models

Both the non-coherent and coherent scattering and emission models described in the previous section are validated using an HFSS plane-wave scattering simulation, a transmission-line coherent scattering model, or an iterative coherent scattering model developed by Wilheit.

The simplest multi-layered structure, depicted in Figure 6.12 is a medium that is vertically stratified into two dissimilar layers and bounded by an infinitely thick outer layer. The last stratified layer (Layer 2) also extends to infinity. The two-layer structure is used to explore the EM behavior of existing coherent and non-coherent scattering models.

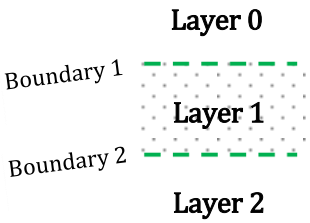

Figure 6.12 Cross-section for a two-layer stratified medium.

Ansys HFSS is used to compute the effective field reflection coefficient at boundary 1. The HFSS plane-wave scattering set-up is shown in Figure 6.13. A Floquet port is used to propagate a plane-wave toward the boundary of the structure. The last stratified layer is extended to infinite space by a matched boundary condition known as a perfectly matched layer (PML). The sides of the

www.manaraa.com

structure contain two pairs of Master and Slave boundary conditions, which model planes of infinite periodicity. This unit-cell modeling process can be repeated for any number of layers.

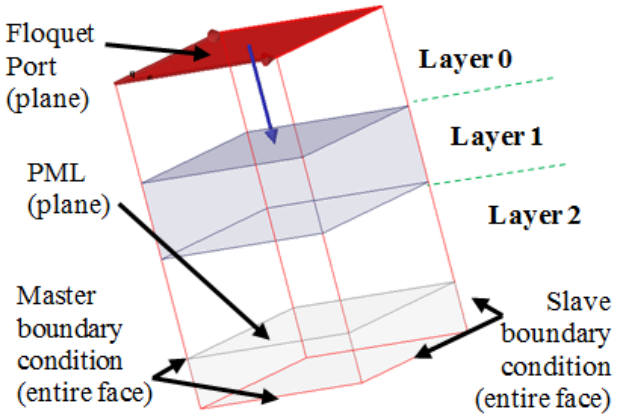

Figure 6.13 HFSS unit-cell scattering setup for a two-layer stratified medium with the applied boundary conditions and a Floquet port (de-embedded to the first boundary of the structure).

6.4.1 Non-Coherent Model Validation

The presented scattering models are compared for the basic two-layer scenario. The two-layer scenario consists of dielectrics where both layer 0 and layer 2 are air, and layer 1 is a lossy medium with similar dielectric properties to that of human skin. The relative permittivities of the stratified media are $\varepsilon_{r0} = \varepsilon_{r2} = 1$ and $\varepsilon_{r1} = 44.1 - j*12.1$ with a layer 1 thickness of 76.2 mm. Layer 0 and layer 2 have infinite thicknesses for the two-layer scenario. Figure 6.14 shows a comparison of the HFSS plane wave scattering simulation, the transmission line coherent scattering model, the Wilheit coherent scattering model, and the zeroth-order, first-order, second-order and steady-state non-coherent scattering formulations over a frequency range of 0.01 GHz to 3 GHz. All models are consistent with the findings from [106] in that they all follow similar decaying trends as they converge toward a constant steady-state value of Γ_1 as frequency approaches infinity. This two-layer scenario reaches a steady-state value quickly ($\leq$ 1.5 GHz) due to the thick and homogenous lossy material. The zeroth-order model for the two-layer scenario displays a constant value since the only reflection present is at boundary 1. The second-order model for this scenario resembles the first-order model since the only reflections present are at the boundaries 1 and 2; however the

www.manaraa.com

differences between the second-order and the first-order model become more obvious as more dissimilar stratified layers are introduced into the model.

The emission characteristics for the temperature dependent models (the Wilheit coherent model from equation (6.9), the zeroth-order non-coherent model from equation (6.13), the first-order non-coherent model from equation (6.14), the second-order non-coherent model from equation (6.15) and the steady-state non-coherent model from equation (6.16)) can be seen by observing Figure 6.15 where the effective brightness temperatures (T_{Beff}) from each model are shown when applying randomly selected physical temperatures of $T_0 = T_2 =$ 71.6°F (or 295.15K) to layer 0 and layer 2, and $T_1 =$ 104°F (or 313.15K) to layer 1. T_{Beff} obtained from the Wilheit and the first-order, second-order and steady-state non-coherent models all predict similar effective temperatures, but the zeroth-order non-coherent model deviates the most due to it not accounting for the higher-order reflections that are present within the stratified medium. The Wilheit coherent based T_{Beff} also exhibits an oscillatory variation with temperature as frequency increases. At lower frequencies the effects of both layers can be noticed (a combination of T_1 and T_2) in contrast to higher frequencies where mainly the layer 1 effects are seen. Apparent temperature values T_{AP} are also included in Figure 6.16. The first-order and second order model give similar temperature results, and all models underestimate the steady-state reflectivity up until the models reach a steady-state. The four-layer steady-state scattering formulation derived in this work is validated by splitting layer 1 of the two-layer scenario into three individual layers, as seen in Figure 6.17. Identical responses for all scattering models are obtained.

www.manaraa.com

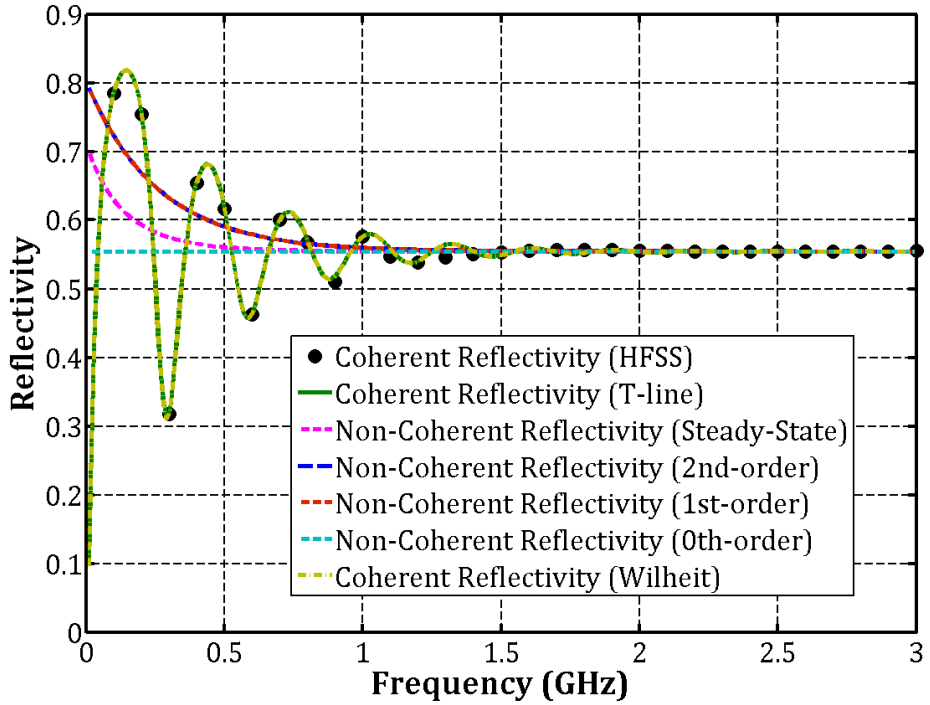

Figure 6.14 Comparison of reflectivity for Wilheit and the zeroth-order, first-order, second-order and steady-state non-coherent reflectivity formulation for the two-layer scenario.

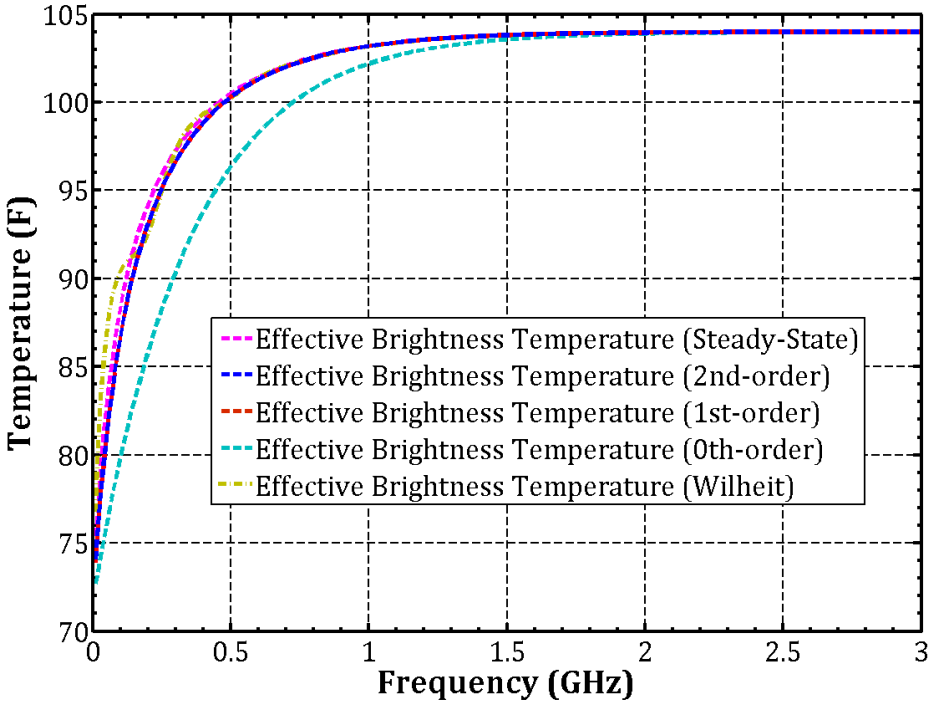

Figure 6.15 Comparison of effective brightness temperature for Wilheit and the zeroth-order, first-order, second-order and steady-state non-coherent effective brightness temperature formulation for the two-layer scenario.

www.manaraa.com

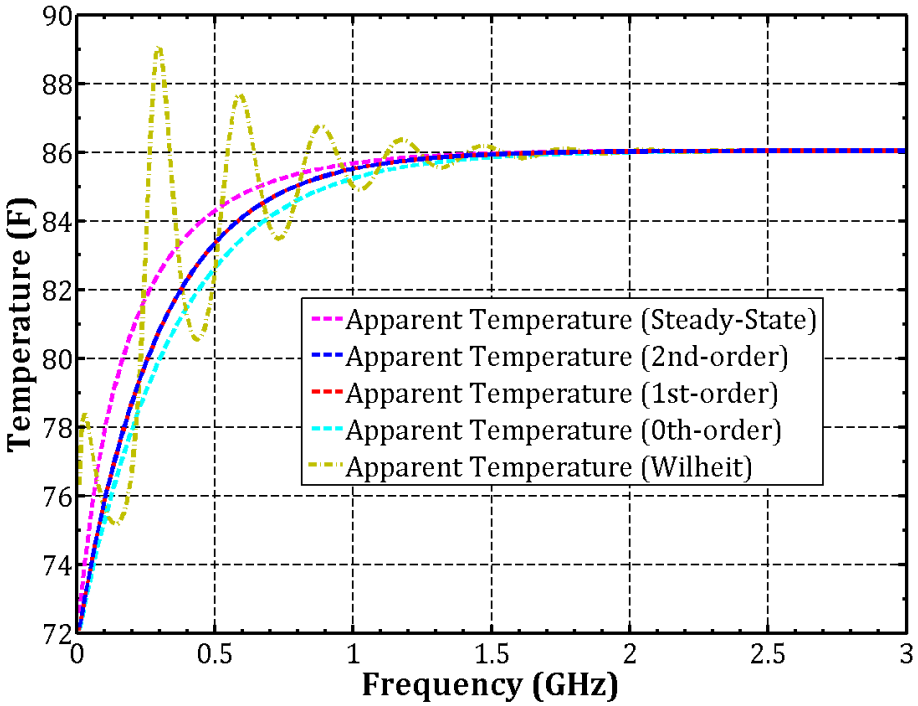

Figure 6.16 Comparison of apparent temperature for Wilheit and the zeroth-order, first-order, second-order and steady-state non-coherent apparent temperature formulation for the two-layer scenario.

Layer 0, $d_{2L.0} = \infty$
Layer 1, $d_{2L.1} = 76.2$mm
Layer 2, $d_{2L.2} = \infty$

Layer 0, $d_{4L.0} = \infty$
Layer 1, $d_{4L.1} = d_{2L.1}/3 = 25.4$mm
Layer 2, $d_{4L.2} = d_{2L.1}/3 = 25.4$mm
Layer 3, $d_{4L.3} = d_{2L.1}/3 = 25.4$mm
Layer 4, $d_{4L.4} = \infty$

Figure 6.17 Representation for two-layer medium being transformed into four-layers.

Now, consider the realistic four-layer human tissue scenario where layer 0 and layer 4 are air, layer 1 is skin, layer 2 is fat, and layer 3 is muscle. The frequency dependent permittivities for each layer are given in Figure 6.18. The tissue layer permittivities are taken from values measured from respective human tissue-mimicking phantoms. The thicknesses of layer 1, layer 2, and layer 3 are $d_1 = 3.3$ mm, $d_2 = 6.25$ mm, and $d_3 = 76.2$ mm, respectively. Layer 0 and layer 4 have infinite

www.manaraa.com

thicknesses for the four-layer scenario. These skin and fat layer thicknesses are chosen to illustrate potential values expected from a human body volume [114]. The effective reflectivity just above boundary 1 for this scenario is compared for the HFSS simulation, the t-line formulation, the Wilheit coherent scattering model, and the steady-state non-coherent formulation over a frequency range of 0.1 GHz to 18 GHz in Figure 6.19. Both the t-line and Wilheit scattering formulations predict similar results to the HFSS scattering simulation for the four-layer scenario (HFSS data goes up to 6 GHz), and the steady-state Γ^{iso}_{ncoh} captures the power decay behavior of the EM wave propagation, without the oscillatory phase-induced effects of the coherent approximations.

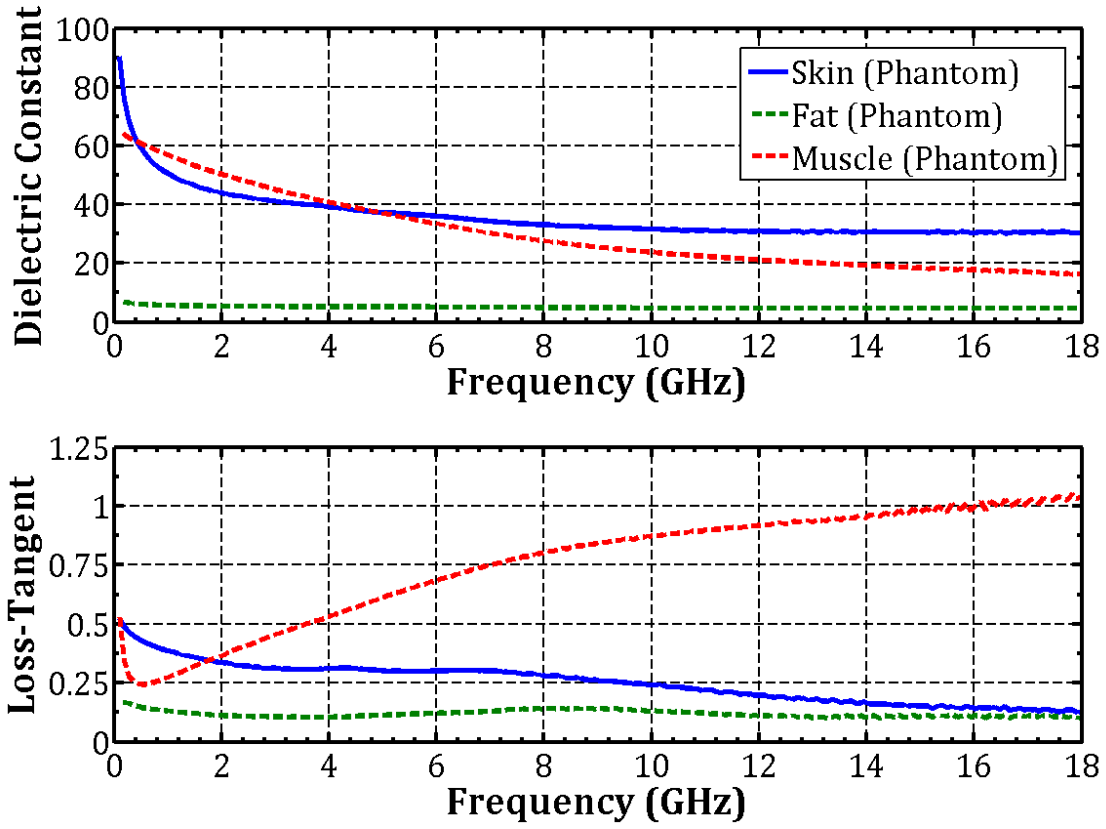

Figure 6.18 Dielectric constant and loss-tangent of phantom tissue layers.

Figure 6.19 also compares the isothermal coherent effective reflectivity to the isothermal non-coherent effective reflectivity calculated using the zeroth-order, first-order, second-order and steady-state effective reflectivity formulations. Both the first-order and second-order formulations overestimate the steady-state Γ^{iso}_{ncoh}, while the zeroth-order approximation underestimates the

www.manaraa.com

steady-state Γ^{iso}_{ncoh}. The effective brightness temperatures (T_{Beff}) obtained from each temperature dependent model given randomly selected input temperatures of $T_0 = T_4 = 71.6°F$ (or 295.15K) for layer 0 and layer 4, $T_1 = 111.2°F$ (or 317.15K) for layer 1, $T_2 = 190.4°F$ (or 361.15K) for layer 2, and $T_3 = 269.6°F$ (or 405.15K) for layer 3 is shown in Figure 6.20. T_{Beff} for the non-coherent models vary from the Wilheit coherent model due to the phase dependency of the Wilheit coherent model. The apparent temperature calculations (T_{AP}) are included in Figure 6.21. The zeroth order model overestimates the steady-state model while both the first and second-order model underestimates the steady state apparent temperature.

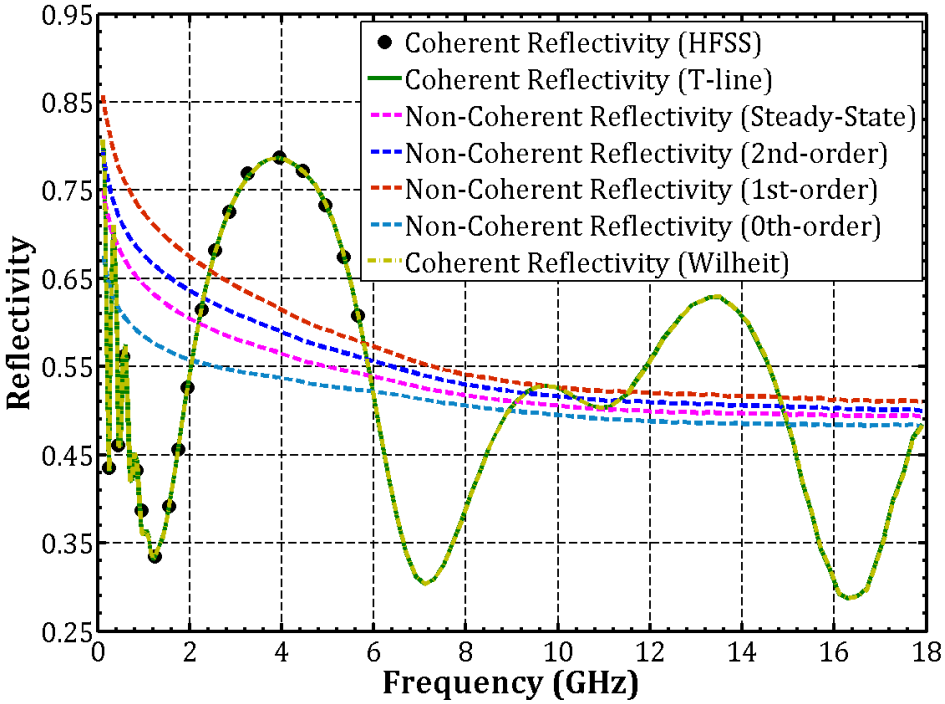

Figure 6.19 Comparison of coherent reflectivity (HFSS simulation, transmission-line, and Wilheit formulations) to the zeroth-order, first-order, and second-order non-coherent effective reflectivity formulations for the four-layer scenario.

www.manaraa.com

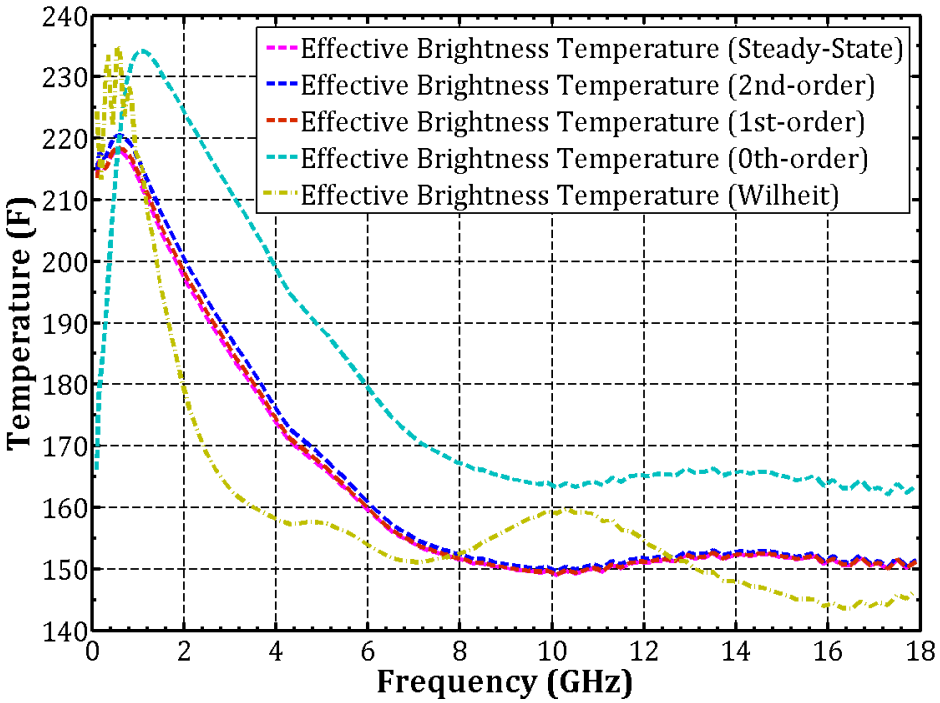

Figure 6.20 Comparison of effective brightness temperature for Wilheit coherent formulation to the zeroth-order, first-order, second-order, and steady-state non-coherent effective brightness temperature formulations for the four-layer scenario.

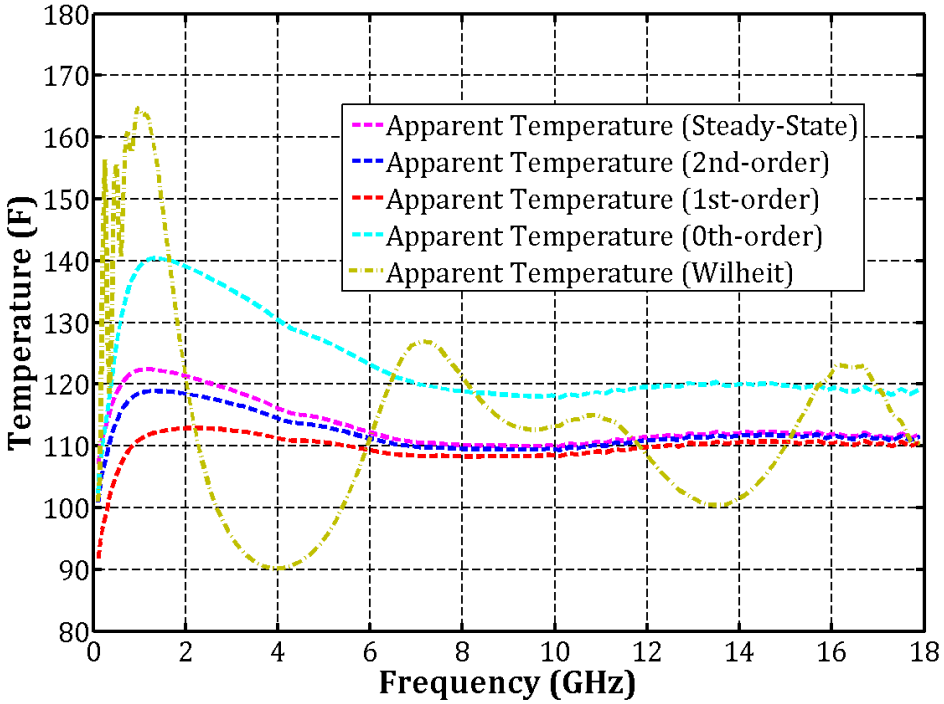

Figure 6.21 Comparison of apparent temperature for Wilheit coherent formulation to the zeroth-order, first-order, second-order, and steady-state non-coherent apparent temperature formulations for the four-layer scenario.

www.manaraa.com

6.4.2 Coherent Model Validation

The derived power wave coherent scattering model is compared to the HFSS plane wave coherent scattering simulation and the Wilheit coherent scattering model for the two-layer scenario (assuming physical temperatures of $T_0 = T_2 =$ 71.6°F (or 295.15K) for layer 0 and layer 2, and $T_1 =$ 104°F (or 313.15K) for layer 1) in Figure 6.22. The power wave coherent reflectivity formulation from equation (6.47) predicts a different reflectivity value than the HFSS and Wilheit coherent formulations. The difference in the predicted reflectivity value is due to the power wave formulation fundamentally being a tool for maximum power transfer [111] and it not satisfying the traveling wave normalized reflection coefficient of $(Z_{load}/Z_{ref} -1)/(Z_{load}/Z_{ref}+1)$ due to the power wave reflection coefficient being $(Z_{load}/Z_{ref} - Z_{ref}^*/Z_{ref})/(Z_{load}/Z_{ref}+1)$ [115] where Z_{load} is the load impedance, Z_{ref} is the reference impedance, and Z_{ref}^* is the complex conjugate of the reference impedance. The power wave formulation is however equal to the travelling wave formulation when the reference impedance is real [116]. Figure 6.23 and Figure 6.24 compares the effective brightness temperatures and apparent temperatures, respectively, for the Wilheit coherent formulation to the power wave coherent formulation for the two-layer scenario. The effective brightness temperature for power wave coherent formulation does not exhibit the same phase dependency that the Wilheit coherent formulation exhibits, but the phase dependency can be seen for both apparent temperature formulations. This apparent temperature phase dependency is due to the reflectivity formulations being ultimately derived from coherent processes. Figure 6.25, Figure 6.26, and Figure 6.27 show the coherent reflectivity, the effective brightness temperatures, and the apparent temperature, respectively, for the realistic four-layer human body scenario (assuming physical temperatures of $T_0 = T_4 =$ 71.6°F (or 295.15K) for layer 0 and layer 4, $T_1 =$ 111.2°F (or 317.15K) for layer 1, $T_2 =$ 190.4°F (or 361.15K) for layer 2, and $T_3 =$ 269.6°F (or 405.15K) for layer 3). Again, the reflectivity from the power wave solution is different from the Wilheit and HFSS reflectivity solution. The effective brightness temperature from the four-layer

www.manaraa.com

scenario displays erroneous results after 11 GHz so this portion of the data is omitted. This erroneous data is caused by the calculated emissivities for layer 3 and layer 4 exhibiting values above unity. The transmissivity, emissivity, and reflectivity unity summation relationships for scenarios with more than two-layers will have to be further investigated later.

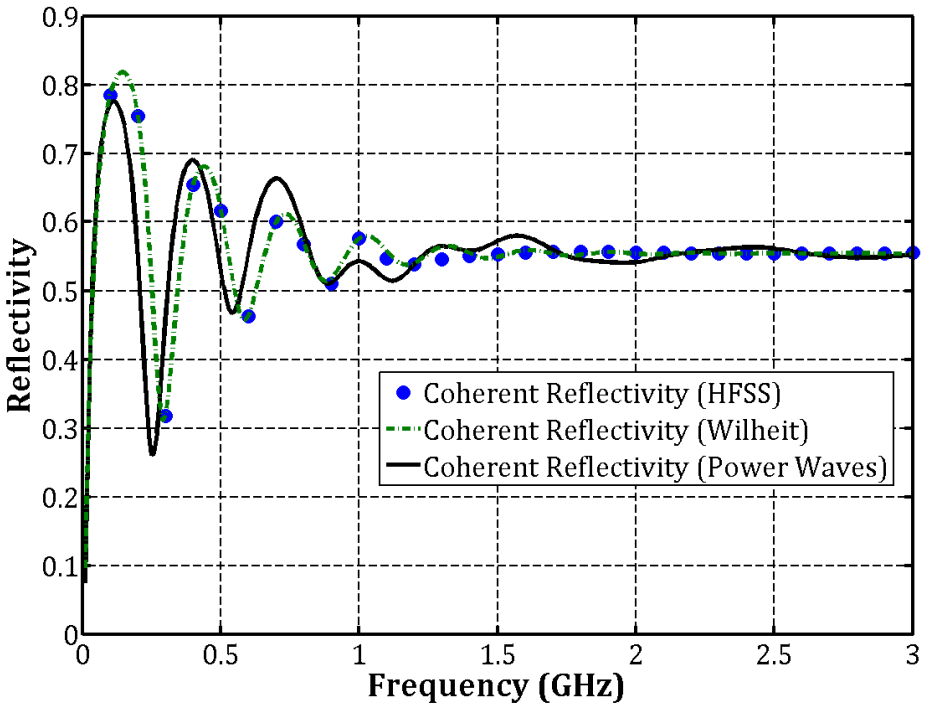

Figure 6.22 Comparison of the Wilheit and HFSS coherent reflectivity formulation to the power wave coherent reflectivity formulation for the two-layer scenario.

www.manaraa.com

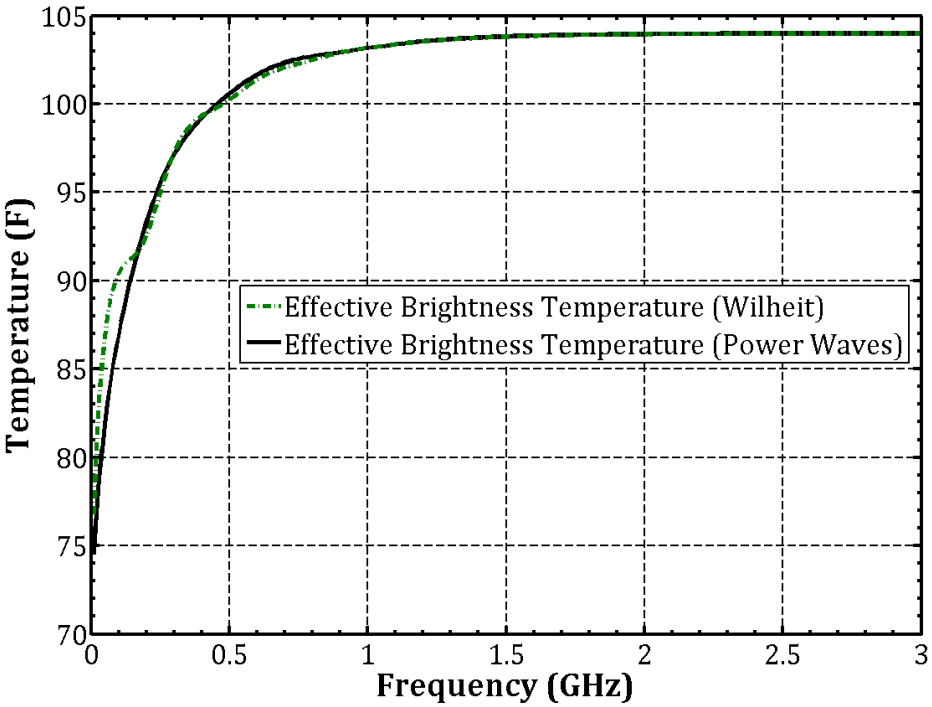

Figure 6.23 Comparison of effective brightness temperatures for Wilheit coherent formulation to the power wave coherent formulation for the two-layer scenario.

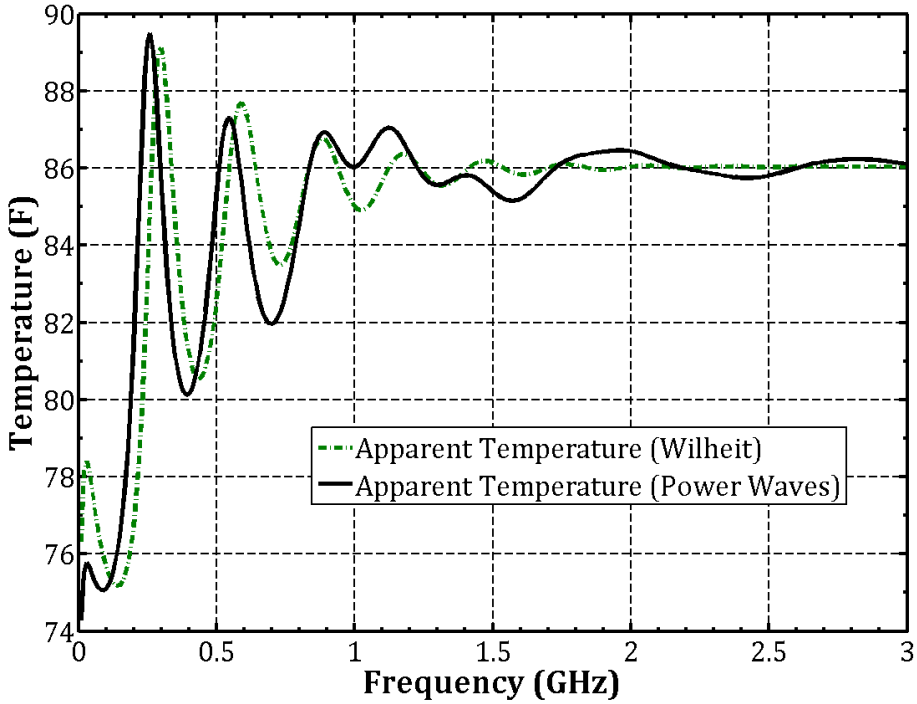

Figure 6.24 Comparison of apparent temperatures for Wilheit coherent formulation to the power wave coherent formulation for the two-layer scenario.

www.manaraa.com

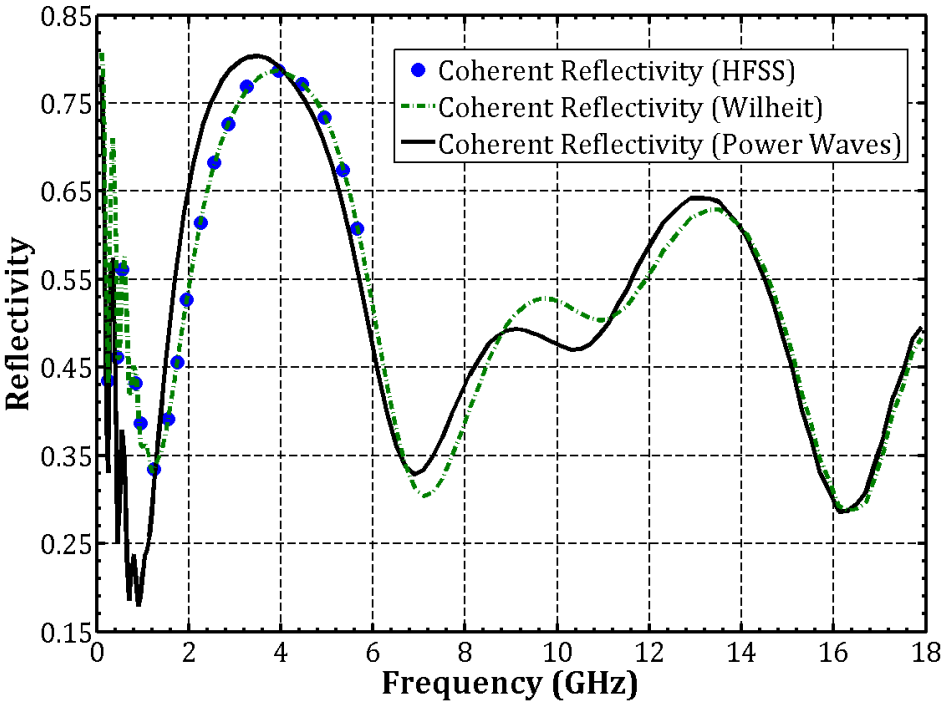

Figure 6.25 Comparison of the Wilheit and HFSS coherent reflectivity formulation to the power wave coherent reflectivity formulation for the four-layer scenario.

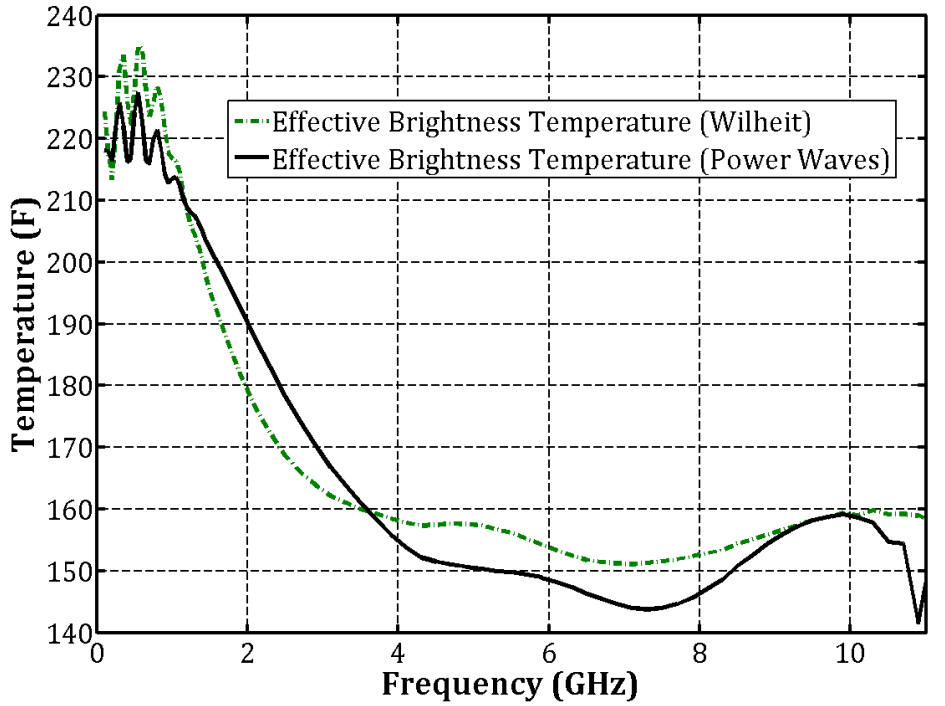

Figure 6.26 Comparison of effective brightness temperatures for Wilheit coherent formulation to the power wave coherent formulation for the four-layer scenario.

www.manaraa.com

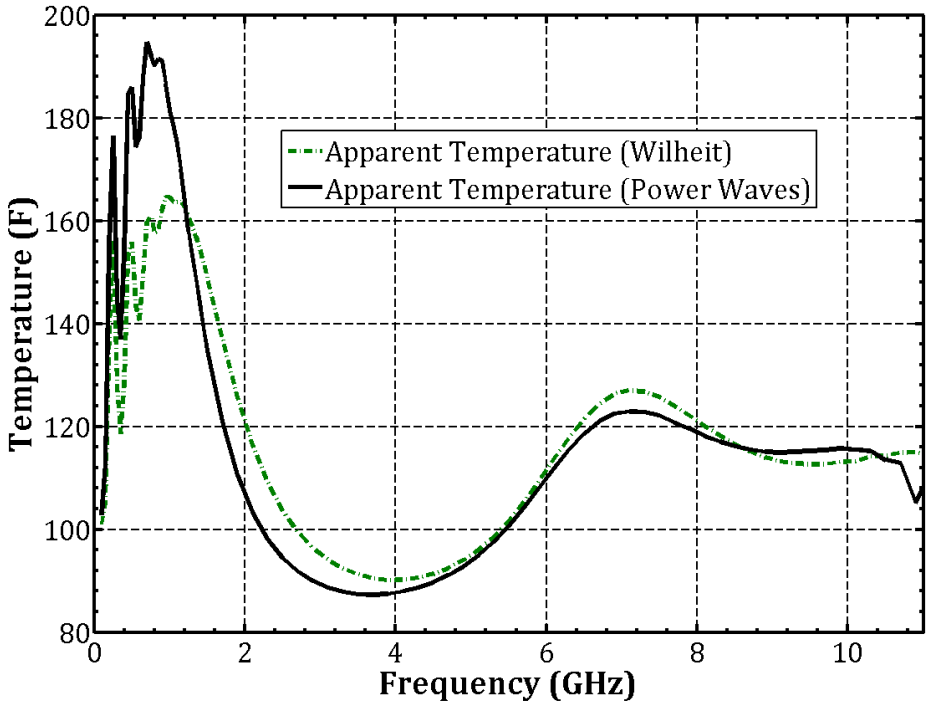

Figure 6.27 Comparison of apparent temperatures for Wilheit coherent formulation to the power wave coherent formulation for the four-layer scenario.

6.5 Conclusion

Signal-flow graph theory is used to explain both the coherent and non-coherent radiative transfer within multi-layer media. Effective reflectivity and effective brightness temperatures obtained from using existing coherent and non-coherent scattering formulations are compared to the derived models for both two-layer and four-layer structures. The power wave coherent solution does not predict the same reflectivity as both the Wilheit and HFSS coherent solutions. A pseudo wave coherent modeling approach [111, 116, 117] is needed to obtain similar reflection properties as the Wilheit and HFSS coherent solutions. Also, the derived four-layer power wave coherent solution does not predict a unity summation for the transmissivity, emissivity, and reflectivity combination at all frequencies. The power wave derivation needs to be further explored.

www.manaraa.com

Chapter 7 Experimental Validation of Internal Body Temperature Sensing with a Comprehensive Closed-Form Analytical Radiometric Model

7.1 Introduction

Since radiometric thermometry is an entirely passive sensing technique, all of the electromagnetic behaviors of a microwave thermometer ecosystem (*i.e.* the sensor and human tissues) must be modeled. Most available radiometric models only provide system modeling advanced enough to resolve relative internal body temperature. This chapter presents the outcome of a comprehensive closed-form analytical radiometric model in resolving internal body temperature. Subsurface muscle temperature is detected to within 1% from a microwave radiometric phantom testbed.

This chapter experimentally validates a comprehensive closed-form analytical radiometric model based on both a coherent and non-coherent brightness temperature model. Section 7.2 highlights previous microwave radiometric works involving internal body temperature sensing. Section 7.3 overviews the full closed-form comprehensive radiometric model. Section 7.4 highlights the experimental validation of both the coherent and non-coherent effective brightness temperature models. This chapter concludes with Section 7.5.

7.2 Previous Microwave Radiometric Works Involving Internal Body Temperature Sensing

An overview of many instances in which microwave radiometry is used for biomedical applications is provided in Section 2.3. This section highlights three specific examples of recent radiometric modeling used to facilitate internal body radiometric sensing. In [23, 24], a Dicke radiometer is used to monitor internal brain temperature for a phantom testbed validation setup and during a surgical procedure. The phantom testbed consists of a human skull encasing with a

www.manaraa.com

brain tissue equivalent circulating liquid. The calibration equation is referenced to the Dicke radiometer configuration. Both the antenna modeling and the radiative transfer modeling are accounted for with simulation software (by an HFSS specific absorption rate (SAR) simulation). Internal brain temperature was quoted to be tracked with a microwave radiometer to within 0.5°C and below over a 4.6 hour experiment. Likewise, during the 2-hour surgery the radiometer was able to track the internal brain temperature of the patient with a 1-4°C temperature difference. In [13, 14], a total power radiometer is used to monitor internal body core temperature for a phantom testbed validation setup. The phantom testbed consists of a hybrid skin/muscle solid tissue phantom and a liquid bloody-fat tissue phantom. The total power radiometer calibration equation assumes constant mismatches and constant switch path losses. The antenna modeling is simulated with an HFSS simulation. While the radiative transfer modeling is derived for a closed-form abbreviated 3–layer model accurately representing the hybrid phantom used during the study. Core body temperature was tracked to within 1.5-3% of the measured thermocouple probed phantom temperatures. In [12], a Dicke radiometer is used to monitor internal body core temperature for a phantom testbed validation setup. The phantom consists of a water, glass, water phantom. The antenna modeling and the radiative transfer modeling are accounted for with simulation software (by an HFSS specific absorption rate (SAR) simulation). Internal body temperature is extracted with a 2°C error.

7.2.1 Gap in Literature

Of the available microwave radiometry works for biomedical sensing, most provide radiometric models only sophisticated enough to resolve relative internal body temperature [12-14, 23, 24]. No current works give a closed-form analytical model with enough accuracy to provide a credible prediction of absolute internal body temperature. Up until this point, the available MW radiometric models either (1) give radiometric formulations calculated from computer-aided simulation software which would only work for relative temperature measurements [12, 23, 24] or

www.manaraa.com

(2) give closed-form analytical radiometric formulations which lack the required detail to achieve high accuracy absolute temperature monitoring [13, 14]. The next logical step is to realize a more comprehensive closed-form analytical radiometric model that is capable of resolving temperature to within 0.2°C.

7.2.2 Contribution of Research

This dissertation introduces new modeling techniques that leverage from existing works in order to develop a more comprehensive closed-form analytical radiometric model that will allow for the accurate sensing of internal body absolute temperature.

7.3 Closed-Form Comprehensive Radiometric Model

The closed-form comprehensive radiometric model is used to extract an internal body temperature from a stratified human tissue phantom testbed. The complete closed-form comprehensive radiometric model outlined in Figure 7.1 consists of the combination of paths A, B, and C. Path A consists of the correction from the radiometer output to antenna input (*i.e.* the correction for dissimilar path losses through the switch and cables), as is highlighted in Section 2.2.4 and Section 3.3. The correction from the radiometer output to antenna input, taken from equation (3.13), gives the unknown antenna noise temperature with

$$\begin{aligned} T_{Ant}^{meas} &= T_C + (T_H - T_C) \cdot \frac{\alpha_h}{\alpha_{ant}} \cdot \frac{P_{ant}^{del} - P_c^{del}}{P_h^{del} - P_c^{del}} \\ &= T_C + (T_H - T_C) \cdot \frac{\alpha_h}{\alpha_{ant}} \cdot \frac{Y_{ant} - 1}{Y_h - 1} \end{aligned} \tag{7.1}$$

where T_{Ant}^{meas} is the measured noise temperature for the scene observed by the antenna, T_H is the noise temperature for the hot calibration reference source, T_C is the noise temperature for the cold calibration reference source, α_h is the available power ratio when the switch is connected to the hot source, α_{ant} is the available power ratio when the switch is connected to the antenna port, Y_{ant} is the antenna Y-factor which is the ratio of the antenna delivered noise power to the cold source

www.manaraa.com

delivered noise power P_{ant}^{del}/P_c^{del}, and Y_h is the hot load Y-factor which is the ratio of the hot source delivered noise power to the cold source delivered noise power P_h^{del}/P_c^{del}.

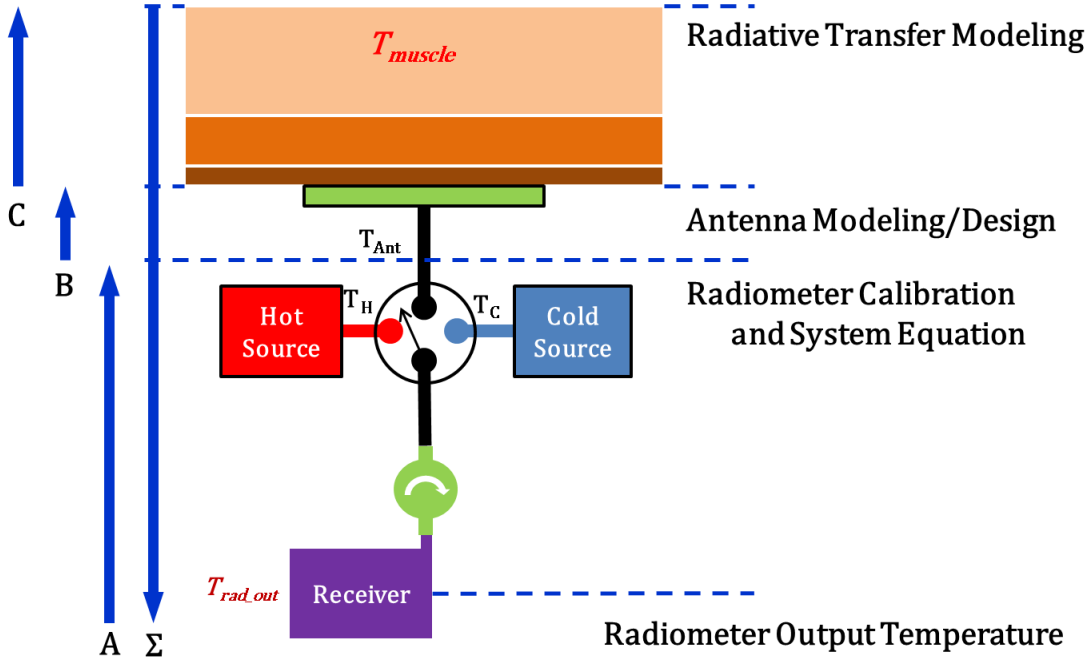

Figure 7.1 Closed-form comprehensive radiometric model.

The antenna noise temperature obtained by the Path A correction is input into the Path B correction, the correction at the antenna to body interface. The correction at the antenna to body interface (*i.e.* the correction for the antenna radiation and main-beam efficiencies) is originally highlighted in equation (2.15) from Section 2.2.2. Solving for the apparent brightness temperature calculated from the measured antenna noise temperature T_{AP}^{calc} gives

$$T_{AP}^{calc} = T_{ML} = \frac{1}{\eta_{rad}\eta_{ML}} T_{Ant}^{meas} - \frac{\eta_{rad}(1-\eta_{ML})}{\eta_{rad}\eta_{ML}} T_a - \frac{(1-\eta_{rad})}{\eta_{rad}\eta_{ML}} T_p. \tag{7.2}$$

where T_{ML} is the main-lobe temperature contribution which is equivalent to the apparent temperature of the scene, T_{Ant}^{meas} is the measured antenna noise temperature given from equations (3.13) and (7.1), η_{ML} is the antenna main-beam efficiency, η_{rad} is the antenna radiation efficiency, T_p is the physical temperature of the antenna, and T_a is the ambient temperature side-

www.manaraa.com

lobe contribution. The apparent temperature calculated from Path B (from equation (7.2)) is equated to the apparent temperature calculated from Path C (*i.e.* the correction down to the layer of interest) and the relation between the measured antenna noise temperature T_{Ant} and the subsurface detected muscle temperature $T_{muscle} = T_3$ can be formed. The apparent brightness temperature modeled from Path C, T_{AP}^{RTM}, initially highlighted in either equation (6.33) or (6.72) from Section 6.3, is given by

$$T_{AP}^{RTM} = T_B + \Gamma_{iso} \cdot T_0 = \epsilon_1 T_1 + \epsilon_2 T_2 + \epsilon_3 T_3 + \epsilon_4 T_4 + \Gamma_{iso} \cdot T_0 = \Gamma_{iso} \cdot T_0 + \sum_{k=1}^{n} \epsilon_k T_k \tag{7.3}$$

where T_k and ϵ_k are the physical temperature and emissivity of each stratified layer, Γ_{iso} is the isothermal reflectivity (which can be either non-coherent (6.33) or coherent (6.72)), and the superscript 'RTM' stands for Radiative Transfer Model (RTM). The quantities T_{AP}^{calc} and T_{AP}^{RTM} must be equal in order to solve for the absolute value of a buried temperature as measured by way of a microwave radiometer. The subsurface muscle temperature for the four-layer scenario is given by

$$T_{muscle} = T_3 = \frac{\frac{1}{\eta_{rad}\eta_{ML}} T_{Ant}^{meas} - \frac{\eta_{rad}(1-\eta_{ML})}{\eta_{rad}\eta_{ML}} T_a - \frac{(1-\eta_{rad})}{\eta_{rad}\eta_{ML}} T_p - \Gamma_{iso} \cdot T_0 - (\epsilon_1 T_1 + \epsilon_2 T_2 + \epsilon_4 T_4)}{\epsilon_3} \tag{7.4}$$

7.4 Experimental Validation of the Coherent and Non-Coherent Brightness Temperature Models

The four-layer coherent and non-coherent steady-state apparent brightness temperature formulations described in Chapter 6 are validated with a comparison to the extracted antenna temperature detected by the microwave radiometer. An antenna connected to the microwave radiometer is placed in contact with a four-layer human body tissue mimicking phantom testbed. Figure 7.2 shows the measurement set-up of the full system. Layered tissue mimicking phantoms consisting of a liquid muscle phantom and semi-solid skin and fat phantoms are highlighted in Chapter 4. Dielectric properties of the tissue mimicking phantoms are illustrated in Figure 7.3. A polyethylene (PE) spacer layer with a 0.0254 mm thickness is inserted between the antenna conductor and the surface of the skin phantom. The muscle phantom is heated and placed in contact

www.manaraa.com

with both the fat and skin phantom. Physical temperature changes of the layered tissue phantoms are tracked over time with a data-logger thermometer. Thermocouple probes connected to the data-logger thermometer are placed at the following locations: (P1) in the ambient environment, (P2) on the back side of the antenna, (P3) at the PE-skin interface, (P4) at the skin-fat interface, (P5) at the fat-muscle interface, (P6) at a distance in the middle of the muscle phantom, and (P7) in the heat and cooled air above the muscle phantom. Figure 7.4 displays the temperature values of the thermocouple probed temperatures (originally highlighted in Figure 7.2). The ambient air layer physical temperature is given from probe (P1). The antenna physical temperature is given by subtracting the temperatures from probes (P3)-(P2). The skin layer physical temperature is found by subtracting the temperatures from probes (P4)-(P3). The fat layer physical temperature is found by subtracting the temperatures from probes (P5)-(P4). The muscle layer physical temperature is given from probe (P6). The heated and cooled air layer physical temperature is given from probe (P7). Lastly, the aforementioned individual layer physical temperatures tracked over 48 hours are shown in Figure 7.5. The physical temperatures of all phantom layers initially heat up, then cool down to ambient temperature at approximately the same rate after coming to thermal equilibrium.

Experimental temperature data from the heated tissue phantom testbed is extracted with the radiometer. The radiometer has a center frequency at 1.4 GHz with 100 MHz of bandwidth and ~100 dB of system gain. The radiometer system is previously designed in another work, thus the radiometer design is not discussed in detail within this current work. More detail on the radiometer is given in [73]. The extracted radiometric antenna temperature for both the smoothed and unsmoothed (raw) data is given in Figure 7.6. A Hodrick-Prescott filter, with a smoothing parameter of $1x10^{10}$, is employed to smooth the extracted radiometric data.

www.manaraa.com

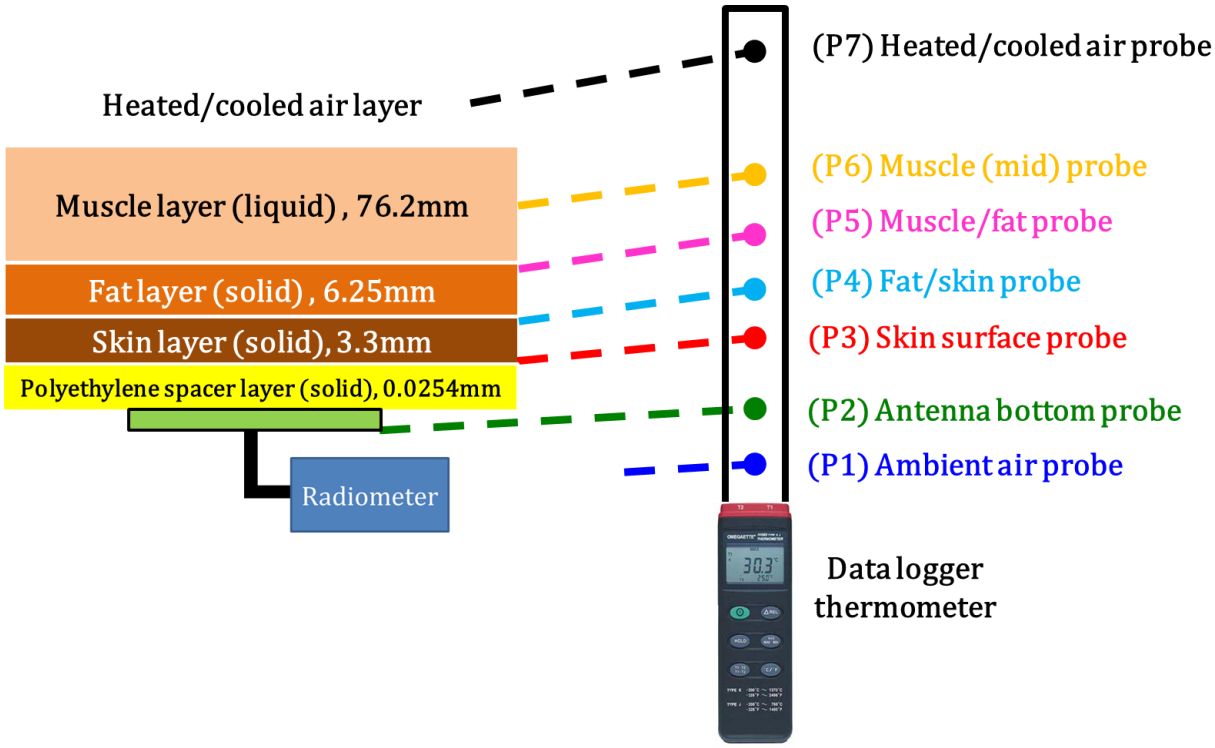

Figure 7.2 Measurement set-up of microwave radiometer and antenna in contact with a four-layer human body tissue mimicking phantom testbed. Thermocouple probes connected to a data-logger thermometer are placed at the following locations: (P1) in the ambient environment, (P2) on the back side of the antenna, (P3) at the PE-skin interface, (P4) at the skin-fat interface, (P5) at the fat-muscle interface, (P6) at a distance in the middle of the muscle phantom, and (P7) in the heat and cooled air above the muscle phantom.

www.manaraa.com

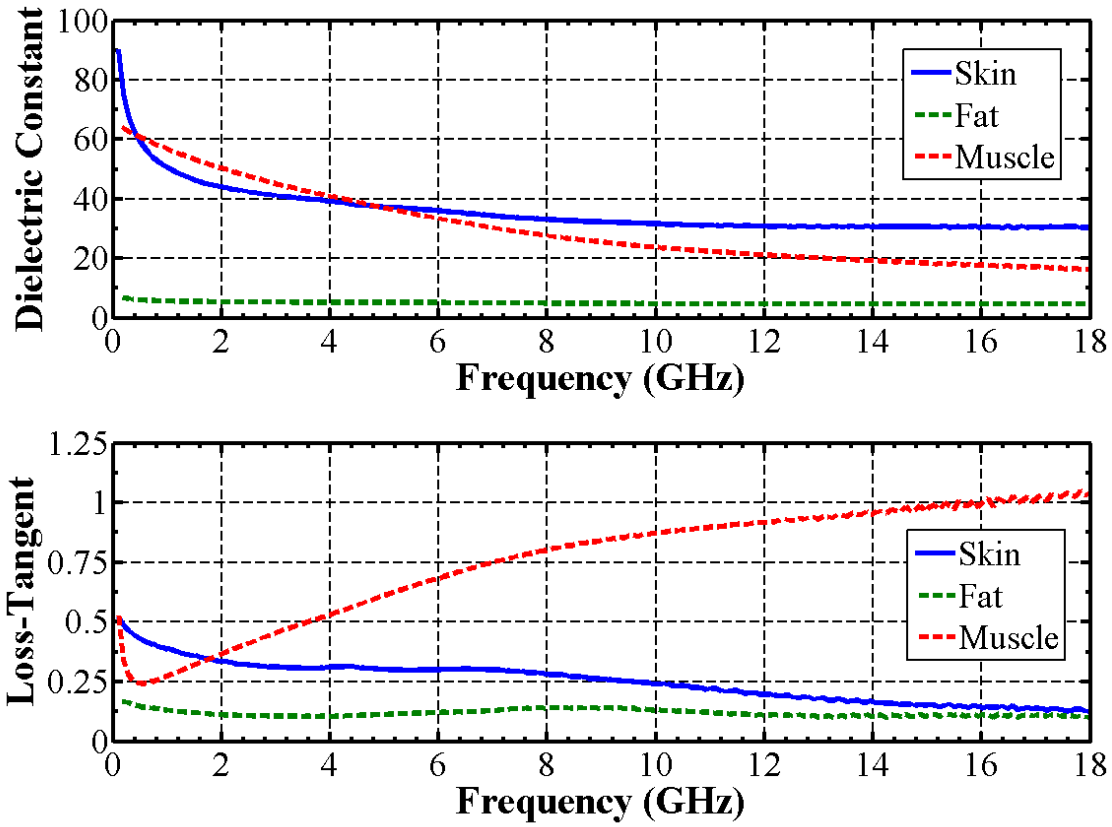

Figure 7.3 Dielectric constant and loss-tangent of human-mimicking tissue phantom layers.

www.manaraa.com

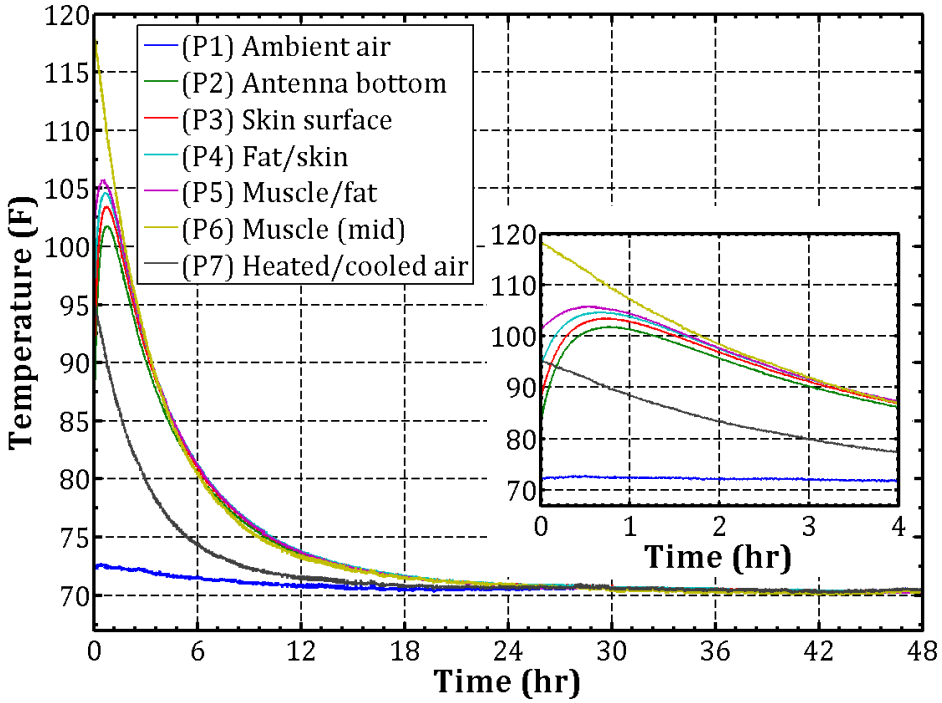

Figure 7.4 Thermocouple probed physical temperatures (P1) through (P7) from the layered human tissue phantom testbed. The tissue phantoms are heated and then allowed to cool down to ambient temperature.

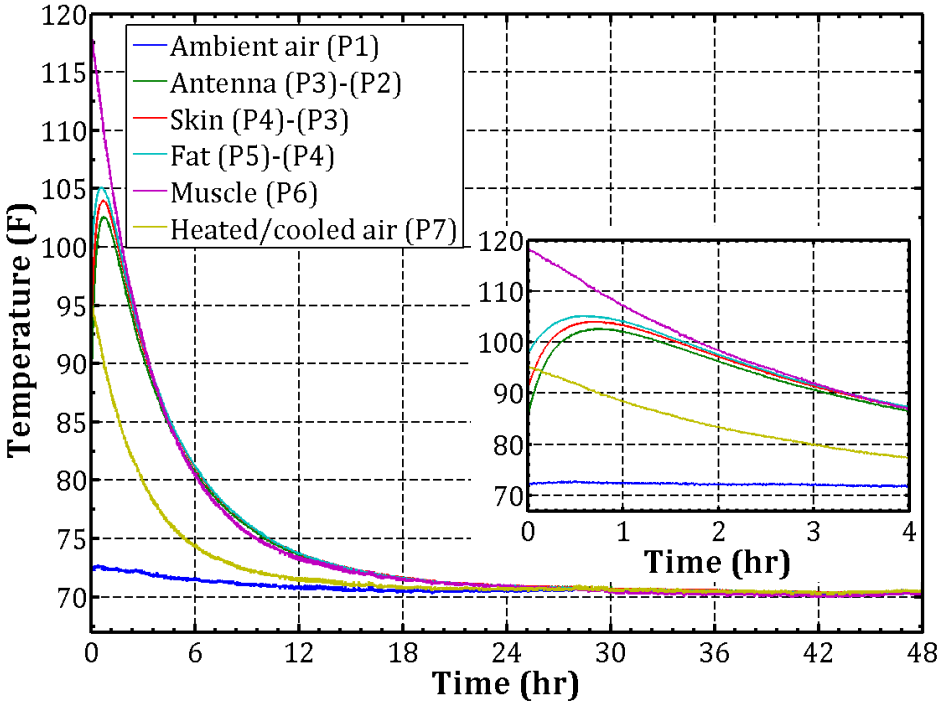

Figure 7.5 Individual layer temperatures as calculated from the thermocouple probed physical temperatures for the layered human tissue phantom testbed.

www.manaraa.com

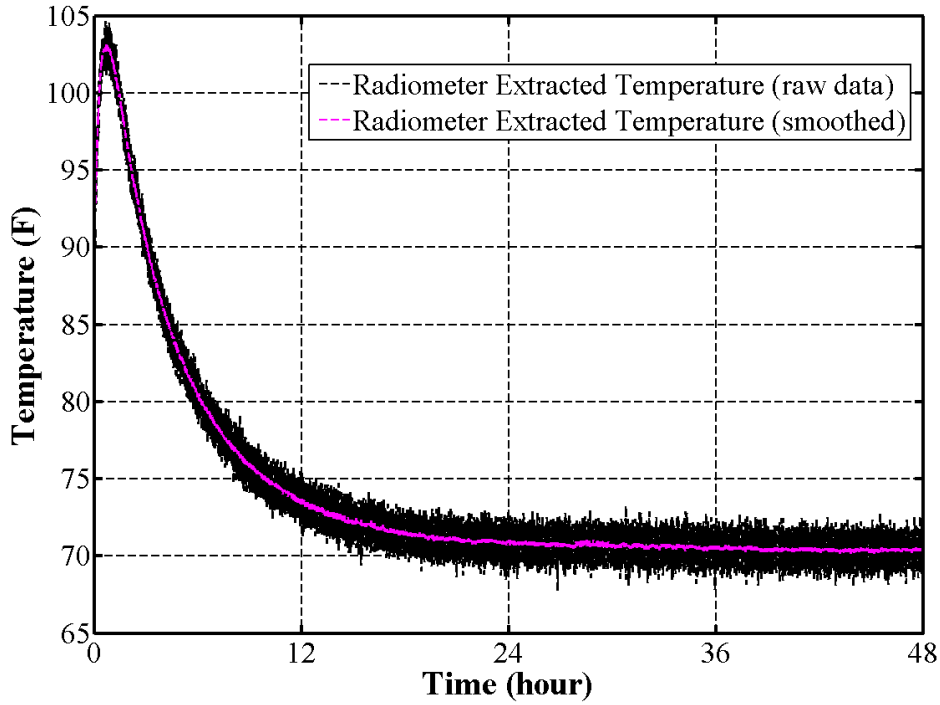

Figure 7.6 Detected radiometric antenna temperature from the heated tissue phantom tested for both smoothed and unsmoothed (raw) data.

7.4.1 Experimental Validation of the Non-Coherent Radiative Transfer Model

The four-layer non-coherent steady-state apparent temperature formulation is validated with an experimental radiometer measurement. The probed physical temperatures are input into the non-coherent radiative transfer formulations from equations (6.29) to (6.33) in order to calculate the steady-state effective brightness temperature. Figure 7.7 compares the calculated values from the four-layer steady-state apparent temperature model, equation (6.33), alongside the detected radiometric antenna temperature converted to an apparent temperature, equation (7.2) assuming a radiation efficiency of 95.429% and a main-beam efficiency of 87.59%, from the heated tissue phantom testbed. These aforementioned efficiency values are specified from the calculated quantities detailed in Section 5.4.4.1. As Figure 7.7 suggests, the modeled steady-state apparent temperature predicts the smoothed radiometric apparent temperature detected from the heated tissue phantom testbed very closely versus time. The percent difference is less than $\pm 1\%$ from the steady-state apparent temperature model to the smoothed radiometric apparent temperature

www.manaraa.com

detected from the heated tissue phantom testbed (Figure 7.8). The modeled versus measured data agreement suggests that the presented steady-state radiative transfer formulation is a viable method for accurate internal body temperature extraction.

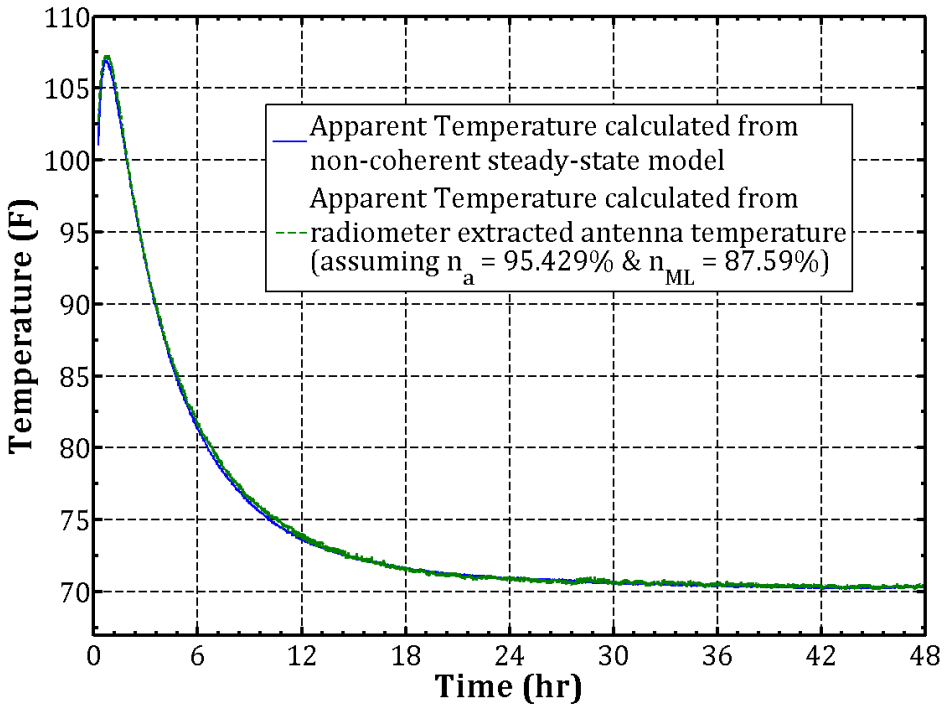

Figure 7.7 Comparison of the steady-state apparent temperature four-layer model to the detected radiometric antenna temperature converted to an apparent temperature from the heated tissue phantom tested.

www.manaraa.com

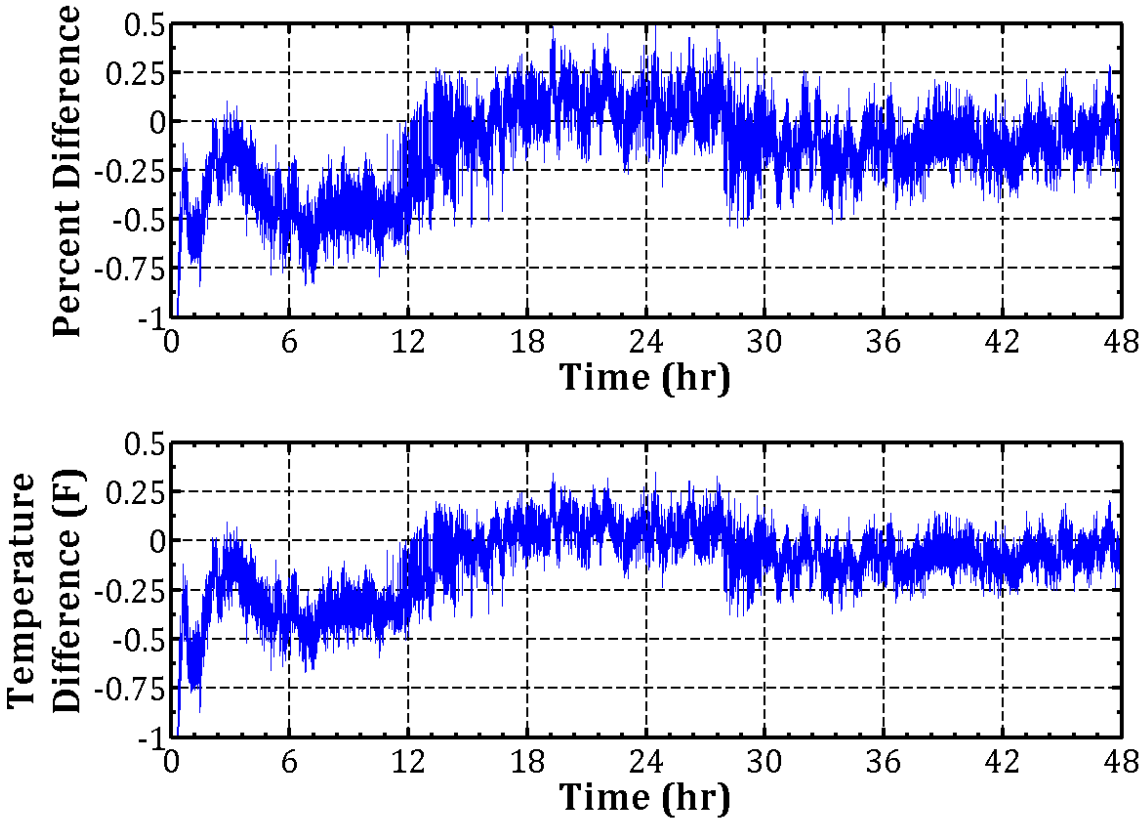

Figure 7.8 Percent difference (top) and absolute temperature difference (bottom) from the steady-state apparent temperature model to the smoothed radiometric apparent temperature detected from the heated tissue phantom testbed.

7.4.2 Experimental Validation of the Coherent Radiative Transfer Model

The four-layer coherent power wave effective brightness temperature formulation is validated with an experimental radiometer measurement. The probed physical temperatures are input into the non-coherent radiative transfer formulations from equations (6.69) to (6.72) in order to calculate the apparent temperature. Figure 7.9 compares the calculated values from the four-layer coherent power wave apparent temperature model, equation (6.72), alongside the detected radiometric antenna temperature converted to an effective brightness temperature, equation (7.2) a radiation efficiency of 95.429% and a main-beam efficiency of 87.59%, from the heated tissue phantom testbed. As Figure 7.10 (the percent difference and absolute temperature difference from the coherent power wave formulation to the extracted radiometric calculation)

www.manaraa.com

suggests, the coherent power wave apparent temperature does not predict the smoothed radiometric apparent temperature detected from the heated tissue phantom testbed very well. The variance in the compared apparent temperatures is due to the difference in the coherent reflectivity calculated from coherent power wave solution.

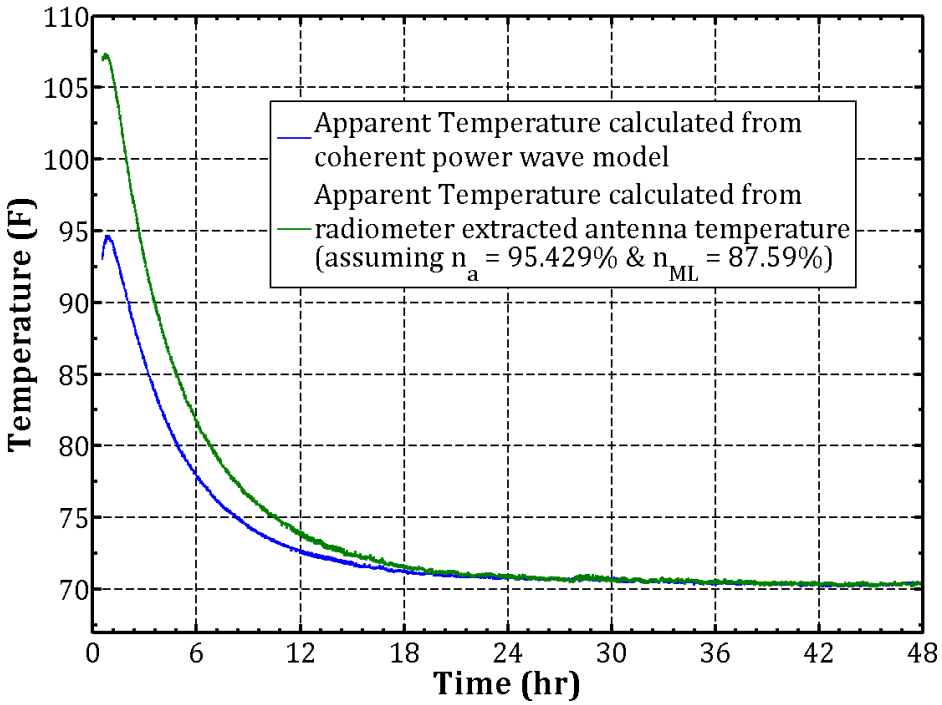

Figure 7.9 Comparison of the coherent power wave apparent temperature four-layer model to the detected radiometric antenna temperature converted to an apparent temperature from the heated tissue phantom tested.

www.manaraa.com

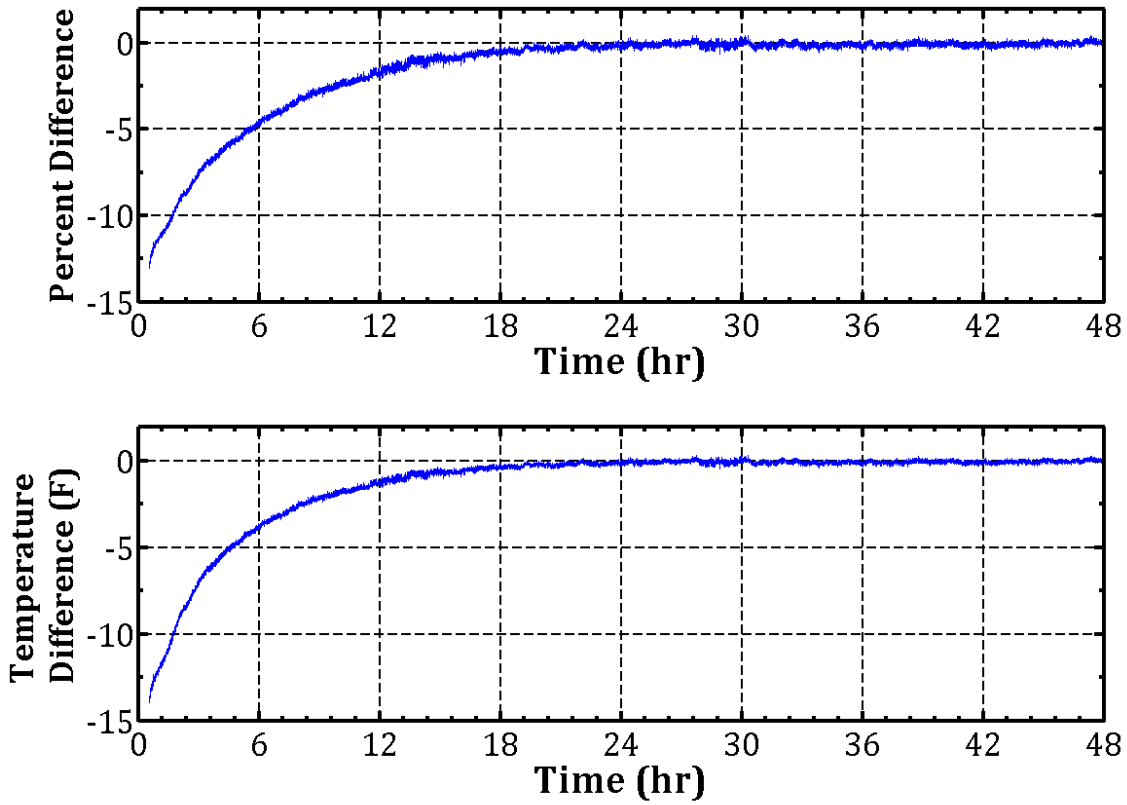

Figure 7.10 Percent difference (top) and absolute temperature difference (bottom) from the coherent power wave apparent temperature model to the smoothed radiometric apparent temperature detected from the heated tissue phantom testbed.

7.5 Conclusion

The steady-state non-coherent radiative transfer model predicts internal body temperatures with a good accuracy (within 1%) assuming the correct antenna efficiency parameters. The coherent power wave solution does not predict an accurate response due to the difference in the calculated coherent reflectivity value from the power weave model. Also, the contact sensing case is greatly affected by the down welling temperature from the human body.

www.manaraa.com

Chapter 8 Summary and Recommendations for Future Work

8.1 Summary

This dissertation developed a comprehensive closed-form analytical radiometric model and validated the effectiveness of the comprehensive model through a controlled life-like human body temperature sensing experiment. Wireless sub-skin temperature data was predicted from a human tissue mimicking phantom testbed to within 1%.

A generic isolated radiometer system equation is derived for all possible calibration source combinations. The generic isolated radiometer system equation predicts comparable results to that of an ideal simulation. While improved isolation decreases measurement uncertainty, it does not improve the accuracy of estimated noise temperatures using a perfectly-isolated radiometer system equation assumption.

A highly reproducible tissue-mimicking biological phantom (bio-phantom) recipe (comprised of urethane, graphite powder, and a solvent) was developed to accurately emulate the electrical properties of actual dry human skin versus frequency up to 18 GHz. The developed solid state skin phantom begins in pourable liquid form and then cures at room temperature into a dry solid state mold.

An in-plane electromagnetic bandgap structure was developed and integrated within an on-body inward facing spiral antenna design. The inclusion of the in-plane electromagnetic bandgap (EBG) structure demonstrated a +2.64dB gain improvement in the antenna broadside and -8dB in the rear gain while in-contact with the body as compared to the conventional spiral antenna. Likewise, the measured main beam efficiency is improved from 54.43% for the conventional antenna to 86.36% for the EBG antenna.

www.manaraa.com

Two techniques based on signal-flow graph theory were derived to explain both the non-coherent steady-state radiative transfer and the coherent radiative transfer within multi-layered dielectric media with non-uniform temperatures and any number of stratified layers. Both models allow for the accurate characterization and sensing of the thermal emissions originating from subsurface tissue layers.

8.2 Recommendations for Future Work

The following recommendations for future work are suggested in order to better realize a portable non-invasive microwave thermometer.

Differing amounts of system isolation were integrated with the total power radiometer configuration to better understand the differences sustained on extracted values with each isolation scenario. A perfectly-isolated radiometer system was assumed. However, a perfectly-isolated radiometer system is not possible. The calibration equation for the total power radiometer should be furthered explored to account for an imperfectly-isolated radiometer. A calibration equation that accounts for an imperfectly-isolated radiometer should allow for more precise temperature extractions and ultimately account for the total system temperature seen by a total power radiometer as outlined in equation (2.12).

An in-plane electromagnetic bandgap (EBG) structure was developed and integrated within an on-body inward facing spiral antenna design. The inclusion of the EBG structure improved the radiation characteristics of the antenna. However, the physical size of the antenna should be decreased. This offers an opportunity to design a compact non-contacting antenna with an EBG structure included. This planar style of the EBG integrated antenna also allows for the use of conformable materials.

Signal-flow graph theory was used to explain both the non-coherent steady-state and the coherent radiative transfer within multilayered media. This work specifically used a coherent approach derived from a coherent power wave formulation. Power wave formulations do not

www.manaraa.com

provide similar reflection properties as the tradition traveling wave reflection coefficient when the reference impedances are complex. A pseudo wave solution is needed to provide similar reflection properties as the traveling wave reflection coefficient. Also, a pseudo wave solution may have a more useful physical meaning than the power wave formulation.

A bio-phantom recipe comprised of urethane, graphite powder, and a solvent was developed to accurately emulate the electrical properties of actual dry human skin versus frequency up to 18 GHz. This recipe can be further improved by decreasing the curing time (which currently takes 18 hours at room temperature) and ultimately minimize the settling of graphite powder (which leads to inconsistent post-cure dielectric properties).

In this work, a microwave thermometer model was validated with a controlled life-like human body temperature sensing experiment. The radiometer was employed in a contacting configuration. The overall microwave thermometer temperature extraction can be improved by employing a non-contacting sensing configuration. A non-contacting sensing scenario is not plagued by the antenna temperature increases caused by the high heat body. For the contacting case, the antenna temperature begins at ambient temperature and it becomes increasingly difficult to predict the antenna temperature when it is also affected by changes in the body temperature. Measurement uncertainty should decrease when the antenna is isolated from the body.

www.manaraa.com

References

[1] "National Environmental Public Health Tracking Network," in *State Hospital Inpatient Discharge data*, C. f. D. C. a. Prevention, Ed., ed.

[2] "National Center for Health Statistics," Centers for Disease Control and Prevention.

[3] A. S. Howe and B. P. Boden, "Heat-Related Illness in Athletes," *The American Journal of Sports Medicine,* vol. 35, pp. 1384-1395, 2007/08/01 2007.

[4] (2011). *Healthcare Technologies Grand Challenges*. Available: https://www.epsrc.ac.uk/research/ourportfolio/themes/healthcaretechnologies/strategy/grandchallenges/

[5] J. L. Glazer, "Management of heatstroke and heat exhaustion," 20050614 DCOM- 20050714.

[6] A. W. Nichols, "Heat-related illness in sports and exercise," *Current Reviews in Musculoskeletal Medicine,* vol. 7, pp. 355-365, 2014.

[7] D. P. Jones, *Biomedical Sensors*: Momentum Press, 2010.

[8] E. E. Coris, D. J. Ramirez Am Fau - Van Durme, and D. J. Van Durme, "Heat illness in athletes: the dangerous combination of heat, humidity and exercise," *Sports Medicine,* vol. 34, 2004.

[9] E. E. Coris, S. M. Mehra S Fau - Walz, R. Walz Sm Fau - Duncanson, J. Duncanson R Fau - Jennings, D. Jennings J Fau - Nugent, K. Nugent D Fau - Zwygart, M. Zwygart K Fau - Pescasio, and M. Pescasio, "Gastrointestinal temperature trends in football linemen during physical exertion under heat stress," *Southern Medical Journal,* vol. 102, 2009.

[10] C. Byrne and C. L. Lim, "The ingestible telemetric body core temperature sensor: a review of validity and exercise applications," *British Journal of Sports Medicine,* vol. 41, pp. 126-133, 2007.

[11] C. C. W. G. Bongers, M. T. E. Hopman, and T. M. H. Eijsvogels, "Using an Ingestible Telemetric Temperature Pill to Assess Gastrointestinal Temperature During Exercise," *Journal of Visualized Experiments : JoVE,* p. 53258, 2015.

[12] Z. Popovic, P. Momenroodaki, and R. Scheeler, "Toward wearable wireless thermometers for internal body temperature measurements," *Communications Magazine, IEEE,* vol. 52, pp. 118-125, 2014.

[13] Q. Bonds, J. Gerig, T. M. Weller, and P. Herzig, "Towards Core Body Temperature Measurement via Close Proximity Radiometric Sensing," *Sensors Journal, IEEE,* vol. 12, pp. 519-526, 2012.

[14] Q. Bonds, P. Herzig, and T. M. Weller, "A Tissue Propagation Model for Validating Close-Proximity Biomedical Radiometer Measurements," GSFC-E-DAA-TN23891, 2016.

[15] S. Jacobsen and P. Stauffer, "Performance Evaluation of Various Antenna Configurations for Microwave Thermography During Superficial Hyperthermia," *Journal of Electromagnetic Waves and Applications,* vol. 15, pp. 111-134, 2001/01/01 2001.

[16] Q. Bonds, T. Weller, B. Roeder, and P. Herzig, "A tunable Cavity Backed Slot Antenna (CBSA) for close proximity biomedical sensing applications," in *2009 IEEE International Conference on Microwaves, Communications, Antennas and Electronics Systems*, 2009, pp. 1-5.

[17] S. Jacobsen* and K. Ø, "Improved Detectability in Medical Microwave Radio-Thermometers as Obtained by Active Antennas," *IEEE Transactions on Biomedical Engineering,* vol. 55, pp. 2778-2785, 2008.

www.manaraa.com

[18] T. Sugiura, Y. Kouno, A. Hashizume, H. Hirata, J. W. Hand, Y. Okita, and S. Mizushina, "Five-band microwave radiometer system for non-invasive measurement of brain temperature in new-born infants: system calibration and its feasibility," in *The 26th Annual International Conference of the IEEE Engineering in Medicine and Biology Society*, 2004, pp. 2292-2295.
[19] J. W. Hand, S. Van Leeuwen Gm Fau - Mizushina, J. B. Mizushina S Fau - Van de Kamer, K. Van de Kamer Jb Fau - Maruyama, T. Maruyama K Fau - Sugiura, D. V. Sugiura T Fau - Azzopardi, A. D. Azzopardi Dv Fau - Edwards, and A. D. Edwards, "Monitoring of deep brain temperature in infants using multi-frequency microwave radiometry and thermal modelling," 20010727 DCOM- 20011221.
[20] L. Dubois, J. J. Pribetich J Fau - Fabre, M. Fabre Jj Fau - Chive, Y. Chive M Fau - Moschetto, and Y. Moschetto, "Non-invasive microwave multifrequency radiometry used in microwave hyperthermia for bidimensional reconstruction of temperature patterns," 19930721 DCOM-19930721.
[21] K. Ø and S. Jacobsen, "Improved Radiometric Performance Attained by an Elliptical Microwave Antenna With Suction," *IEEE Transactions on Biomedical Engineering,* vol. 59, pp. 263-271, 2012.
[22] M. A. Ertürk, A.-M. M. El-Sharkawy, and P. A. Bottomley, "Monitoring local heating around an interventional MRI antenna with RF radiometry," *Medical Physics,* vol. 42, pp. 1411-1423, 2015.
[23] D. B. Rodrigues, P. F. Maccarini, S. Salahi, T. R. Oliveira, P. J. S. Pereira, P. Limão-Vieira, B. W. Snow, D. Reudink, and P. R. Stauffer, "Design and Optimization of an Ultra Wideband and Compact Microwave Antenna for Radiometric Monitoring of Brain Temperature," *IEEE Transactions on Biomedical Engineering,* vol. 61, pp. 2154-2160, 2014.
[24] P. R. Stauffer, B. W. Snow, D. B. Rodrigues, S. Salahi, T. R. Oliveira, D. Reudink, and P. F. Maccarini, "Non-Invasive Measurement of Brain Temperature with Microwave Radiometry: Demonstration in a Head Phantom and Clinical Case," *The neuroradiology journal,* vol. 27, pp. 3-12, 2014.
[25] D. B. Rodrigues, P. F. Maccarini, S. Salahi, E. Colebeck, E. Topsakal, P. J. S. Pereira, P. Limão-Vieira, and P. R. Stauffer, "Numerical 3D modeling of heat transfer in human tissues for microwave radiometry monitoring of brown fat metabolism," *Proceedings of SPIE,* vol. 8584, p. 10.1117/12.2004931, 2013.
[26] B. W. Snow, K. Arunachalam, V. De Luca, P. F. Maccarini, Ø. Klemetsen, Y. Birkelund, T. J. Pysher, and P. R. Stauffer, "Non-invasive vesicoureteral reflux detection: Heating risk studies for a new device," *Journal of pediatric urology,* vol. 7, pp. 624-630, 2011.
[27] S. Jacobsen, A. Murberg, and P. R. Stauffer, "Characterization of a Tranceiving Antenna Concept for Microwave Heating and Thermometry of Superficial Tumors - Abstract," *Journal of Electromagnetic Waves and Applications,* vol. 12, pp. 351-352, 1998/01/01 1998.
[28] F. T. Ulaby, A. K. Fung, and R. K. Moore, *Microwave Remote Sensing: Active and Passive* vol. 1: Fundamentals and Radiometry: Addison-Wesley Publishing Company, 1981.
[29] Y. A. Çengel and R. H. Turner, *Fundamentals of Thermal-fluid Sciences*: McGraw-Hill, 2000.
[30] D. M. Pozar, *Microwave Engineering*: Fourth edition. Hoboken, NJ : Wiley, [2012] ©2012, 2012.
[31] "Agilent fundamentals of RF and microwave noise figure measurements," Agilent Technologies 2006.
[32] "Noise figure measurement accuracy - The Y-factor method," Agilent Technologies 2004.
[33] C. Gabriel, S. Gabriel, and E. Corthout, "The dielectric properties of biological tissues: I. Literature survey," *Phys Med Biol,* vol. 41, pp. 2231-2249, 19970307 DCOM- 19970307 1996.

المنارة للاستشارات
www.manaraa.com

[34] S. Gabriel, R. W. Lau, and C. Gabriel, "The dielectric properties of biological tissues: II. Measurements in the frequency range 10 Hz to 20 GHz," *Phys Med Biol. ,* vol. 41, pp. 2251-2269, 19970307 DCOM- 19970307 1996.

[35] S. Gabriel, R. W. Lau, and C. Gabriel, "The dielectric properties of biological tissues: III. Parametric models for the dielectric spectrum of tissues," *Phys Med Biol. ,* vol. 41, pp. 2271-2293, 19970307 DCOM- 19970307 1996.

[36] D. Andreuccetti, R. Fossi, and C. Petrucci. An Internet resource for the calculation of the dielectric properties of body tissues in the frequency range 10 Hz - 100 GHz. Website at http://niremf.ifac.cnr.it/tissprop/. IFAC-CNR, Florence (Italy), 1997. Based on data published by C.Gabriel et al. in 1996. [Online].

[37] P. Risman, "Terminology and Notation of Microwave Power and Electromagnetic Energy," *Journal of Microwave Power and Electromagnetic Energy,* vol. 26, pp. 243-250, 1991/01/01 1991.

[38] J. C. Chiao and D. Kissinger, "Medical Applications of RF and Microwaves?Therapy and Safety [From the Guest Editors' Desk]," *IEEE Microwave Magazine,* vol. 16, pp. 12-13, 2015.

[39] J. C. Chiao and D. Kissinger, "Medical Applications of RF and Microwaves - Applications and Events [From the Guest Editors' Desk]," *IEEE Microwave Magazine,* vol. 16, pp. 14-18, 2015.

[40] D. Kissinger and J. C. Chiao, "Medical Applications of Radio-Frequency and Microwaves-Sensing, Monitoring, and Diagnostics [From the Guest Editors' Desk]," *IEEE Microwave Magazine,* vol. 16, pp. 34-38, 2015.

[41] K. L. Carr, "Microwave radiometry: its importance to the detection of cancer," *Microwave Theory and Techniques, IEEE Transactions on,* vol. 37, pp. 1862-1869, 1989.

[42] S. Mouty, B. Bocquet, R. Ringot, N. Rocourt, and P. Devos, "Microwave radiometric imaging (MWI) for the characterisation of breast tumours*," *Eur. Phys. J. AP,* vol. 10, pp. 73-78, 2000.

[43] M. El-Shenawee, "Numerical assessment of multifrequency microwave radiometry for sensing malignant breast cancer tumors," *Microwave and Optical Technology Letters,* vol. 36, pp. 394-398, 2003.

[44] K. Arunachalam, P. Maccarini, V. D. Luca, P. Tognolatti, F. Bardati, B. Snow, and P. Stauffer, "Detection of Vesicoureteral Reflux Using Microwave Radiometry—System Characterization With Tissue Phantoms," *IEEE Transactions on Biomedical Engineering,* vol. 58, pp. 1629-1636, 2011.

[45] A. Kavitha, F. M. Paolo, L. Valeria De, B. Fernando, W. S. Brent, and R. S. Paul, "Modeling the detectability of vesicoureteral reflux using microwave radiometry," *Physics in Medicine & Biology,* vol. 55, p. 5417, 2010.

[46] Y. Birkelund, S. K. Klemetsen O Fau - Jacobsen, K. Jacobsen Sk Fau - Arunachalam, P. Arunachalam K Fau - Maccarini, P. R. Maccarini P Fau - Stauffer, and P. R. Stauffer, "Vesicoureteral reflux in children: a phantom study of microwave heating and radiometric thermometry of pediatric bladder."

[47] K. Toutouzas, A. Synetos, C. Nikolaou, K. Stathogiannis, E. Tsiamis, and C. Stefanadis, "Microwave radiometry: a new non-invasive method for the detection of vulnerable plaque," *Cardiovascular Diagnosis and Therapy,* vol. 2, pp. 290-297, 2012.

[48] L. M. al-Alousi, R. A. Anderson, and D. V. Land, "A non-invasive method for postmortem temperature measurements using a microwave probe," *Forensic Science International,* vol. 64, pp. 35-46, 1994/01/01/ 1994.

[49] J. Robert, J. Edrich, P. Thouvenot, M. Gautherie, and J. M. Escanye, "Millimeter-Wave Thermography Preliminary Clinical Findings in Head and Neck Diseases," *Journal of Microwave Power,* vol. 14, pp. 131-134, 1979/01/01 1979.

www.manaraa.com

[50] P. R. Stauffer, D. B. Rodriques, S. Salahi, E. Topsakal, T. R. Oliveira, A. Prakash, F. D'Isidoro, D. Reudink, B. W. Snow, and P. F. Maccarini, "Stable Microwave Radiometry System for Long Term Monitoring of Deep Tissue Temperature," *Proceedings of SPIE,* vol. 8584, p. 10.1117/12.2003976, 2013.
[51] L. R. Ballew, "A microwave radiometer system for use in biomedical applications," Baylor University 2007.
[52] A. G. MacDonald, R. D. Land Dv Fau - Sturrock, and R. D. Sturrock, "Microwave thermography as a noninvasive assessment of disease activity in inflammatory arthritis."
[53] E. Zampeli, I. Raftakis, A. Michelongona, C. Nikolaou, A. Elezoglou, K. Toutouzas, E. Siores, and P. P. Sfikakis, "Detection of Subclinical Synovial Inflammation by Microwave Radiometry," *PLOS ONE,* vol. 8, p. e64606, 2013.
[54] J. Edrich and C. J. Smyth, "Millimeter Wave Thermograph as Subcutaneous Indicator of Joint Inflammation," in *1977 7th European Microwave Conference*, 1977, pp. 713-717.
[55] A. M. Shaeffer J Fau - el-Mahdi, A. E. el-Mahdi Am Fau - Hamwey, Jr., K. L. Hamwey Ae Jr Fau - Carr, and K. L. Carr, "Detection of extravasation of antineoplastic drugs by microwave radiometry."
[56] D. V. Land, "Medical microwave radiometry and its clinical applications," in *IEE Colloquium on Application of Microwaves in Medicine*, 1995, pp. 2/1-2/5.
[57] Y. Leroy, A. Mamouni, J. C. Van de Velde, and B. Bocquet, "Microwave Radiometry and Thermography," in *Electromagnetic Interaction with Biological Systems*, J. C. Lin, Ed., ed Boston, MA: Springer US, 1989, pp. 27-38.
[58] K. R. Foster and E. A. Cheever, "Microwave radiometry in biomedicine: A reappraisal," *Bioelectromagnetics,* vol. 13, pp. 567-579, 1992.
[59] J. Randa and L. A. Terrel, "Noise-Temperature Measurement System for the WR-28 Band," *NIST Technical Note,* vol. 1395, 1997.
[60] C. A. Grosvenor, J. Randa, and R. L. Billinger, "Design and Testing of NFRad- A New Noise Measurement System," *NIST Technical Note,* vol. 1518, 2000.
[61] M. Weatherspoon and L. Dunleavy, "Enhanced One-Port Noise Temperature Measurements Using a Noise Figure Meter," in *ARFTG Conference Digest-Spring, 57th*, 2001, pp. 1-4.
[62] J. Randa, "Amplifier and Transistor Noise-Parameter Measurements," in *Wiley Encyclopedia of Electrical and Electronics Engineering*, ed: John Wiley & Sons, Inc., 2014.
[63] M. H. Weatherspoon, L. P. Dunleavy, A. Boudiaf, and J. Randa, "Vector corrected noise temperature measurements," in *2002 IEEE MTT-S International Microwave Symposium Digest (Cat. No.02CH37278)*, 2002, pp. 2253-2256 vol.3.
[64] C. K. S. Miller, W. C. Daywitt, and M. G. Arthur, "Noise standards, measurements, and receiver noise definitions," *Proceedings of the IEEE,* vol. 55, pp. 865-877, 1967.
[65] T. Y. Otoshi, "The Effect of Mismatched Components on Microwave Noise-Temperature Calibrations," *IEEE Transactions on Microwave Theory and Techniques,* vol. 16, pp. 675-686, 1968.
[66] J. S. Wells, W. C. Daywitt, and C. K. S. Miller, "Measurement of Effective Temperatures of Microwave Noise Sources," *IEEE Transactions on Instrumentation and Measurement,* vol. IM-13, pp. 17-28, 1964.
[67] W. C. Dawitt, "Radiometer equation and analysis of systematic errors for the NIST automated radiometers," *NIST Technical Note,* vol. 1327, 1989.
[68] S. P. Pucic, "Derivation of the System Equation for Null-Balanced Total-Power Radiometer System NCS1," *J. Res. Natl. Inst. Stand. Technol. ,* vol. 99, pp. 55-63, 1994.
[69] D. F. Wait, "Radiometer equation for noise comparison radiometers," *IEEE Transactions on Instrumentation and Measurement,* vol. 44, pp. 336-339, 1995.

www.manaraa.com

[70] J. Randa, D. K. Walker, A. E. Cox, and R. L. Billinger, "Errors resulting from the reflectivity of calibration targets," *IEEE Transactions on Geoscience and Remote Sensing,* vol. 43, pp. 50-58, 2005.
[71] T. W. Kang, J. H. Kim, J. G. Lee, J. I. Park, and D. C. Kim, "Determining Noise Temperature of a Noise Source Using Calibrated Noise Sources and an RF Attenuator," *IEEE Transactions on Instrumentation and Measurement,* vol. 60, pp. 2558-2563, 2011.
[72] M. H. Weatherspoon and L. P. Dunleavy, "Vector corrected on-wafer measurements of noise temperature," *IEEE Transactions on Instrumentation and Measurement,* vol. 54, pp. 1327-1332, 2005.
[73] Q. Bonds, "A Microwave Radiometer for Close Proximity Core Body Temperature Monitoring: Design, Development, and Experimentation," Ph.D. Dissertation, University of South Florida, 2010.
[74] A. T. Mobashsher and A. M. Abbosh, "Artificial Human Phantoms: Human Proxy in Testing Microwave Apparatuses That Have Electromagnetic Interaction with the Human Body," *IEEE Microwave Magazine,* vol. 16, pp. 42-62, 2015.
[75] A. Trehan and N. Nikolova, "Summary of Materials and Recipes available in the Literature to Fabricate Biological Phantoms for RF and Microwave Experiments," McMaster University 2007.
[76] W. M. A. Ibrahim, H. M. Algabroun, and M. T. Almaqtari, "Short Review on the Used Recipes to Simulate the Bio-Tissue at Microwave Frequencies," in *4th Kuala Lumpur International Conference on Biomedical Engineering 2008: BIOMED 2008 25–28 June 2008 Kuala Lumpur, Malaysia*, N. A. Abu Osman, F. Ibrahim, W. A. B. Wan Abas, H. S. Abdul Rahman, and H.-N. Ting, Eds., ed Berlin, Heidelberg: Springer Berlin Heidelberg, 2008, pp. 234-237.
[77] K. Ito, "NUMERICAL AND EXPERIMENTAL HUMAN BODY PHANTOMS," in *2007 IET Seminar on Antennas and Propagation for Body-Centric Wireless Communications*, 2007, pp. 6-12.
[78] T. Yilmaz, R. Foster, and Y. Hao, "Broadband Tissue Mimicking Phantoms and a Patch Resonator for Evaluating Noninvasive Monitoring of Blood Glucose Levels," *IEEE Transactions on Antennas and Propagation,* vol. 62, pp. 3064-3075, 2014.
[79] Y. Machii, H. Aoki, and K. Koshiji, "Fat Thickness Estimation Method Using Bio Electrical Property Examination by Gel Phantom Model Test," in *2006 IEEE International Symposium on MicroNanoMechanical and Human Science*, 2006, pp. 1-6.
[80] G. Hartsgrove, A. Kraszewski, and A. Surowiec, "Simulated biological materials for electromagnetic radiation absorption studies," *Bioelectromagnetics,* vol. 8, pp. 29-36, 1987.
[81] Y. Nikawa, M. Chino, and K. Kikuchi, "Soft and dry phantom modeling material using silicone rubber with carbon fiber," *IEEE Transactions on Microwave Theory and Techniques,* vol. 44, pp. 1949-1953, 1996.
[82] J. Garrett and E. Fear, "Stable and Flexible Materials to Mimic the Dielectric Properties of Human Soft Tissues," *IEEE Antennas and Wireless Propagation Letters,* vol. 13, pp. 599-602, 2014.
[83] J. Garrett and E. C. Fear, "A time- and temperature-stable complex breast phantom for microwave breast imaging," in *2013 USNC-URSI Radio Science Meeting (Joint with AP-S Symposium)*, 2013, pp. 32-32.
[84] J. Garrett and E. Fear, "A New Breast Phantom With a Durable Skin Layer for Microwave Breast Imaging," *IEEE Transactions on Antennas and Propagation,* vol. 63, pp. 1693-1700, 2015.
[85] C. Gabriel, "Tissue equivalent material for hand phantoms," *Physics in Medicine & Biology,* vol. 52, p. 4205, 2007.
[86] H. Tamura, Y. Ishikawa, T. Kobayashi, and T. Nojima, "A dry phantom material composed of ceramic and graphite powder," *IEEE Transactions on Electromagnetic Compatibility,* vol. 39, pp. 132-137, 1997.

www.manaraa.com

[87] Y. T. Lo and S. W. Lee, *Antenna Handbook: Volume III Applications*: Van Nostrand Reinhold, 1993.
[88] K. L. Carr, "Antenna: the critical element in successful medical technology," in *Microwave Symposium Digest, 1990., IEEE MTT-S International*, 1990, pp. 525-527 vol.1.
[89] J. Volakis, *Antenna Engineering Handbook, Fourth Edition*: McGraw-Hill Companies,Incorporated, 2007.
[90] J. Volakis, C. C. Chen, and K. Fujimoto, *Small Antennas:Miniaturization Techniques & Applications*: Mcgraw-hill, 2010.
[91] G. H. Miranda, R. V. Iyer, and S. Pamidighantam, "Analysis and Optimization of Dual Arm, Center Excited, Surface Micro-machined Archimedean Spiral Antenna with Improved Wideband Characteristics," in *COMSOL Conference 2011*, Bangalore, India.
[92] S. Bosch, J. Ferre-Borrull, N. Leinfellner, and A. Canillas, "Effective dielectric function of mixtures of three or more materials: a numerical procedure for computations," *Surface Science* vol. 453, pp. 9-17, 2000.
[93] M. Grady and T. M. Weller, "Using resistive loading to control the radiation efficiency of a spiral antenna," in *WAMICON 2014*, 2014, pp. 1-4.
[94] Y. Fan and Y. Rahmat-Samii, "Microstrip antennas integrated with electromagnetic band-gap (EBG) structures: a low mutual coupling design for array applications," *IEEE Transactions on Antennas and Propagation,* vol. 51, pp. 2936-2946, 2003.
[95] D. Sievenpiper, Z. Lijun, R. F. J. Broas, N. G. Alexopolous, and E. Yablonovitch, "High-impedance electromagnetic surfaces with a forbidden frequency band," *IEEE Transactions on Microwave Theory and Techniques,* vol. 47, pp. 2059-2074, 1999.
[96] S. Raza, "Characterization of the Reflection and Dispersion Properties of 'Mushroom'-related Structures and their Applications to Antennas," Electrical and Computer Engineering, University of Toronto, 2012.
[97] A. W. England, "Thermal microwave emission from a scattering layer," *Journal of Geophysical Research,* vol. 80, pp. 4484-4496, 1975.
[98] C. T. Swift, W. L. Jones, R. F. Harrington, J. C. Fedors, R. H. Couch, and B. L. Jackson, "Microwave radar and radiometric remote sensing measurements of lake ice," *Geophysical Research Letters,* vol. 7, pp. 243-246, 1980.
[99] T. J. Schmugge and B. J. Choudhury, "A comparison of radiative transfer models for predicting the microwave emission from soils," *Radio Science,* vol. 16, pp. 927-938, 1981.
[100] R. Scheeler, E. F. Kuester, and Z. Popovic, "Sensing Depth of Microwave Radiation for Internal Body Temperature Measurement," *Antennas and Propagation, IEEE Transactions on,* vol. 62, pp. 1293-1303, 2014.
[101] D. A. Morton, K. B. Foreman, and K. H. Albertine, "Chapter 7. Anterior Abdominal Wall," in *The Big Picture: Gross Anatomy*, ed New York, NY: The McGraw-Hill Companies, 2011.
[102] W. J. Burke, T. Schmugge, and J. F. Paris, "Comparison of 2.8- and 21-cm microwave radiometer observations over soils with emission model calculations," *Journal of Geophysical Research: Oceans,* vol. 84, pp. 287-294, 1979.
[103] F. T. Ulaby, A. K. Fung, and R. K. Moore, *Microwave Remote Sensing: Active and Passive* vol. 3: From Theory to Aplications: Addison-Wesley Publishing Company, 1986.
[104] T. T. Wilheit, "Radiative Transfer in a Plane Stratified Dielectric," *IEEE Transactions on Geoscience Electronics,* vol. 16, pp. 138-143, 1978.
[105] L. Tsang, E. Njoku, and J. A. Kong, "Microwave thermal emission from a stratified medium with nonuniform temperature distribution," *Journal of Applied Physics,* vol. 46, pp. 5127-5133, 1975/12/01 1975.
[106] M. Grady and T. M. Weller, "Comparison of Coherent and Non-Coherent Scattering Models for Stratified Media," *WAMICON 2017,* pp. 1-5, 2017.

www.manaraa.com

[107] E. G. Njoku and J.-A. Kong, "Theory for passive microwave remote sensing of near-surface soil moisture," *Journal of Geophysical Research,* vol. 82, pp. 3108-3118, 1977.
[108] A. Stogryn, "The Brightness Temperature of a Vertically Structured Medium," *Radio Science,* vol. 5, pp. 1397-1406, 1970.
[109] D.-J. Lee and J. F. Whitaker, "Analysis of optical and terahertz multilayer systems using microwave and feedback thoery," *Microwave and Optical Technology Letters,* vol. 51, pp. 1308-1312, 2009.
[110] K. Kurokawa, "Power Waves and the Scattering Matrix," *IEEE Transactions on Microwave Theory and Techniques,* vol. 13, pp. 194-202, 1965.
[111] D. Williams, "Traveling Waves and Power Waves: Building a Solid Foundation for Microwave Circuit Theory," *IEEE Microwave Magazine,* vol. 14, pp. 38-45, 2013.
[112] G. Gonzalez, *Microwave Transistor Amplifiers: Analysis and Design*: Prentice Hall, 1997.
[113] D. A. Frickey, "Conversions between S, Z, Y, H, ABCD, and T parameters which are valid for complex source and load impedances," *IEEE Transactions on Microwave Theory and Techniques,* vol. 42, pp. 205-211, 1994.
[114] M. A. Gibney, C. H. Arce, K. J. Byron, and L. J. Hirsch, "Skin and subcutaneous adipose layer thickness in adults with diabetes at sites used for insulin injections: implications for needle length recommendations," *Current Medical Research and Opinion,* vol. 26, pp. 1519-1530, 2010/06/01 2010.
[115] R. B. Marks, D. F. Williams, and D. A. Frickey, "Comments on "Conversions between S, Z, Y, h, ABCD, and T parameters which are valid for complex source and load impedances" [with reply]," *IEEE Transactions on Microwave Theory and Techniques,* vol. 43, pp. 914-915, 1995.
[116] R. Marks and D. F. Williams, "A General Waveguide Circuit Theory," *Journal of Research (NIST JRES),* vol. 97, 1992.
[117] "Arbitrary Impedance: Accurate Measurement in Almost Any Impedance Environment," *Anritsu Application Note*.
[118] "IEEE Standard Definitions of Terms for Antennas," *IEEE Std 145-1993,* pp. 1-32, 1993.
[119] H. A. Wheeler, "Fundamental limitaions of a small VLF antenna for submarines," *Antennas and Propagation, IRE Transactions on,* vol. 6, pp. 123-125, 1958.
[120] H. A. Wheeler, "Useful radiation from an underground antenna," *Journal of Research of the National Bureau of Standards - Section D. Radio Propagation,* vol. 65, p. 2, 1961.
[121] R. C. Hansen, "Radiation and reception with buried and submerged antennas," *Antennas and Propagation, IEEE Transactions on,* vol. 11, pp. 207-216, 1963.
[122] R. K. Moore, "Effects of a surrounding conducting medium on antenna analysis," *Antennas and Propagation, IEEE Transactions on,* vol. 11, pp. 216-225, 1963.
[123] A. Karlsson, "Physical limitations of antennas in a lossy medium," *Antennas and Propagation, IEEE Transactions on,* vol. 52, pp. 2027-2033, 2004.
[124] K. Kihyun, Y. Sumin, L. Sungho, N. Sangwook, Y. Young Joong, and C. Changyul, "A Design of a High-Speed and High-Efficiency Capsule Endoscopy System," *Biomedical Engineering, IEEE Transactions on,* vol. 59, pp. 1005-1011, 2012.
[125] L. Jaechun and N. Sangwook, "Q Evaluation of Antennas in an Electrically Conductive Medium," *Antennas and Propagation, IEEE Transactions on,* vol. 56, pp. 2116-2120, 2008.
[126] L. Jaechun and N. Sangwook, "Effective Area of a Receiving Antenna in a Lossy Medium," *Antennas and Propagation, IEEE Transactions on,* vol. 57, pp. 1843-1845, 2009.
[127] T. Dissanayake, K. P. Esselle, and M. R. Yuce, "Dielectric Loaded Impedance Matching for Wideband Implanted Antennas," *Microwave Theory and Techniques, IEEE Transactions on,* vol. 57, pp. 2480-2487, 2009.
[128] V. T. Nguyen and C. W. Jung, "Impact of Dielectric Constant on Embedded Antenna Efficiency," *International Journal of Antennas and Propagation,* vol. 2014, p. 6, 2014.

www.manaraa.com

[129] C. Wen-Tzu and C. Huey-Ru, "Numerical computation of human interaction with arbitrarily oriented superquadric loop antennas in personal communications," *Antennas and Propagation, IEEE Transactions on,* vol. 46, pp. 821-828, 1998.
[130] R. C. Dorf and R. H. Bishop, *Modern Control Systems*, 12 ed.: Pearson Prentice Hall, 2011.

www.manaraa.com

Appendix A Description of Antenna Efficiencies

A.1 Antenna Main-Beam Efficiency

The antenna main-beam efficiency η_{ML} is described below. The antenna probing footprint is shown in Figure A.1. The main-beam and side-beam efficiencies are calculated through an initial normalization of the antenna radiation pattern [13]. The main-beam efficiency is a ratio of the sum of the portion of the normalized pattern located in the upper half-space (-90° < θ < 90°) to the sum of the full-space normalized pattern (-180° < θ < 180°).

$$\eta_{ML} = \sum_{\theta=-90^\circ}^{90^\circ} P_{ant}^{norm}(\theta) \Big/ \sum_{\theta=-180^\circ}^{180^\circ} P_{ant}^{norm}(\theta). \tag{A.1}$$

The side-beam efficiency is a ratio of the sum of the portion of the normalized pattern located in the lower half-space (90° < θ < 180° & -180° < θ < -90°) to the sum of the full-space normalized pattern (-180° < θ < 180°).

$$\eta_{SL} = 1 - \eta_{ML} = \left(\sum_{\theta=-180^\circ}^{-90^\circ} P_{ant}^{norm}(\theta) + \sum_{\theta=90^\circ}^{180^\circ} P_{ant}^{norm}(\theta) \right) \Big/ \sum_{\theta=-180^\circ}^{180^\circ} P_{ant}^{norm}(\theta). \tag{A.2}$$

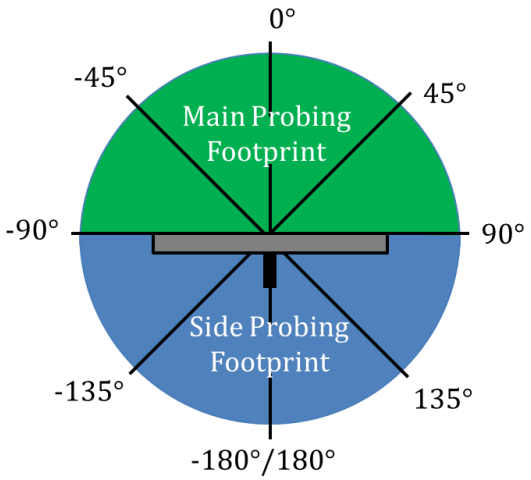

Figure A.1 Radiation pattern normalization to calculate main-beam efficiency.

www.manaraa.com

A.2 Antenna Radiation Efficiency

The antenna radiation efficiency η_{rad} is described below. IEEE defines radiation efficiency as the ratio of the total power radiated by an antenna to the net power accepted by the antenna from the connected transmitter [118]. The challenge of calculating the efficiency of an antenna in the presence of a lossy conducting medium was tackled as far back as the 1960's when authors including Wheeler [119, 120], Hansen [121], and Moore [122] have all in some form discussed the differences between the field analyses when evaluating an antenna in air versus being in a conducting medium. Later works [123-126] have explicitly stated the calculation of the radiation efficiency of an antenna in the presence of a lossy medium as given by

$$P_{out}(r) = P_{in}\,\eta_{rad} \cdot e^{-2|\mathrm{Im}(k)|r} \tag{A.3}$$

where P_{out} is the output power at a sphere distance of *'r'*, P_{in} is the input power, and k is the wave number.

More recent works [127, 128] have expressed that the radiation efficiency of an antenna radiating in the presence of a lossy biological medium is affected by the loss absorbed by the biological tissue. As equation (A.3) suggests, the antenna radiation efficiency should only be affected by the losses from the actual antenna and should not include the absorption effects from the propagation medium. The total efficiency, however, does include all the losses that reduce the maximum gain. Notice that the total efficiency in equation (A.3), expressed in terms of P_{out}/P_{in}, includes both the radiation efficiency and the absorption term. This convention is consistent with [129] where total efficiency is explicitly listed as the product of the ohmic efficiency and absorption efficiency. While equation (A.3) does, in principle, show the distinction between total efficiency and radiation efficiency, it does not provide the complete picture of all the loss affecting the total efficiency. In terms of biomedical radiometric sensing, the total efficiency actually takes into account the biological medium absorption loss, the spillover loss, the mismatch loss, and the

www.manaraa.com

conductor and dielectric substrate loss. Using a similar naming convention in [127, 128], the radiation efficiency is defined as

$$\eta_{rad} = \frac{P_{out}}{P_{in} - P_{mismatch} - P_{spillover} - P_{tissue}}, \tag{A.4}$$

and the total efficiency is defined as

$$\eta_{tot} = \frac{P_{out}}{P_{in}}, \tag{A.5}$$

with

$$P_{out} = P_{in} - P_{mismatch} - P_{spillover} - P_{tissue} - P_{ant}\,, \tag{A.6}$$

where $P_{mismatch}$ (mismatch power loss) is the power loss in watts due to the antenna source mismatch, $P_{spillover}$ (spillover power loss) is the power loss due to energy spilling beyond the antenna edge into the back lobes, P_{tissue} (tissue absorption power loss) is the power loss absorbed by the biological tissue, and P_{ant} is the power loss due to antenna conductor and dielectric substrate.

www.manaraa.com

Appendix B Mason's Signal Flow Gain Rule

B.1 Mason's Rule

The transfer function between a system input and output can be found using Mason's signal-flow gain formula [130],

$$G_{total} = \sum_{k=1}^{P_{total}} \frac{G_k \cdot \Delta_k}{\Delta} \tag{B.1}$$

where G_{total} is the total gain from the source node to output node, P_{total} is the total number of paths, G_k is the kth path gain, Δ is the determinant, and Δ_k is the kth path cofactor.

www.manaraa.com

Appendix C Copyright Permissions

C.1 Permissions for Chapter 6

Copyright Clearance Center RightsLink®

Home | Create Account | Help

IEEE Requesting permission to reuse content from an IEEE publication

Title:	Comparison of coherent and non-coherent scattering models for stratified media
Conference Proceedings:	2017 IEEE 18th Wireless and Microwave Technology Conference (WAMICON)
Author:	Michael Grady; Thomas M. Weller
Publisher:	IEEE
Date:	24-25 April 2017

Copyright © 2017, IEEE

LOGIN

If you're a copyright.com user, you can login to RightsLink using your copyright.com credentials. Already a RightsLink user or want to learn more?

Thesis / Dissertation Reuse

The IEEE does not require individuals working on a thesis to obtain a formal reuse license, however, you may print out this statement to be used as a permission grant:

Requirements to be followed when using any portion (e.g., figure, graph, table, or textual material) of an IEEE copyrighted paper in a thesis:

1) In the case of textual material (e.g., using short quotes or referring to the work within these papers) users must give full credit to the original source (author, paper, publication) followed by the IEEE copyright line © 2011 IEEE.
2) In the case of illustrations or tabular material, we require that the copyright line © [Year of original publication] IEEE appear prominently with each reprinted figure and/or table.
3) If a substantial portion of the original paper is to be used, and if you are not the senior author, also obtain the senior author's approval.

Requirements to be followed when using an entire IEEE copyrighted paper in a thesis:

1) The following IEEE copyright/ credit notice should be placed prominently in the references: © [year of original publication] IEEE. Reprinted, with permission, from [author names, paper title, IEEE publication title, and month/year of publication]
2) Only the accepted version of an IEEE copyrighted paper can be used when posting the paper or your thesis on-line.
3) In placing the thesis on the author's university website, please display the following message in a prominent place on the website: In reference to IEEE copyrighted material which is used with permission in this thesis, the IEEE does not endorse any of [university/educational entity's name goes here]'s products or services. Internal or personal use of this material is permitted. If interested in reprinting/republishing IEEE copyrighted material for advertising or promotional purposes or for creating new collective works for resale or redistribution, please go to http://www.ieee.org/publications_standards/publications/rights/rights_link.html to learn how to obtain a License from RightsLink.

If applicable, University Microfilms and/or ProQuest Library, or the Archives of Canada may supply single copies of the dissertation.

BACK | CLOSE WINDOW

Copyright © 2017 Copyright Clearance Center, Inc. All Rights Reserved. Privacy statement. Terms and Conditions.
Comments? We would like to hear from you. E-mail us at customercare@copyright.com

www.manaraa.com

About the Author

Michael Grady was born in Birmingham, AL. He received the B.S. (2008) and M.S. (2010) degrees in electrical engineering from Auburn University in Auburn, AL. He is currently pursuing a Ph.D. in electrical engineering at the University of South Florida (USF) in Tampa, FL. During his tenure at USF, Michael has been awarded the IEEE MTT-S 2016 WAMICON Best Student Research Poster Award, 1st place* in the IEEE MTT-S IMS2015 Apps for Microwave Theory and Techniques Competition, 2nd place in the IEEE MTT-S 2015 Video Competition, the IEEE MTT-S 2014 Graduate Fellowship for Medical Applications, 2nd place in the IEEE MTT-S 2012 Video Competition, 3rd place in the IEEE MTT-S 2013 Video Competition, the NSF Graduate Research Diversity Supplement (GRDS), the Alfred P. Sloan Minority Ph.D. Scholarship, the McKnight Doctoral Fellowship, and the GEM Doctoral Fellowship. He served on the steering committee for IEEE MTT-S IMS2014, 2015, 2016 Project Connect at the International Microwave Symposium (IMS). Michael interned at Corning, Inc. in 2010 and NASA Goddard Space Flight Center in 2013. His research interests lie in microwave (MW) measurements, MW circuit design, and biomedical radiometry.

Visit Michael on LinkedIn at www.linkedin.com/in/michael-grady/.

www.manaraa.com